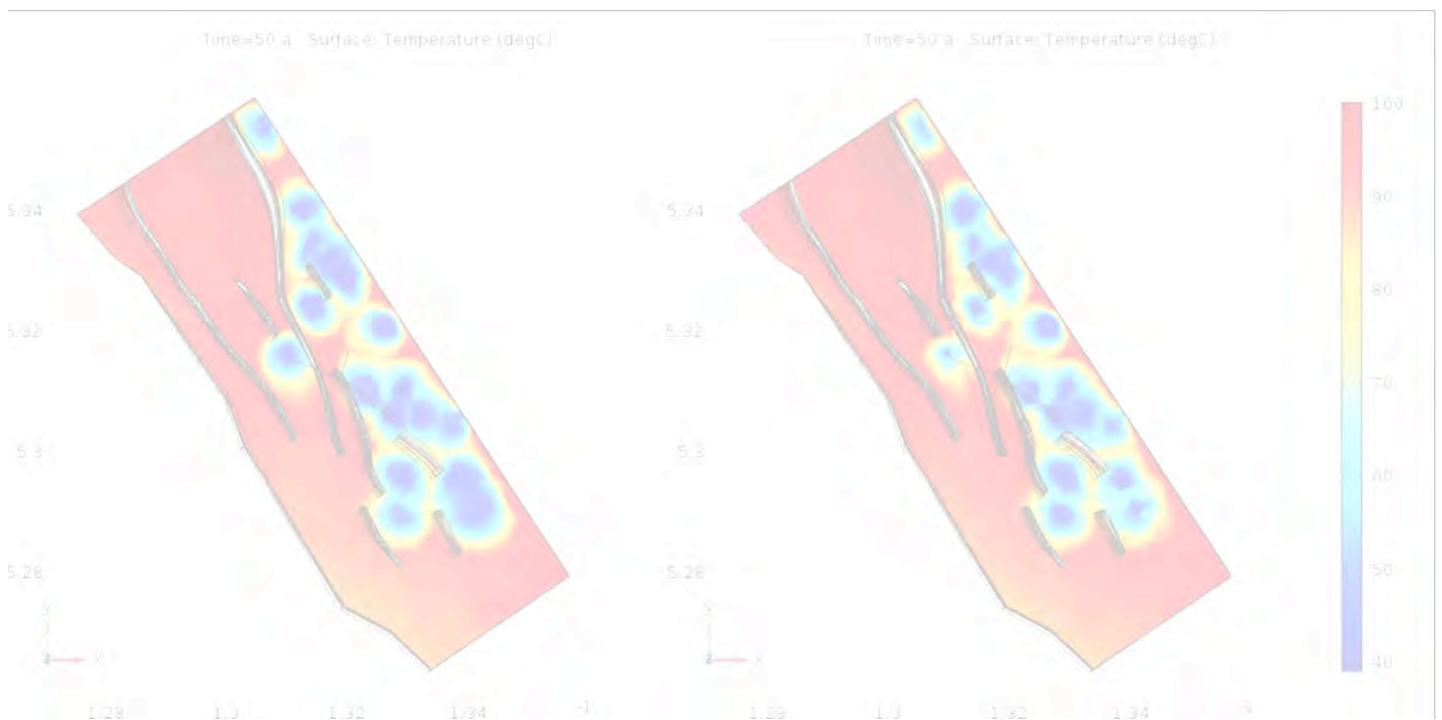
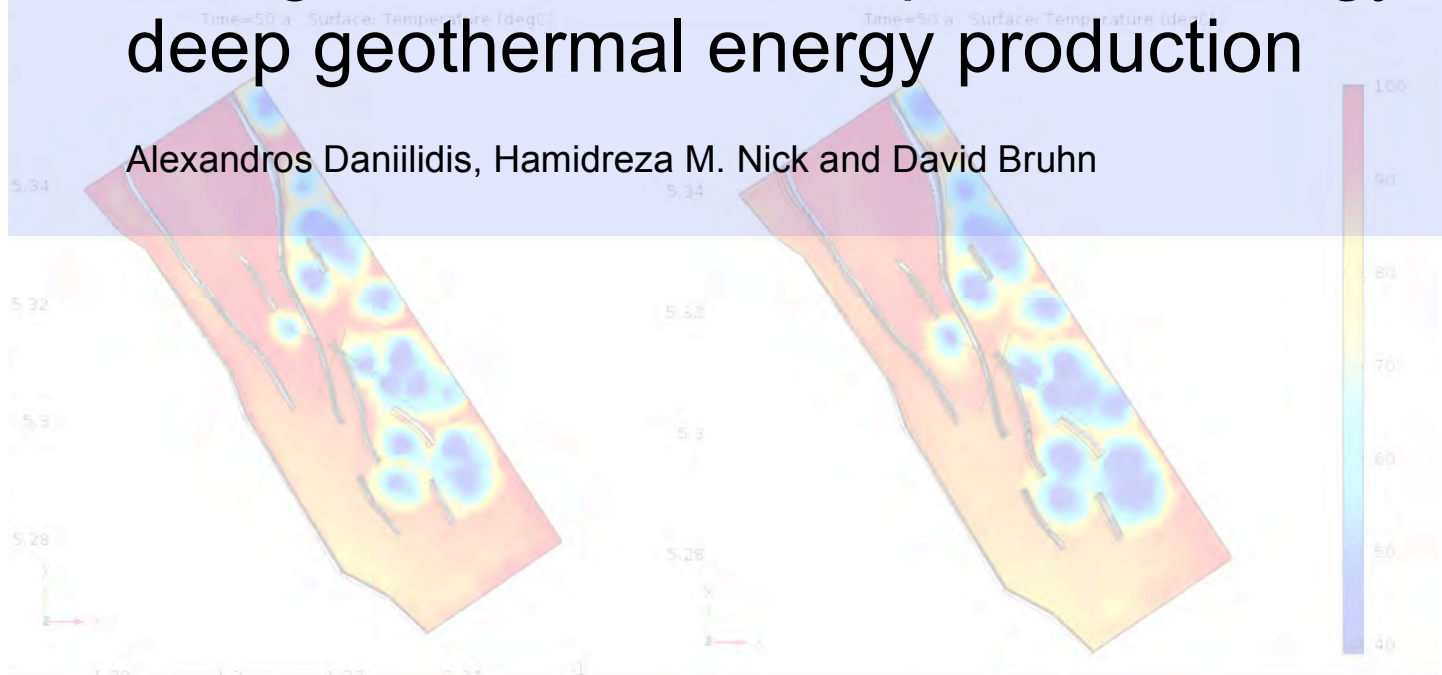


# Kennisagenda

## A regional field development strategy for deep geothermal energy production

Alexandros Daniilidis, Hamidreza M. Nick and David Bruhn



Principal investigator: Hamidreza M. Nick

The work presented in this report has been funded by:



Steering committee:



# Contents

1	Introduction	5
2	Coordinated doublet deployment	5
3	Model Completion	8
3.1	Design and inputs	8
3.1.1	One doublet bounded by two faults (1D2F)	9
3.1.2	Two doublets one fault (2D1F)	10
3.2	Modelling approach	11
3.2.1	Governing physics	11
3.3	Well model	12
3.4	Initial and Boundary conditions!	13
3.5	Heat In Place (HIP)	13
3.6	System lifetime and NPV	13
3.7	Results: One doublet bounded by two faults (1D2F)	14
3.7.1	Cold water front	14
3.7.2	Fault distance, throw and reservoir architecture effect on lifetime	17
3.7.3	NPV overview	19
3.7.4	Energy recovery	20
3.7.5	1D2F summary	21
3.8	Results: Two doublets separated by a fault (2D1F)	22
3.8.1	Fault permeability impact	22
3.8.2	Single developer – two individual developers	23
3.8.3	Result sensitivity	24
3.8.4	2D1F Summary	26
4	Field application	27
4.1	Realistic 3D model	27
4.2	Considered scenarios	28
4.3	Results	30
4.4	Monitoring	34
5	Conclusions	36
6	References	37
7	Acknowledgements	38
	Appendices:	38



# 1 Introduction

A major concern in developing deep geothermal projects in the Netherlands is that geothermal field development studies are often limited to the license area and do not investigate possible interference with nearby projects in regional settings. This results in projects which may be far from optimal and limits the use of the available resource. Currently production licence areas are often issued based on the expected extent of the reinjected cold water plume on the moment of thermal breakthrough.

It is important to develop routines for geothermal development projects considering the regional scales (10 -100 km<sup>2</sup>) in order to be more proactive in preventing the possible above-mentioned problems and to optimise the use of the available resource. For mutual understanding of doublet owners and geothermal developers and for sustainable use of geothermal reservoirs, investigation of the whole system is essential.

The central aim of this study is to improve geothermal doublets exploitation efficiency at regional scale. This translates into the following major objectives:

- Identifying the key physical and human controlled parameters (flow rate, well placement, injection temperature, heterogeneity, reservoir thickness and width) controlling NPV, sweep efficiency, lifetime and energy production of geothermal doublets.
- Developing of a routine for improved prediction of geothermal energy production at the regional-scale (10-100 km<sup>2</sup>) based on data availability and probabilistic analysis.
- Evaluate the interference between nearby deep geothermal projects that tap the same resource, and develop workflow and monitoring strategies minimizing the risk of interference.

These help to increase the economic feasibility of geothermal energy for domestic and industrial heating by optimizing the energy production per reservoir volume while minimizing the negative interferences. Such regional-scale modelling approach allows the decision makers, such as municipalities and investors, not only to know and regulate which activities take place, but more importantly, to pose conditions on how these are carried out.

The report follows based on previous studies (Willems et al., 2017a,b), the impact of two different deployment strategies: a) 'first come, first served' deployment, and b) coordinated doublet deployment; on heat recovery are illustrated at the regional-scale of WNB. This objective is to exemplify the effectiveness of utilising a coordinated doublet deployment for increasing the productivity to levels that enable economic use of natural geothermal systems at large-scales.

A numerical model of non-isothermal flow - honouring reservoir structure - embedding detailed geological heterogeneity for calculating energy recovery from geothermal doublet systems at regional-scale is developed and utilised to study the key physical and human controlled parameters controlling NPV, sweep efficiency, lifetime and energy production of geothermal doublets under realistic conditions. This can be used to develop routines for improved prediction of geothermal energy production at the regional-scale.

Further extensive analyses on heterogeneous systems is done to study the interference between deep geothermal doublets and to suggest monitoring strategies minimizing the risk of interference. At the end, a three-dimensional geological model at the regional-scale in the Rotliegend basin (Middenmeer concession) is utilised to illustrate the impact of different well placements on improve the performance of a geothermal system.

## 2 Coordinated doublet deployment

The first Dutch geothermal sites proved that Hot Sedimentary Aquifers exploitation can play an important role in a future low-carbon energy mix. In this study, we estimate that with the expansion rate of the past four years, geothermal heat production from Lower Cretaceous Hot Sedimentary Aquifers could cover up to 20% of the heat demand in the province of Zuid-Holland by 2050. Although this is a significant amount, we show in this study that only 1% of the potentially

recoverable heat will be recovered by 2050. This is because of inefficient doublet deployment on a ‘first-come, first served’ basis with operational parameters that focus on objectives of small decentralised heat grid demands. Instead, similar to the common-practise approach in the hydrocarbon industry, a regional coordinated ‘masterplan’ approach could be used to increase heat recovery (Figure 1)

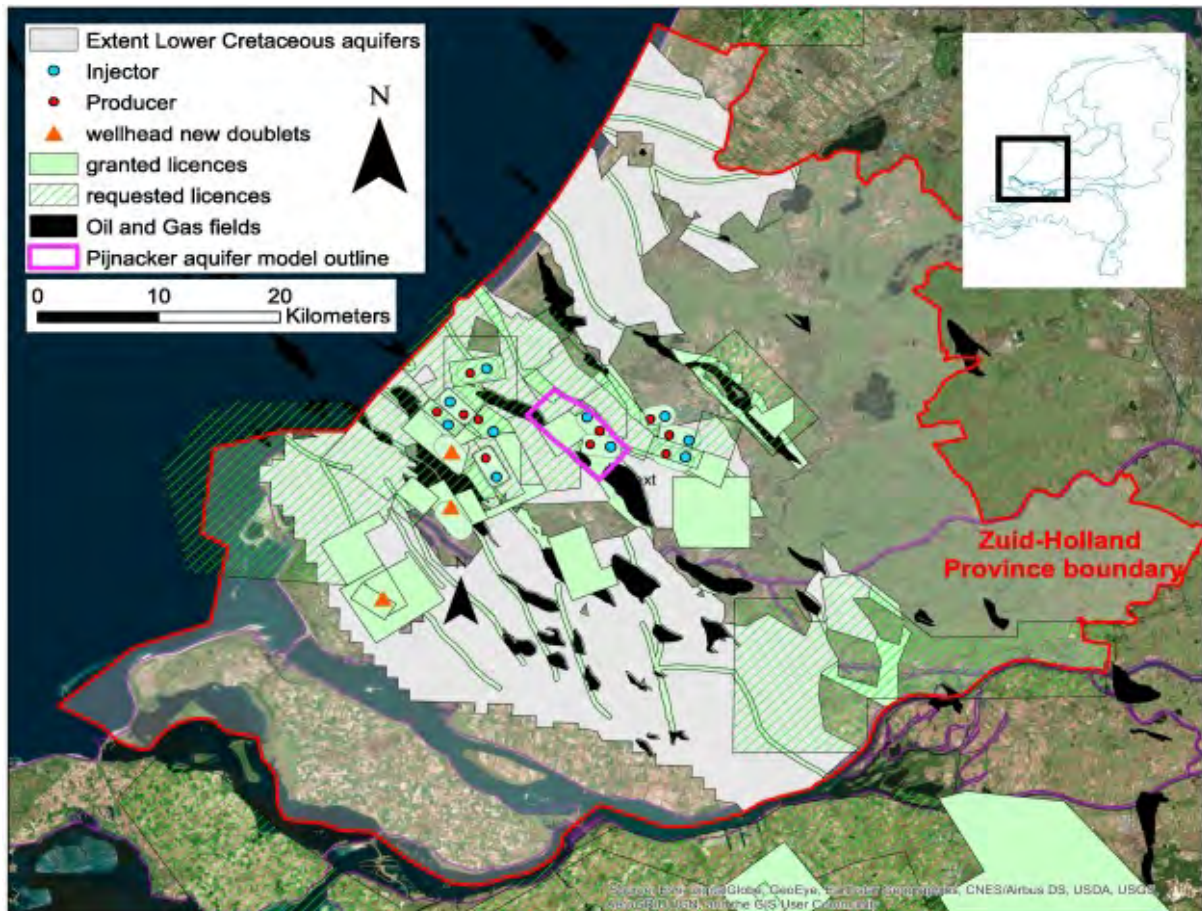


Figure 1 Overview of geothermal activity in the province of Zuid-Holland (red border). Red and blue dots indicate the location of injectors and producers at aquifer level. For three new doublets the well trajectories are unknown and only the wellhead (i.e. the surface termination of a wellbore) locations are shown (orange triangles). Figure source: (C. J.L. Willems & M. Nick, 2019)

When the installed capacity will continue to grow with 13 MW<sub>th</sub>/yr, some 50 doublets will have been realised by 2050. Assuming that the average injector-producer spacing of the doublets remains 1.6 km it was calculated that these 50 doublets will cover some 225 km<sup>2</sup>. This is approximately 20% of the surface area below which Lower Cretaceous aquifers are expected to have sufficient potential according to Pluymaekers et al., (2012). When the expansion rate of geothermal exploitation is faster, for example 24 MW<sub>th</sub>/yr like in the past four years, some 80 doublets can be realised by 2050, occupying some 35% of the surface area below which the aquifer has sufficient potential. Note that in both expansion scenarios, not even 1% of the HIP will be recovered in 2050 and pressure interference will become increasingly imminent (Willems et al., 2017a). Therefore, Figure 2 shows that a change in doublet deployment and permitting strategy is required to increase the number of doublets and heat recovery efficiency in this basin.

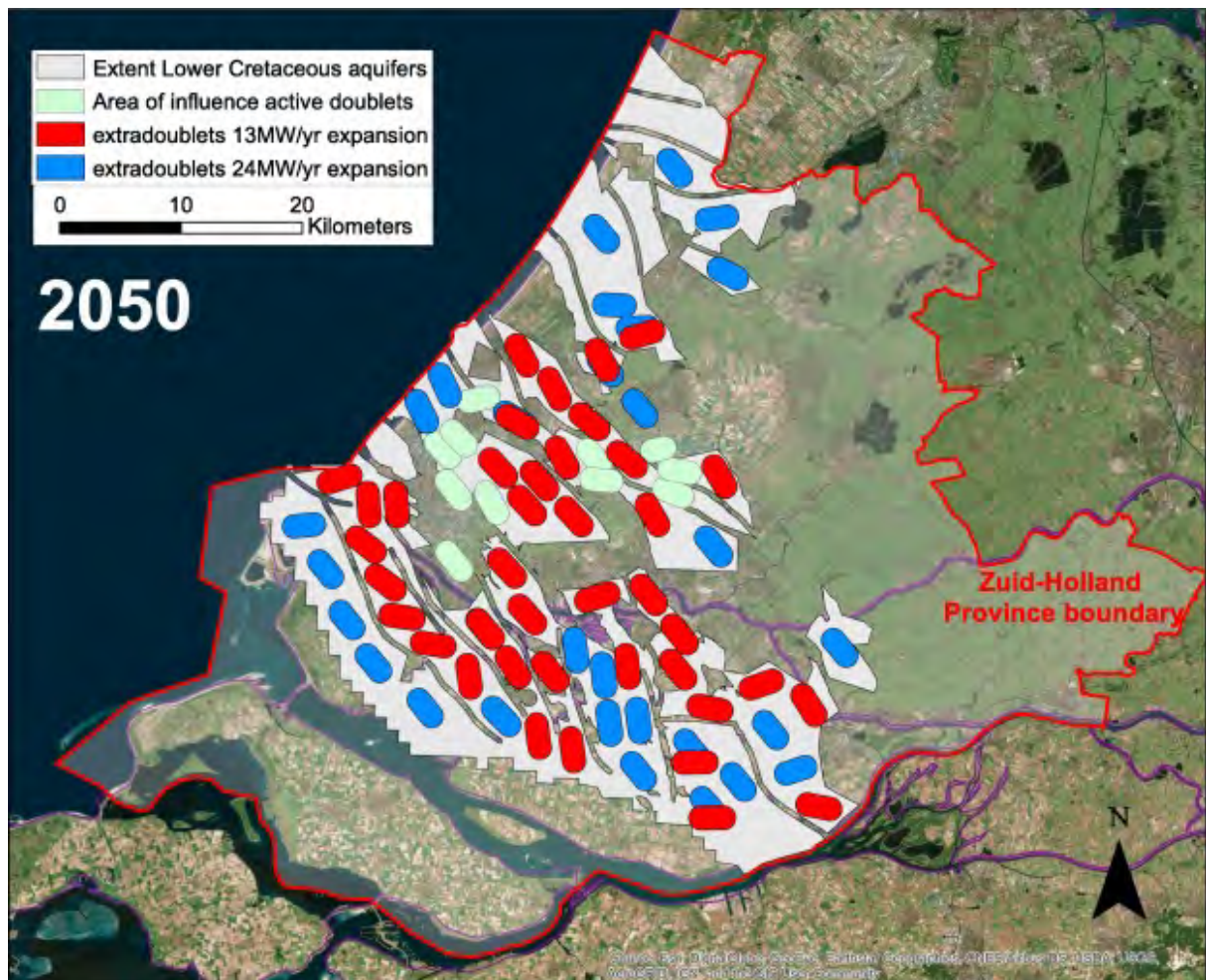


Figure 2. Surface area covered by geothermal doublets in 2018 (green) and 2050 with expansion rate of 13  $MW_{th}/yr$  (red) or 25  $MW_{th}/yr$  (blue). The red line outlines the extent of the Province of Zuid-Holland and the filled grey polygon indicates the area with assumed sufficient geothermal potential of the Lower Cretaceous aquifers according to *Pluymaekers et al.* (Pluymaekers et al., 2012). Figure source: (C. J.L. Willems & M. Nick, 2019)

### 3 Model Completion

Direct use geothermal systems are mostly developed in conduction dominated fields (Moeck, 2014). These systems are alternatively referred to as Hot Sedimentary Aquifers (HSA), hydrothermal systems, or deep, low enthalpy geothermal systems (Barbier, 2002; Daniilidis et al., 2016; Willems et al., 2017b). A doublet configuration with one producer and one injector well is commonly used (Crooijmans et al., 2016; Vik et al., 2018).

Additionally, the evaluation of economic output of such a system can vary according to the considered parameters (Daniilidis et al., 2017; Limberger et al., 2018). A geological factor that has been found to influence the produced energy of a geothermal doublet is fault permeability (Blöcher et al., 2010; Daniilidis et al., 2016; Salimzadeh & Nick, 2019; Salimzadeh et al., 2018)

In this section an overview of the models run for the KA study is presented. The quantitative models use non-isothermal flow embedding geological heterogeneity for calculating energy recovery from geothermal doublet systems. Key physical and human controlled parameters are considered such as reservoir permeability, flow rates, well placement and spacing. The system is examined in terms of NPV, HIP recovery, system lifetime and energy production under realistic conditions.

#### 3.1 Design and inputs

The reservoir is comprised of three layers, 50 m thick each. These are confined between overburden and basement layers that exhibit very low porosity and permeability (Table 1), equivalent to impermeable rocks. The inclusion of an overburden and basement layer in the model is important as their thermal properties can have a significant effect on the produced energy (Daniilidis & Herber, 2016), and the thermal recharge can affect the system lifetime (Saeid et al., 2014). These confining layers have a thickness of at least 250 m to ensure sufficient thermal recharge over the simulation duration of 100 years. The faults are a planar, vertical surface that extends 100 m above and below the reservoir layers. The throw of the fault takes different values.

Two different base models are considered. The first base model includes a single doublet bounded by two faults (1D2F). The second based model includes two doublets separated by a single fault (2D1F). These models and their respective inputs are detailed below. Both models share the inputs of Table 1.

*Table 1. The physical properties of the model components. The reservoir, over and underburden layers have a vertical permeability an order of magnitude lower that the horizontal. The fault permeability is assigned to the normal to its plane, while along the fault plane the permeability is an order of magnitude higher.. The fault permeability values are determined by the inputs from Table 2.*

	Porosity (%)	Permeability (m <sup>2</sup> )	Thermal conductivity (W/(m·K))	Specific heat capacity (J/(kg·K))	Density (kg/m <sup>3</sup> )
max	20	$4.93 \times 10^{-13}$	2.9	970	2200
mid		$9.87 \times 10^{-14}$			
min		$4.93 \times 10^{-15}$			
Fault	20	Fault plane: $k_{\text{Fault}} \times 10$ Normal to fault plane: $k_{\text{Fault}}$	2.9	970	2200
Overburden and basement	1	$9.86 \times 10^{-18}$	2.2	1100	2400

The properties of the different model layers are listed in Table 1. The reservoir architecture is captured by alternating the sequence of the three reservoir layers and their respective flow properties. The reservoir layers exhibit the same porosity but their permeability takes one of the discrete values: max ( $4.93 \times 10^{-13} \text{ m}^2$ ), mid ( $9.87 \times 10^{-13} \text{ m}^2$ ) and min ( $4.93 \times 10^{-15} \text{ m}^2$ ). Reservoir permeability is isotropic on the horizontal plane, while the vertical permeability is an order of magnitude lower.

The fault permeability of the normal to the fault plane is an order of magnitude lower than along the fault plane (Table 1), which is isotropic. Fault permeability takes three values: i) sealing, which is three orders of magnitude lower than the min layer of the reservoir and the same as the overburden and basement confining layers, ii) transparent, which is the same as the max reservoir layer and can be seen as only examining the impact of fault displacement and iii) conduit, which is two times higher than the max reservoir layer. The fault and reservoir layers have the same values of thermal conductivity and specific heat capacity. Porosity and permeability is the same for overburden and basement layers (1 % and  $9.86 \times 10^{-18} \text{ m}^2$  respectively).

The well diameter is 21.59 cm (8.5") for the low flow rate case of  $100 \text{ m}^3/\text{h}$  and 25.4 cm (10") for the high flow rate case of  $400 \text{ m}^3/\text{h}$ . Table 4 summarizes the input used for the NPV calculations.

### 3.1.1 One doublet bounded by two faults (1D2F)

The model includes a doublet positioned in a block that is bounded by two faults. The width of the central block is fixed to 800 m while the spacing of the well doublet is varied between 600 m and 1000 m. The wells are aligned parallel to the faults. The fault plane itself has a thickness of 10 m; this thickness is always outside of the central block. The two faults have an offset that is controlled by the type of faulting and the specified fault throw (see also Table 2 and Figure 3). The fault throw takes values of 50 m, 75 m and 150 m. Respectively, these represent: bringing two consecutive reservoir layers aligned across the fault surface, having an overlap between two layers on each side of the fault and having a complete disconnection of the reservoir layers across the fault surface. The fault throw is always the same for both faults, regardless of the faulting type. Three faulting types are considered, namely series, graben and horst (Figure 3).

*Table 2. The input parameters considered in the analysis. All parameter combinations are considered in an experimental design that results in a dataset of 2430 simulations.*

Parameter	
Well Spacing (m)	1000, 800, 600
Fault Permeability ( $\text{m}^2$ )	Sealing ( $9.86 \times 10^{-18}$ ), Transparent ( $4.93 \times 10^{-13}$ ), Conduit ( $9.86 \times 10^{-13}$ )
Fault Throw (m)	50, 75, 150
Fault Type	Series, Graben, Horst
Reservoir architecture	min/mid/max, max/min/mid, min/max/mid
Flow rate ( $\text{m}^3/\text{h}$ )	100, 400
Doublet Position (m)	W50, W100, W200, center, E200, E100, E50

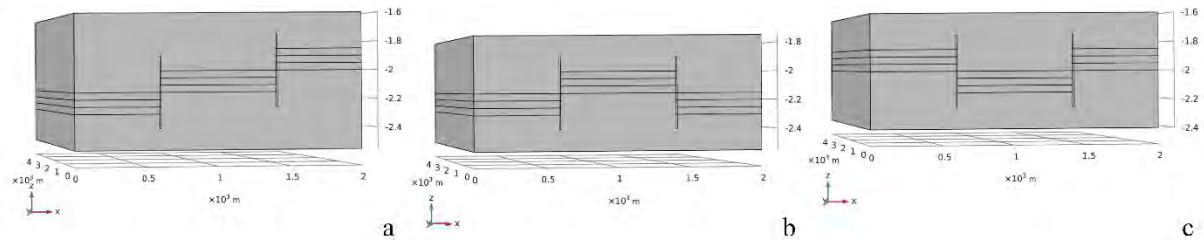


Figure 3. Model geometries for the different fault types: (a) series, (b) horst and (c) graben. The horst and graben fault types result in a symmetric geometry while the series type of fault in an asymmetric one. The faults always extend 100m above or below the respective layers they intersect. Here a fault throw of 150m is shown for all three cases.

Due to the fact that the graben and horst faulting types result in a symmetrical model, the doublet positioning for these two fault types is only varying between middle and 50 meters away from the west fault (W50). For the fault type in series, the doublet is positioned 50 m away from the west fault (W50) up to 50 m away from the east fault (E50).

The top of the reservoir in the central block is always positioned at 2 km depth. A subdomain area is assigned with dimensions of the well spacing by two times the well spacing, as shown in Table 1.

### 3.1.2 Two doublets one fault (2D1F)

Two doublets are positioned in the system, one in the west and one in the east block of the model. The well spacing of the wells in a single doublet is 800 m and equals the spacing between the doublets, as this has been shown to be the most beneficial configuration for lifetime and NPV (Willems et al., 2017). The wells in a single doublet are oriented along the N-S direction. The west doublet has the producer on the north and injector on the south, while the east doublet has either the same (tram) or the opposite configuration (checkerboard) (see also Figure 14).

Table 3. Input considered in the analysis consisting of 128 reservoir simulations.

Parameter	Values	Units
Fault Throw	50 ,75	(m)
Fault permeability	Normal to fault plane: $9.87 \times 10^{-18}$ (sealing – 0.01 mD), $4.93 \times 10^{-13}$ (conduit – 1 D) Fault plane: Normal to fault plane·10	(m <sup>2</sup> )
Reservoir layers (top to bottom)	min/mid/max, min/max/mid	-
Well configuration	Tram, Checkerboard	-
Flow rate	100, 250	m <sup>3</sup> /h
Well spacing	800	m
Top reservoir depth	2000	m
Fault distance	400, 200, 100, 50	m

An overview of alternative fault positions and an impression of the meshed domain are presented in Figure 4. In order to make the results from each doublet cross comparable, the lifetime definition is normalized to a percentage change with respect to the production temperature at time zero (see Figure 5 and section System lifetime and NPV).

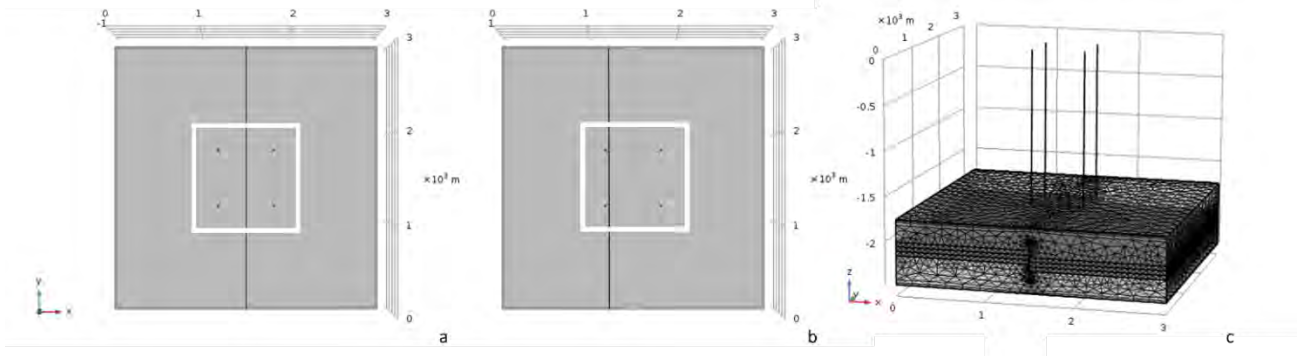


Figure 4. Top view of the model with the fault positioned at the middle – 400 m (a) and 50 m away from the west doublet (b). The white highlighted area designates the influence area in which the HIP is calculated. The subdomain area size marked in white is two times the well spacing for both sides. Example of meshed domain for a horst type of faults in (c) angled view. The number of elements ranges between 180k to 310k depending on the geometry configuration.

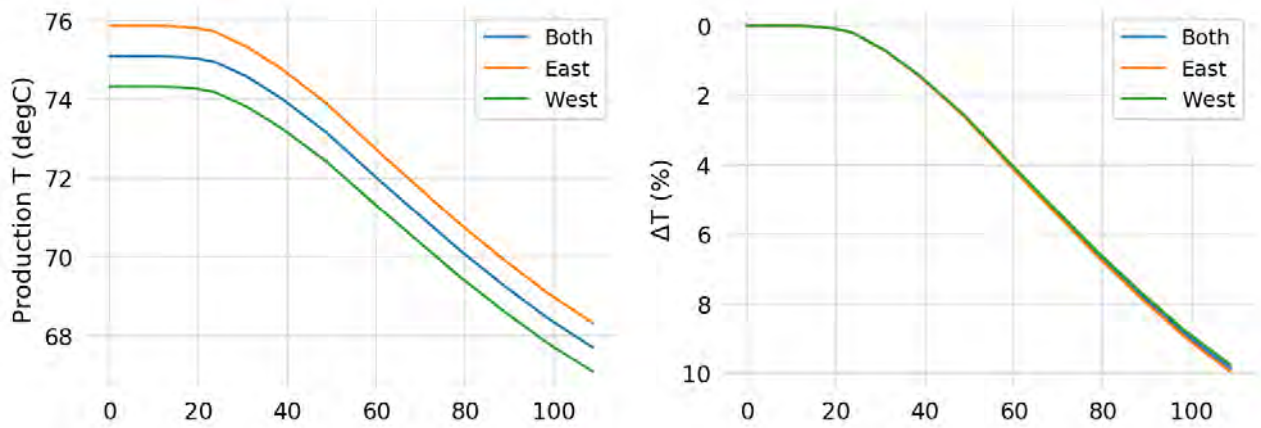


Figure 5 Normalizing the production temperature to a percentage change compared to the initially produced temperature allows for cross comparison between different models.

## 3.2 Modelling approach

### 3.2.1 Governing physics

A Thermal-Hydraulic (TH) model is built in COMSOL Multiphysics. The Energy Balance describes the heat transfer in the model as follows:

$$\rho C \frac{\partial T}{\partial t} + \rho_f C_f \mathbf{q} \nabla T - \nabla(\lambda \nabla T) = 0 \quad [1]$$

in which  $T$  (K) is the temperature,  $\rho$  the mass density ( $\text{kg}/\text{m}^3$ ),  $C$  ( $\text{J}/(\text{kg}\cdot\text{K})$ ) the specific heat capacity,  $\lambda$  ( $\text{W}/(\text{m}\cdot\text{K})$ ) the thermal conductivity,  $\mathbf{q}$  (m/s) the Darcy velocity and suffixes  $f$  and  $s$  refer to the fluid and the solid matrix respectively. The thermal conductivity and volumetric heat capacity of the system is computed based on the respective fluid and rock values separately according to:

$$\lambda = (1 - \varphi)\lambda_s + \varphi\lambda_f \quad [2]$$

and

$$\rho C = (1 - \varphi)\rho_s C_s + \varphi\rho_f C_f \quad [3]$$

in which  $\varphi$  is rock porosity. The pressure field is computed based on the continuity equation according to:

$$\varphi \frac{\partial \rho_f}{\partial t} + \nabla \cdot (\rho_f \mathbf{q}) = 0 \quad [4]$$

where the flux  $\mathbf{q}$  (m/s) is defined by Darcy's law:

$$\mathbf{q} = -\frac{k}{\mu} (\nabla P - \rho_f g \nabla z) \quad [5]$$

in which  $k$  is the intrinsic porous medium permeability ( $\text{m}^2$ ),  $\mu$  the dynamic viscosity of the fluid (Pa·s),  $g$  the acceleration of gravity ( $\text{m/s}^2$ ) and  $P$  the hydraulic pressure (Pa).

The fluid density and viscosity are a function of temperature according to:

$$\rho_T = 838.466135 + 1.40050603 \cdot T - 0.0030112376 \cdot T^2 + 3.71822313 \cdot 10^{-7} \cdot T^3 \quad [6]$$

$$\mu_T = 1.3799566804 - 0.021224019151 \cdot T + 1.3604562827 \cdot 10^{-4} \cdot T^2 - 4.6454090319 \cdot 10^{-7} \cdot T^3 + 8.9042735735 \cdot 10^{-10} \cdot T^4 - 9.0790692686 \cdot 10^{-13} \cdot T^5 + 3.8457331488 \cdot 10^{-16} \cdot T^6 \quad [7]$$

The consideration for the mesh was to enable high enough result accuracy while maintaining a reasonable run time for the simulation ensemble. The model is meshed using a higher number of tetrahedral elements inside the reservoir layers, where flow is taking place. An additional refinement is performed around the wells where the higher flow velocities occur. Moreover, within the subdomain area (see Figure 6) a further refinement is applied ensuring a minimum of three vertical cells per reservoir layer. The minimum element size inside the reservoir domain is 5m and the maximum is 70m. We have also performed a mesh analysis study (not shown here) to confirm that the chosen mesh sizes provide sufficient accuracy of model results. Note that the geomechanical modelling of the system is out of the scope this study.

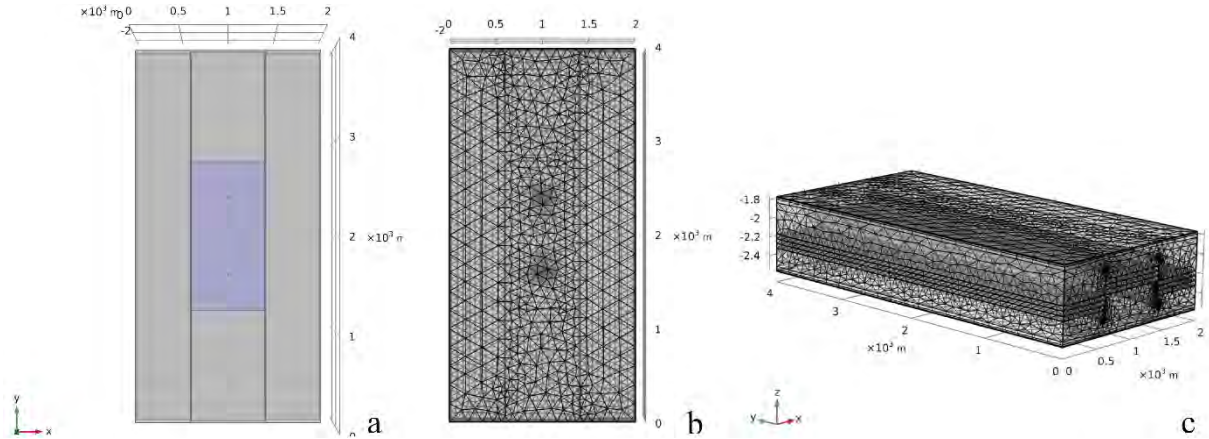


Figure 6. Subdomain around the doublet (a), shown here for a well spacing of 800 m. The subdomain area has a size of two times the well spacing on the long side and one time the well spacing on the short side. In the event that the subdomain area extends beyond the faults, the corresponding part of the reservoir at that depth is included in the calculation. Example of meshed domain for a horst type of faults in (b) top and (c) angled view. The number of elements ranges between 145k to 195k depending on the geometry configuration.

### 3.3 Well model

A simple well model is implemented in order to accommodate a flow rate control on the wells. The well rate is partitioned to each layer based on the ratio of the  $kh$  (permeability-thickness) of each layer to the  $kh$  of the whole reservoir interval as formulated in (Jalali, Embry, Sanfilippo, Santarelli, & Dusseault, 2016) :

$$q_i = (k_i h_i / \sum_1^n k_i h_i) q_{total} \quad [8]$$

in which  $k_i$  ( $\text{m}^2$ ) and  $h_i$  (m) are the permeability and thickness of layer  $i$  respectively,  $n$  is the total number of layers and  $q_i$  and  $q_{total}$  are the layer  $i$  flow rate and the total flow rate respectively.

Model inputs

### 3.4 Initial and Boundary conditions

A geothermal gradient of 31 °C/km (Bonté, Wees, & Verweij, 2012) and a hydrostatic pressure gradient of 10 MPa/km are applied as initial conditions to the whole model domain. A pressure boundary condition is applied to the sides of the model, equal to the initial values calculated through the hydrostatic pressure gradient.

The model boundary conditions for flow include no flow boundaries on the top and bottom surfaces of the model, while all side boundaries are open to flow. Temperature boundaries include a fixed temperature at the top and bottom of the model (top and bottom of the over/underburden) according to the initial conditions, while all side boundaries are open to heat transfer.

### 3.5 Heat In Place (HIP)

The calculation of the Heat In Place (HIP) is carried out according to :

$$HIP = \int_0^V_{subdomain} \left( (\rho_f c_f \varphi + \rho_s c_s (1 - \varphi)) (T - T_{inj}) dV \right) \quad [9]$$

The HIP is calculated before any production takes place. The lower bound of the temperature difference is taken as  $T_{inj}$  as that is the lowest threshold that can effectively be recovered from the system (Garg & Combs, 2015). The HIP is calculated only inside the subdomain area (Figure 6). The subdomain area has a size of two times the well spacing on the long side and one time the well spacing on the short side

### 3.6 System lifetime and NPV

The system lifetime is reached when the condition for the temperature (°C) of the hot water from the production well

$$T_{prod_t} \leq 0.95 \cdot T_{prod_{t=0}} \quad [10]$$

is met. This condition is quite sensitive and is meant to capture the moment at which a slight change in the production temperature is measured. It therefore can be considered as worst case scenario for lifetime, bearing in mind that a temperature drop of less than 10 °C may still not compromise the operation of the geothermal system. The produced power used for the calculation of income is computed according to:

$$P_{well} = Q \rho_f c_f \Delta T \quad [11]$$

in which  $Q$  is the flow rate (m<sup>3</sup>/s) and  $\Delta T$  is the temperature difference between producer and injector wells (degC). The required pump power only considers the pressure drop in the reservoir:

$$P_{pump} = \frac{\Delta P \cdot Q}{\eta} \quad [12]$$

where  $\Delta P$  is the pressure difference between the wells and  $\eta$  is the pump efficiency. The overall system power is then calculated as:

$$P_{system} = P_{well} - P_{pump} \quad [13]$$

The cost of the wells in € is computed according to (TNO, 2018):

$$C_{well} = 375000 + 1150Z + 0.3Z^2 \quad [14]$$

where  $Z$  is the measured depth. For the high flow rate cases that utilize a larger production diameter, the above calculated  $C_{well}$  is increased by 25%. Note that the well diameter has a significant impact of the flow rate and the pressure field around the well. The NPV is then calculated as:

$$NPV = \sum_{t=0}^n \frac{CF_t}{(1+r)^t} \quad [15]$$

Where  $CF$  is the cashflow,  $r$  the discount rate,  $n$  is the project years and  $t$  the time. The cumulative produced power generated income is based on the heat price, while the pump power costs are

computed based on the electricity price (see Table 4). The NPV and HIP recovery data are selected at the point in time where the system lifetime condition is reached.

*Table 4. Inputs used in the economic calculations*

Load factor (%)	Heat price (€/MWh)	Pump cost (k€)	Pump lifetime (yrs)	Pump efficiency (%)	OpEx % of CapEx (%)	Discount rate (%)	Electricity price (€/MWh)
90	60	500	5	60	5	7	100

### **3.7 Results: One doublet bounded by two faults (1D2F)**

#### **3.7.1 Cold water front**

The shape and extent of the cold water front is affected by the effective flow path that is available based on the simulation input and the flow rate. This flow path is controlled by the reservoir architecture, the fault permeability, the doublet position in relation to the faults, the fault type and throw, the well spacing and finally the flow rate. All combinations of these parameters result in different flow paths and a different spatial distribution of the cold front. In order to visualize the qualitative behaviour of these interactions, the focus is drawn to a sub-dataset. This sub-dataset uses the higher considered flow rate (400 m<sup>3</sup>/h) and highest fault throw (150 m), while the doublet is positioned 50 m away from the west fault (W50) and the fault type is series (Figures 7 and 8).

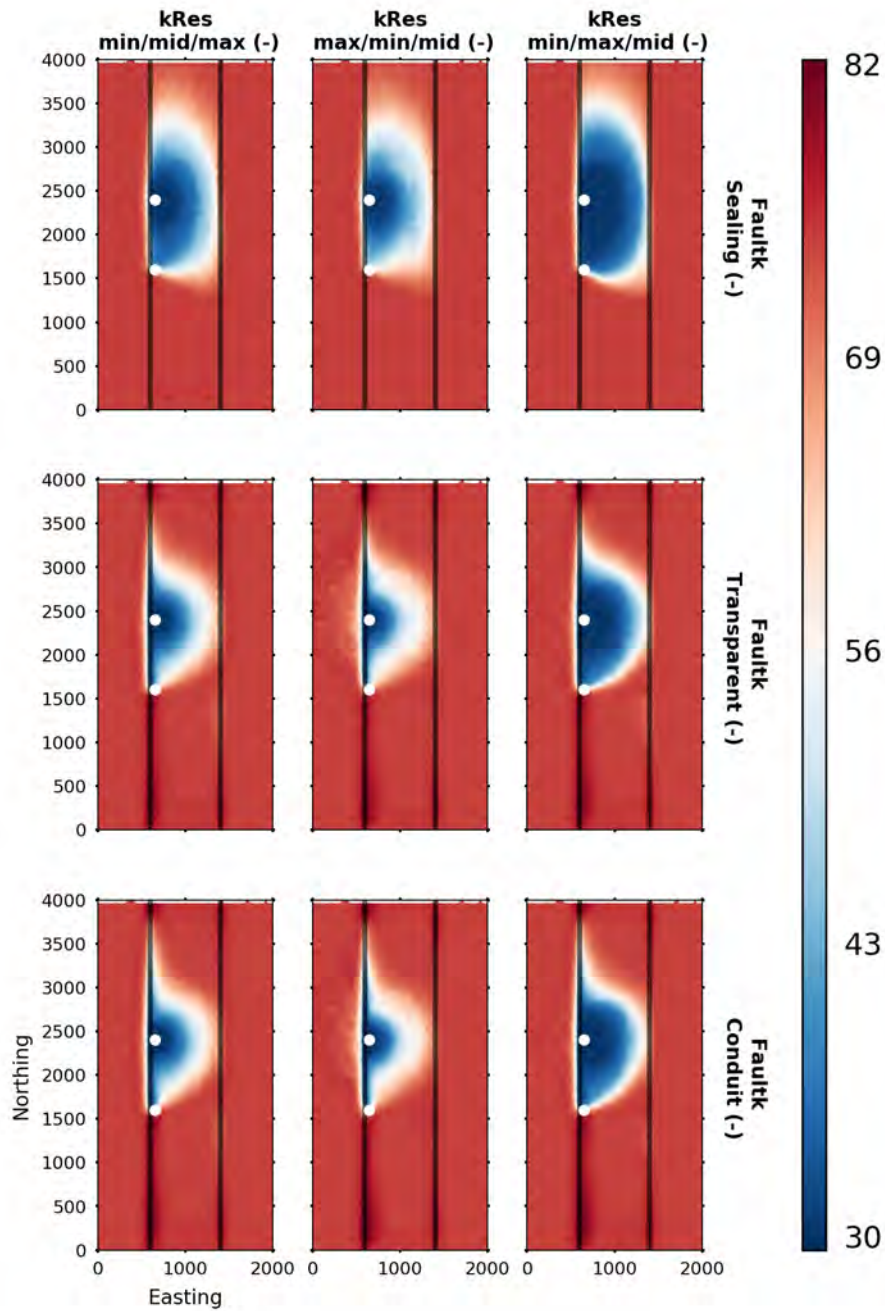


Figure 7. Cold water front top view, slice at the middle of the reservoir (depth of 2075m) for the central part of the geometry after 50 years of simulation. White dots mark the injector (North) and producer (South) wells, while dark lines mark the faults. Data shown here for the subset where WSpacing is 800m, FaultThrow is 150 m, Fault type is series, flow rate is 400 m<sup>3</sup>/h and the doublet is positioned 50m away from the west fault. The West and East parts of each subplot do not represent the same reservoir layers as they are offset by the faults.

The top view of the middle reservoir layer (Figure 7) reveals the importance of the reservoir architecture; depending on the flow properties of the middle layer of the reservoir, we can see distinctively different cold water front shapes. The main differences are observed in the extent of the influence area and the volume that is cooled down to the injection temperature of 30 °C. Both the extent and the volume are larger with higher permeability. Additionally, higher layer permeability leads to a more sharply defined edge of the cold plume, owing to the higher Peclet number (Figure 7).

A sealing fault results in a different shape and extent of the cold plume, while a similar pattern is observed between the transparent or conduit fault behaviour (Figure 7). A sealing fault compartmentalises the reservoir and essentially confined the flow within the faulted block. Proximity

to the fault boundary results in a homogeneous development of the cold front along that boundary, as is the case along the west fault (Figure 7). Between transparent and conduit faults, the shape of the cold plume remains the same for each reservoir architecture, but the extent is reduced for the conduit fault behaviour. This is due to a diversion of large parts of the flow through the fault plane to other parts of the reservoir (see also Figure 8). While this enhanced flow through the faults can act as a short circuit between the wells (see also section Fault distance, throw and reservoir architecture effect on lifetime) it also enables heat exchange between the deeper sited layers of the western block; this can be seen by the higher temperature flow around the south part of the west fault.

Additionally, a sealing fault exhibits a less widespread temperature diffusion outside its boundaries compared to transparent or conduit properties (Figure 7). The temperature is lower on the west block for the reservoir architecture that has the maximum flowing layer at the top. This means that right below the depth slice, the highest flow inside the reservoir is present and therefore we observe lower temperatures extending further away from the fault. This effect is also clear in Figure 8.

The vertical slice presented in Figure 8 better reveals the interaction between the reservoir layers and the fault plane. With a sealing fault, after 50 years of production the cold plume is limited to the inside of the central block, and heat is only extracted from the surroundings by conduction. This is clearly demonstrated by the fact that temperature interaction across the west fault only happens at the depth of the central block reservoir layers. With a transparent and conduit flow the cold water also flows along the fault plane and we observe a temperature drop around the whole height of the fault, extending beyond all production layers. After crossing the fault plane, the cold water preferentially flows in the highest permeable layer it encounters (Figure 8).

Additionally, Figure 8 allows for the identification of the different flow layers by means of their respective cold water plume extent. Interestingly, when the minimum flow layer is situated in the middle, we see that despite the flow across the layer boundaries (vertical permeability is an order of magnitude lower) and the heat extraction through conduction, the middle layer cold water front remains recessed. Lastly, even though not very pronounced, a difference in the extent of the cold water front inside the reservoir layers is observable between the transparent and conduit faults. As discussed previously, this can be attributed to the diversion of a larger part of the flow through the fault and to other parts of the reservoir for the case of a conduit fault.

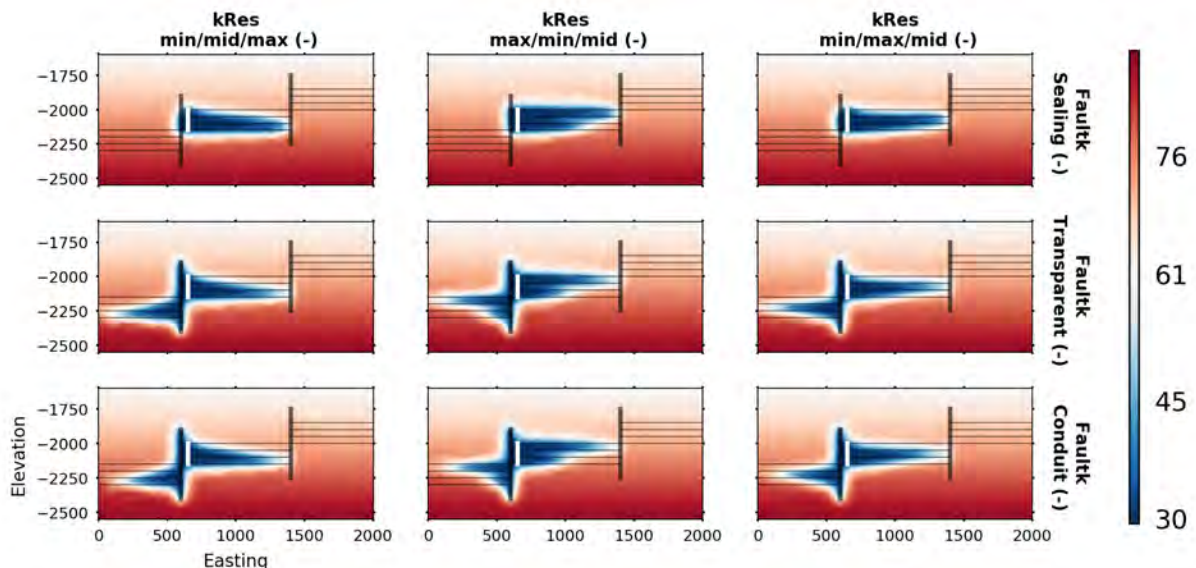


Figure 8. Cold water front, vertical slice along W-E at the point of the injector well after 50 years of simulation. Horizontal black lines represent the reservoir layer contacts, vertical black lines represent the faults and the white line represents the injection well. Data shown here for the subset where well spacing is 800m, fault throw is 150 m, Fault type is series, flow rate is 400 m<sup>3</sup>/h and the doublet is positioned 50m away from the west fault.

### 3.7.2 Fault distance, throw and reservoir architecture effect on lifetime

For the effect of the fault distance we consider the dataset with well spacing of 800 m and a flow rate of 400 m<sup>3</sup>/h, as used in all three figures (Figures 9 and 10). For the series type of faulting (Figure 9) and sealing fault the impact of reservoir architecture is obvious; having the minimum layer in the middle of the reservoir results in higher system lifetime while having the mid and max layers in the middle leads to progressively shorter lifetimes. Even though the max layer is the shallower of the three, the presence of the minimum layer in the middle still leads to the longest system lifetime of all three reservoir architectures. This effect is due to the heat extraction from the middle layer via conduction from both above (max) and below (mid) layers. This effect is further amplified as the fault permeability is increased to transparent and conduit. For a sealing fault there is no significant impact in terms of lifetime with increasing fault throw.

A fault permeability that is at the same order of magnitude as the highest permeable reservoir layer (transparent) introduces an additional, high permeable path through which the cold front can reach the injector (Figure 9). This in turn leads to a reduction of the system lifetime; this reduction is further exaggerated the closer the doublet is positioned to the fault plane. This finding is consistent for both west and east faults.

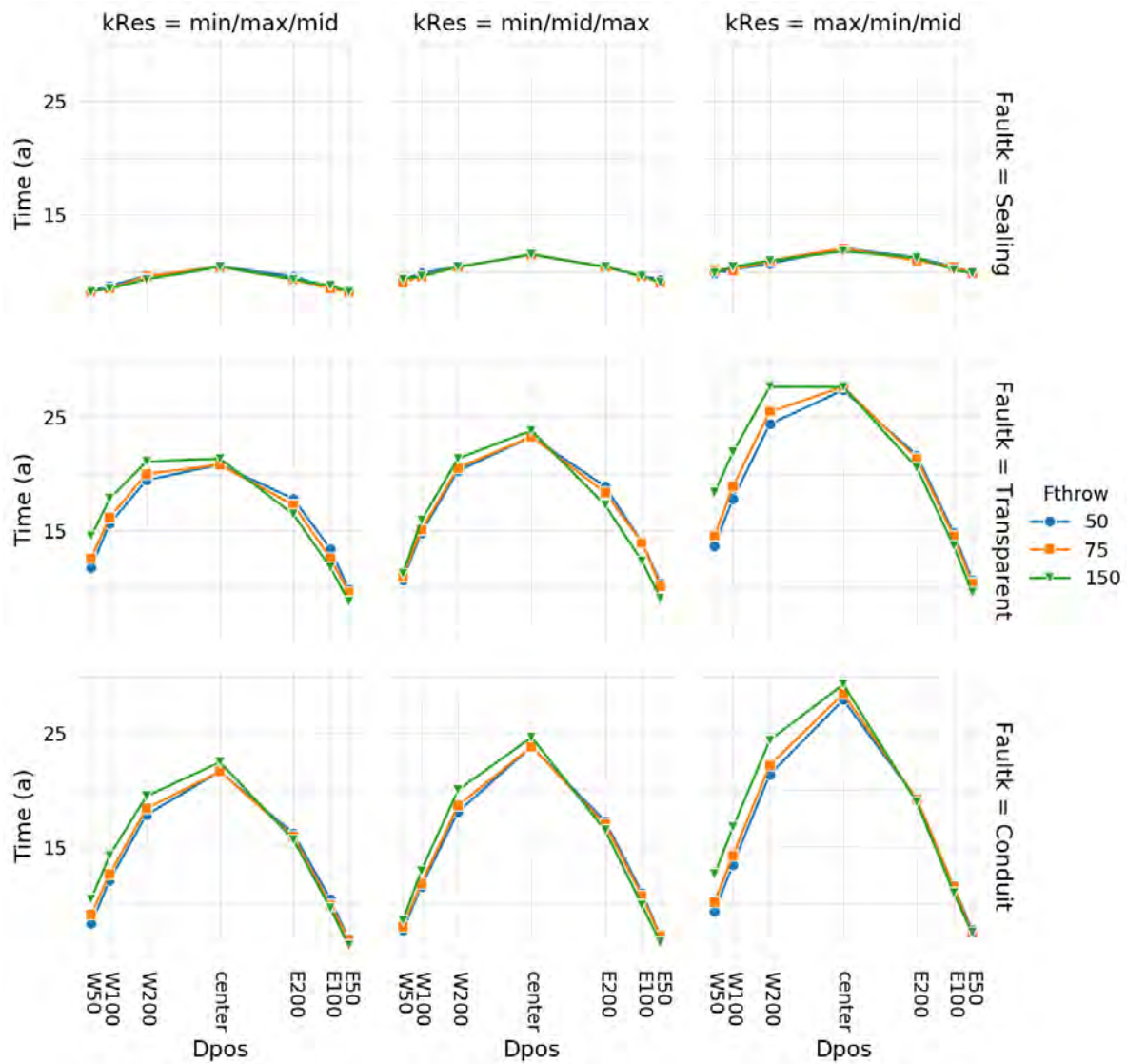


Figure 9. Effect of fault permeability, reservoir architecture, doublet distance to fault and fault throw on the system lifetime for the series fault type. A well spacing of 800m is used for all data points. The system lifetime criterion is defined in section System lifetime and NPV.

For a transparent and conduit fault, as the doublet is positioned closer to the west fault, the decrease of lifetime is less than when the doublet is positioned closer to the east fault (Figure 9). This is consistent with the west fault block always being situated deeper than the one in the east. Therefore, the fluid and temperature flow that is contributed from the west block is of higher temperature compared to the one from the east.

For a transparent fault, a large fault throw of 150m (equal to the reservoir thickness) has a smaller negative effect on the system lifetime than a small one of 50m when moving towards the west fault (Figure 9). This effect is inverted when the doublet is closer to the east fault.

The largest differences can be observed at the central positioning of the doublet, where the lifetime increases with increasing fault permeability (Figure 9). This is due to the faults diverting part of the cold water front away from the producer, therefore allowing the production temperature to remain higher for longer periods of time. Overall, moving closer to the fault results in a lifetime reduction of circa 20% for a sealing fault, to circa 50% for transparent and conduit faults alike.

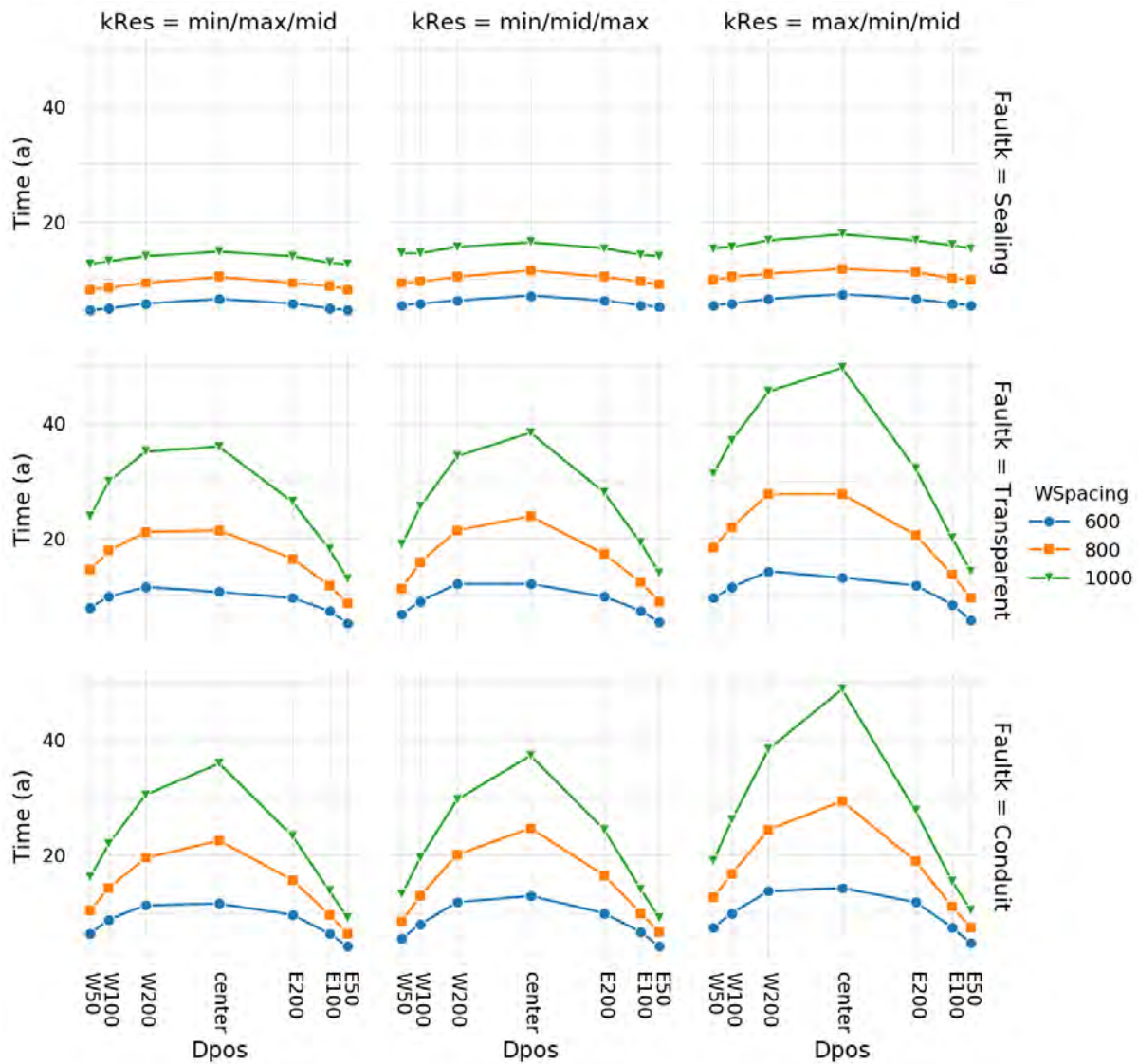


Figure 10. Effect of fault permeability, reservoir architecture, doublet distance to fault and well spacing on the system lifetime for the series fault type. A fault throw of 150m is used for all data points. The system lifetime criterion is defined in section System lifetime and NPV.

Introducing the well spacing as the varying parameter and removing the fault throw as a variable, the qualitative points made in Figure 9 are amplified or dampened (Figure 10). Increasing the well spacing to 1000 m extends the system lifetime when the doublet is positioned at the center of the block; at the

same time the effect of moving the doublet 50 m away from the fault reduces the lifetime by circa 60%. The opposite effect can be observed for reducing the well spacing; with 600 m between the injector and the producer, up to 200m away from the fault on either side has minor effects on the system lifetime.

Examining the NPV values against the cumulative produced energy (a proxy for the system lifetime) clarifies the trend further; both datasets exhibit a logarithmic type of behaviour (Figure 11). For the low flow rate the data points are more scattered, meaning that other parameters also influence mostly the generated NPV as multiple NPV values are encountered for similar amounts of cumulatively produced energy. On the other hand, the high flow rate dataset exhibits much less scatter of the data points, implying, as discussed before, that the effect of the high flow rate is decreasing the significance of the other parameters. For both flow rates there is a levelling off in terms of NPV, meaning that a longer lifetime would not yield higher economic value.

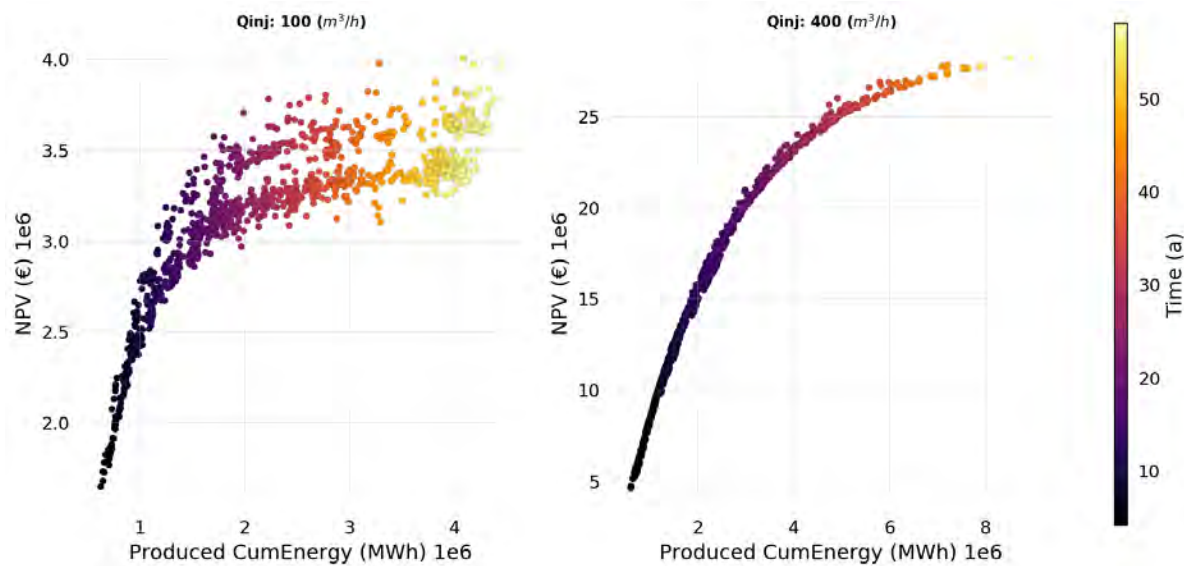


Figure 11 Produced energy and NPV for the full dataset of 2430 simulations plotted according to injection/production flow rate and coloured according to the system lifetime.

### 3.7.3 NPV overview

The impact of the doublet position to the changes in NPV is depicted in (Figure 12). For a sealing fault changing the doublet position from the center of the block leads to NPV losses; these losses amplify as the well spacing decreases for both the high and low flow rates. For both a transparent and a conduit fault the polarity of the fault offset becomes important. Positioning the doublet closer to the east fault leads to NPV losses; these loss increases the closer the doublet is positioned to the east fault. This observation is consistent for both low and high flow rates, with higher flow rates further amplifying the percentage decrease of the NPV. Increasing the fault permeability to conduit further amplifies the effect, especially for the doublet being positioned 50 m away from the east fault. The east block is positioned shallower than the central block and therefore any fluid produced from the east reservoir part will reduce the production temperature, leading to lower energy generation and possibly earlier thermal breakthrough.

Contrary to this, positioning the doublet closer to the west fault results in a more complicated effect on the NPV change. For 200 meters distance, high flow rates exhibit either a minor increase or no NPV change. Closer than 200 meters to the west fault results to an NPV decrease which is more significant for lower well spacing. The reservoir architecture seems to also be important here as having the maximum producing layer at the bottom of the reservoir section yields the largest NPV drop.

For low flow rates different effects are observed. For a transparent fault, a well spacing of 600 m leads to either no NPV effects or minor losses, while for a conduit fault these losses reach up to 10% decrease of the NPV compared to the doublet being positioned at the center. However, for a well

spacing of 800 m or 1000 m there is a slight increase in the NPV that can reach up to 10% for the reservoir architecture with the minimum flowing layer in the center. A transparent fault has almost the same effect for both well spacing values, but a conduit flow slightly differentiated between the two with the larger well spacing exhibiting higher benefits.

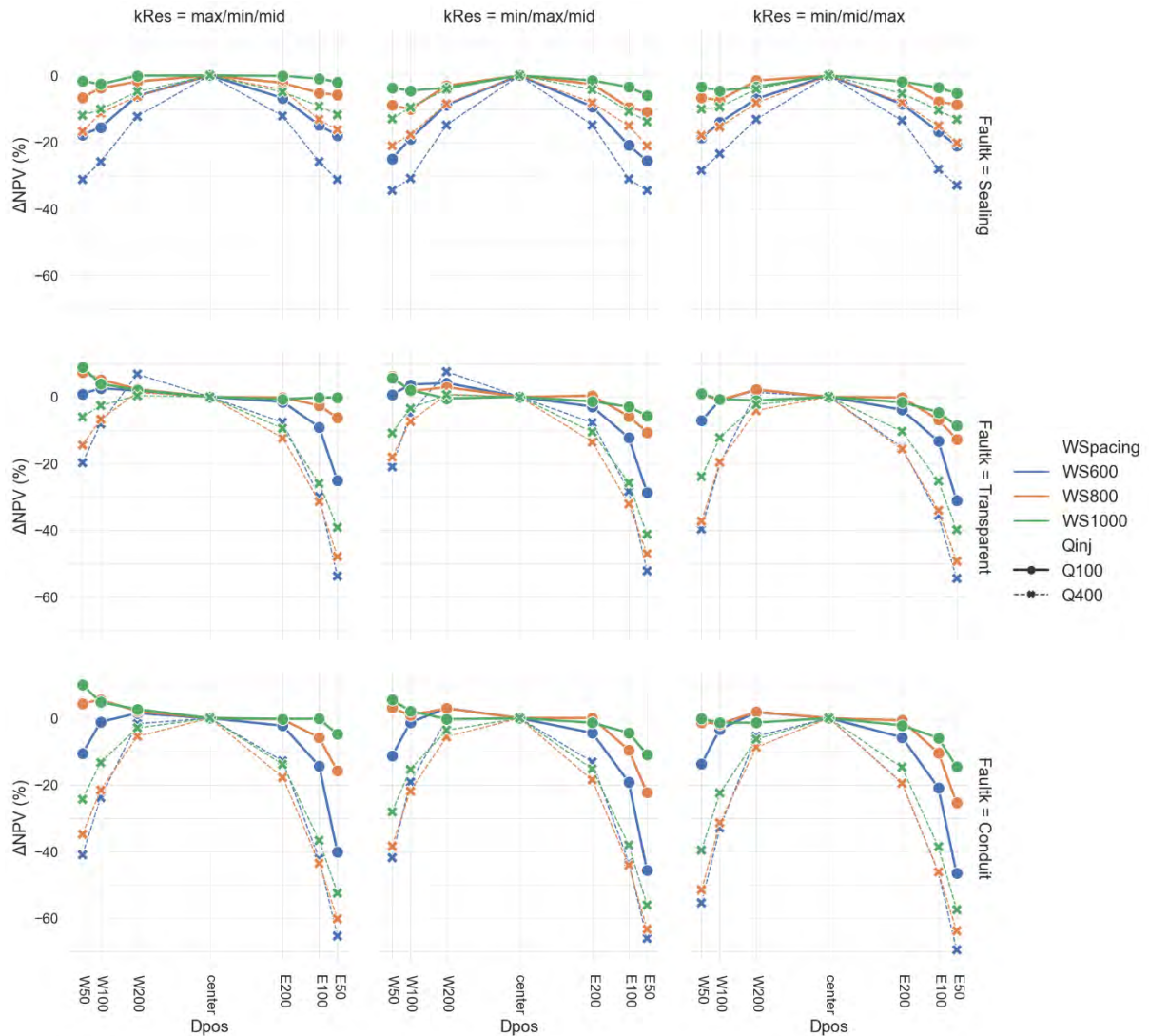


Figure 12. Changes in NPV (%) for different doublet positions in relation to the faults and different reservoir architectures for the subset of data with a series fault type and fault throw of 150m. The data are colour coded according to the well spacing and different flow rates are indicated by the lifestyles.

### 3.7.4 Energy recovery

Energy recovery as a function of system lifetime gives an indication of the rate of recovery within the defined subdomain boundaries. For the whole dataset the HIP recovery does not fall below circa 10% under any parameter combination. For low flow rates the recovery never exceeds 50 %, whereas for high flow rates it only exceeds 50% in very few cases (Figure 13). Nonetheless, a clear clustering is observed for both flow rates: the combination of well spacing and fault behaviour controls the ratio of HIP recovery to system lifetime.

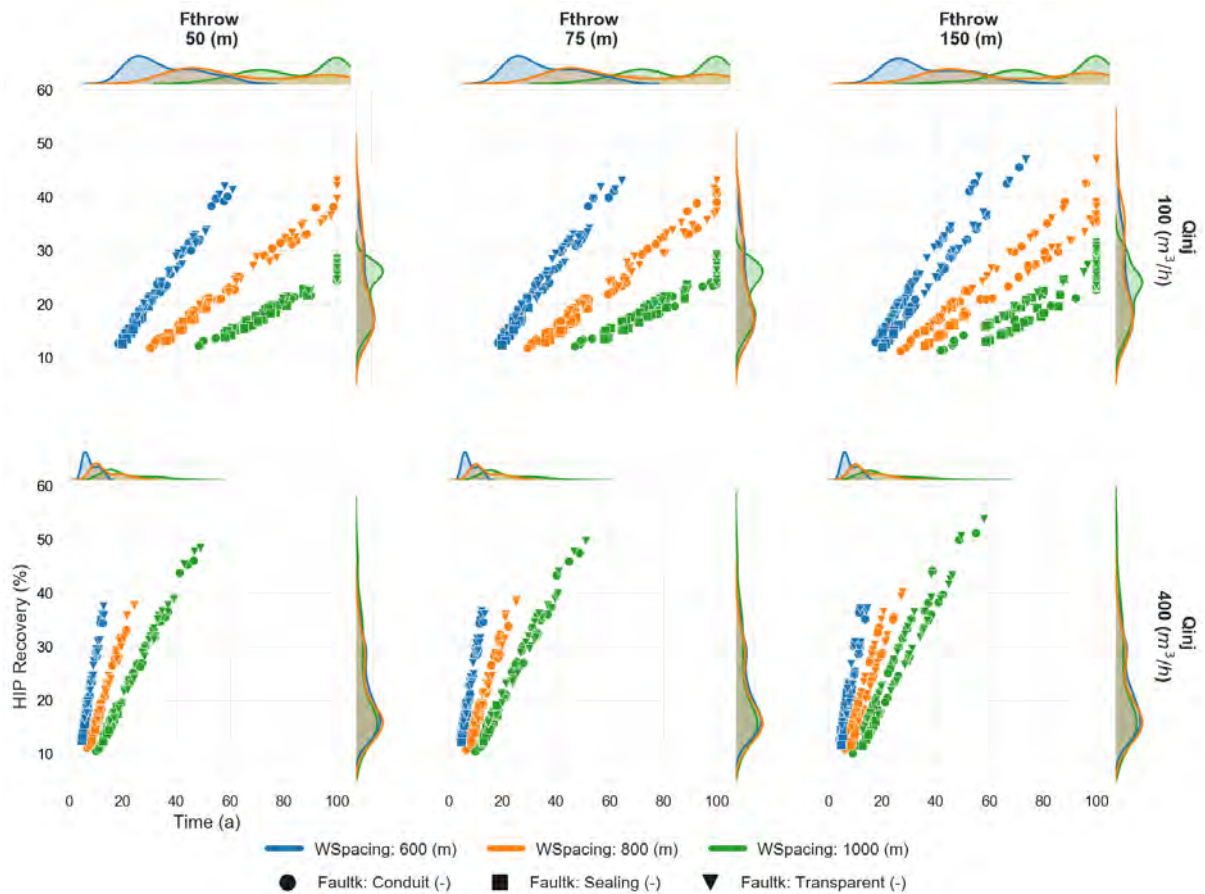


Figure 13. Percentage of recovered HIP within the subdomain boundaries of the model. Data are coloured according to the well spacing and marked according to the fault permeability.

For the low flow rate of 100 m<sup>3</sup>/h a higher separation can be seen between the different well spacing clusters in terms of system lifetime, while for the high flow rate of 400 m<sup>3</sup>/h the well spacing clusters are closer together. A higher flow rate leads to a comparable heat recovery values with the low flow rate, but this is achieved in a shorter system lifetime. The small decrease in terms of recovered HIP between the high and low flow rate could be attributed to lower flow rates sweeping a large part of the reservoir and to high flow rates reaching an earlier thermal breakthrough.

### 3.7.5 1D2F summary

The analysis includes 2430 unique Hydraulic Thermal (HT), 3D reservoir simulations. Considerations of physical parameters include the fault type and fault throw, flow properties of reservoir layers and faults, while operational parameters include well spacing, well positioning and flow rate.

The characterization of fault flow properties is more significant compared to the fault offset. Additionally, system lifetime is less affected by the presence and flow behaviour of faults when a smaller well spacing is utilized. The fault flow properties have a significant impact to the shape and extent of the cold plume and therefore the system lifetime. In absolute numbers, faults that enable fluid flow lead to longer thermal breakthrough times since part of the flow is diverted away from reaching the production well. However, the presence of faults that enable fluid flow increases the sensitivity of the doublet positioning to the fault location. Contrary to this, a fault with a sealing behaviour renders the system lifetime less sensitive to the doublet positioning.

Results suggest that operators would always opt for higher flow rates, since the generated NPV using 400 m<sup>3</sup>/h is at all times higher than any scenario considered with a lower flow rate of 100 m<sup>3</sup>/h. NPV's of low flow rates are more sensitive to other parameters in absolute terms, while higher flow rates only appear sensitive to system lifetime. For both flow rates the NPV demonstrate an asymptotic behaviour implying that further extension of system lifetime does not yield additional benefits. This finding

implies the presence of an optimum in terms of the balance between system lifetime and generated value.

Reservoir architectures with a low flowing layer in the middle, or two individual reservoirs separated by an impermeable layer showcase improved system lifetime and NPV generation. The presence of a less permeable layer in the middle acts as a heating body, leading to improved extraction from the production layers as well as from over- and underburden bodies. This result is present for both high and low flow rates although it is more pronounced for the former.

### 3.8 Results: Two doublets separated by a fault (2D1F)

#### 3.8.1 Fault permeability impact

The flow properties of the fault have a major impact in the shape of the cold front. A sealing fault causes a clear distortion to the shape of the cold front (Figure 14). This distortion can be better observed in the respective cross sections of Figure 14. The absence of a flow path along the fault channels the flow of cold water from the injector along the fault plane. As a result, at the producer well the cold front arrives first from the side of the fault. Contrary to this, the outer side of the producer, away from the fault, maintains a higher temperature for a longer period of time. These results are consistent for both doublets, as the fault throw and respective depth of each block do not cause noticeable differences.

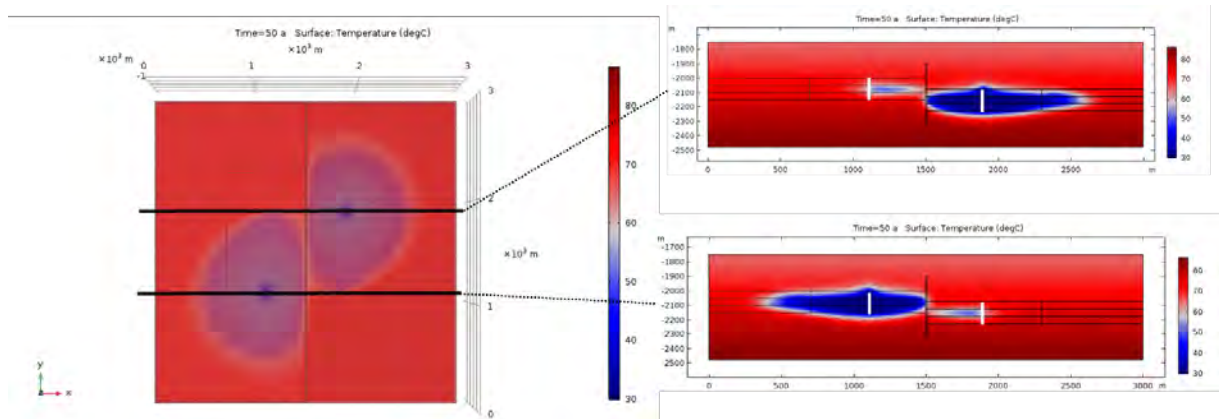


Figure 14. Top view and respective sections through the west producer and east injector (North section) and the west injector and east producer (South section). The fault permeability is sealing, the throw of 75 m, the injection flow rate is  $250 \text{ m}^3/\text{h}$ , the reservoir architecture is min/max/mid, while a checkerboard configuration is used for the well arrangement.

A conduit flow provides a channelized path for the cold water to propagate into. This leads to flow along the fault that escapes out of the influence area of the doublets (Figure 15). At the same time the cold water flow also travels across the fault, preferentially using the highest flowing layer (in the case shown in Figure 15 the middle one). As a result, both injectors contribute cold water flow to both producers. The resulting cold water front shape after 50 years of production shows a characteristic tear shape point towards both producers.

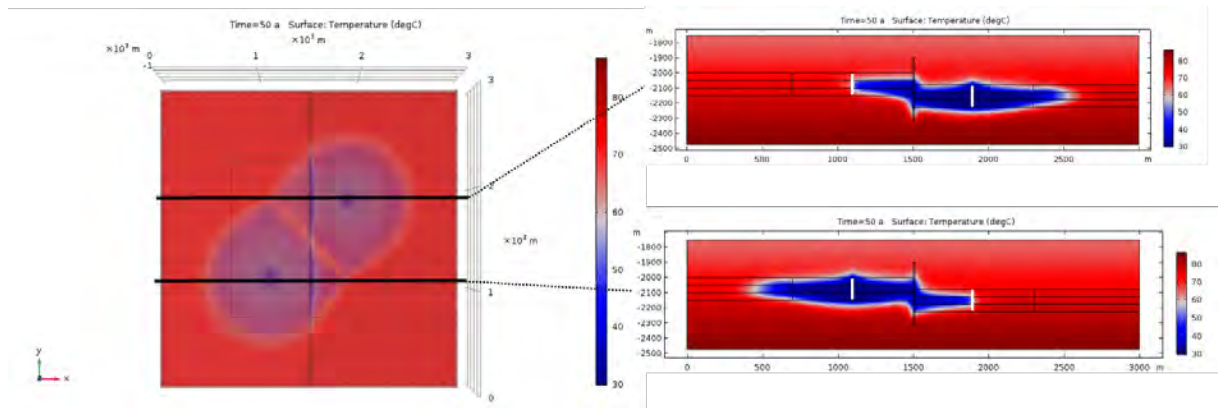


Figure 15. Top view and respective sections through the west producer and east injector (North section) and the west injector and east producer (South section). The fault permeability is conduit, the throw of 75 m, the injection flow rate is  $250 \text{ m}^3/\text{h}$ , the reservoir architecture is min/max/mid, while a checkerboard configuration is used for the well arrangement.

### 3.8.2 Single developer – two individual developers

Comparing having a single developer operating both doublets and two individual developers operating one doublet shows some benefits for the former. Firstly, the production temperature can remain higher for a longer period of time, effectively extending the lifetime of the system (Figure 16). Consequently, the robustness of the development increases as possible implications about the presence the flow behavior of faults are alleviated. This observation is valid for both high and low flow rates. Nonetheless, higher flow rates achieve similar levels of cumulative produced energy at much shorter system lifetimes; e.g. a single developer would achieve 4 million MWh at circa 53 years of system lifetime with a low flowrate of  $100 \text{ m}^3/\text{h}$  while the same amount of cumulative energy can be generated in less than half the time (circa 22 years) with a higher flowrate of  $250 \text{ m}^3/\text{h}$ . Nonetheless, the benefit of a single developer in terms of overall produced energy increases with longer lifetimes for both flow rates.

For two individual developers, the east doublet always exhibits a higher amount of cumulative energy produced; this is attributed to the fault offset that positions the east doublet deeper and therefore producing with slightly higher temperature, based on the geothermal gradient.

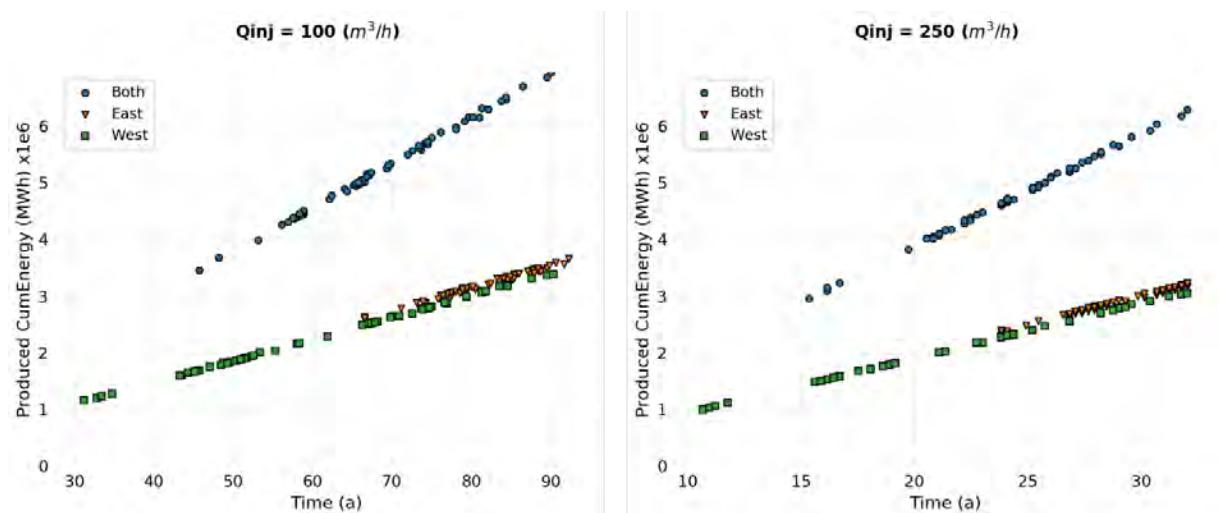


Figure 16. Cumulative produced energy at the time of breakthrough for the whole dataset of 128 simulations.

The percentage of recovered HIP compared to the initial HIP shows no difference between a single developer or two individual ones (Figure 17). This result is valid regardless of the flow rate used. Similarly, to the cumulative produced energy using a higher flow rate achieves comparable heat recovery at shorter lifetimes. However, low flow rates do result in higher minimum and maximum

values of recovered HIP. This can be attributed to longer lifetimes enabling an increased contribution of heat recharge via conduction from the layers confining the reservoir.

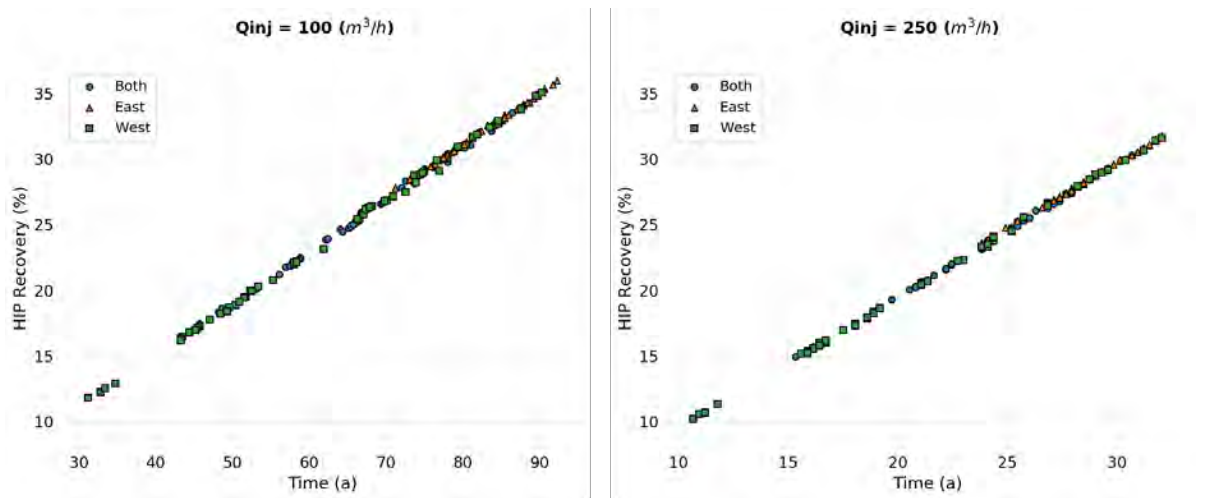


Figure 17. Recovered HIP (%) at the time of breakthrough for the whole dataset of 128 simulations.

The NPV generated shows that for lower flow rates the benefit of a single developer compared to two individual ones is comparable larger than for higher flow rates (Figure 18). With a flow rate of 100 m<sup>3</sup>/h the combined development results in an aggregated result that is larger than the sum of the two parts. This difference increases further with longer lifetimes. For the high flow rate of 250 m<sup>3</sup>/h the combined development benefits more from a longer system lifetime. Nonetheless, a higher flow rate yields potentially higher NPV's with the exception of very short system lifetimes.

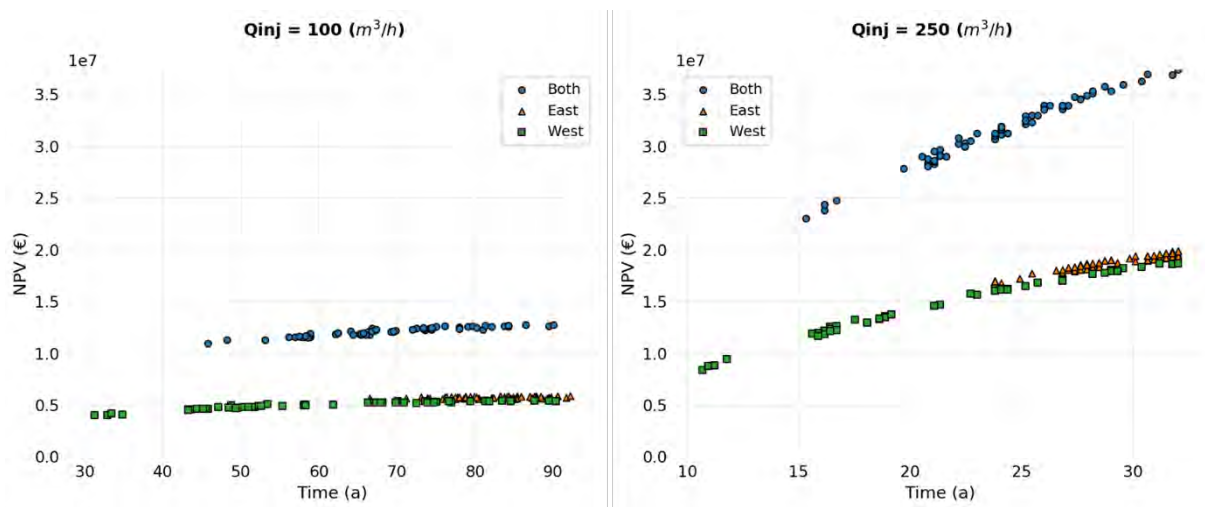


Figure 18. NPV at the time of breakthrough for the whole dataset of 128 simulations.

### 3.8.3 Result sensitivity

The result sensitivity shown considers both doublets operated by a single developer. The system lifetime is most sensitive to the flow rate used, with high flow rates resulting in shorter system lifetime (Figure 19). Slightly improved lifetime is achieved for the checkerboard configuration although in some cases a tramline configuration may lead to slightly longer lifetime. A conduit fault showcases a wider distribution of system lifetimes than a sealing one and can potentially lead to both shorter and longer lifetimes compared to the latter. The fault throw however shows minor changes in lifetimes. Reservoir architecture favors having the most permeable layer at the bottom of the reservoir, yielding a slightly shifted upwards distribution, compared to having the most permeable layer at the middle of

the reservoir. Lastly, fault distance exhibits a very similar distribution for all values that is gradually shifted upwards when the fault is progressively further away from the west doublet.

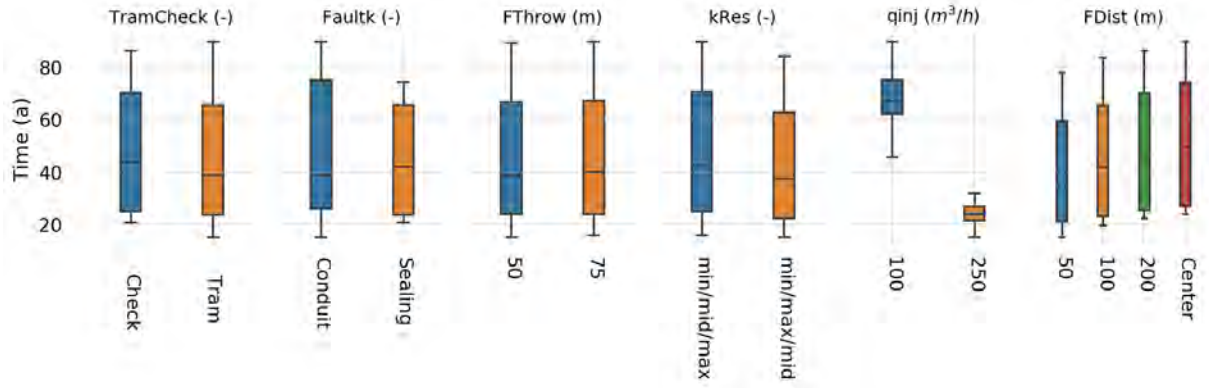


Figure 19. Sensitivity of the thermal breakthrough time to the input parameters

The generated cumulative energy and HIP recovery show almost identical sensitivities to the input parameters (Figures 20 and 21). The checkerboard well configuration demonstrates a narrower distribution with higher values for both cumulative energy and HIP recovery compared to the tram configuration. A sealing fault behavior showcases also a narrower distribution meaning that its impact is quite dominant on the outcome; at the same time the wider distribution of a conduit fault allows for both lower and higher amounts of generated energy and heat recovery with the median being significantly higher compared to a sealing fault. Contrary, the fault throw has a minor effect, with a higher throw resulting in a slight increase of the median values for both produced and recovered energy. Similar to the system lifetime a reservoir architecture with the highest flowing layer at the bottom benefits energy production and recovery, but compared to lifetime this positive difference is more pronounced. Both flow rates show similar distribution values with higher flowrates resulting to notable lower energy production and recovery. Finally, the fault distance affects energy production and recovery in a similar way to its effect on system lifetime exhibiting higher values when moving further away from west doublet. However, in this case the distributions are narrower and the differences between each fault position more substantial.

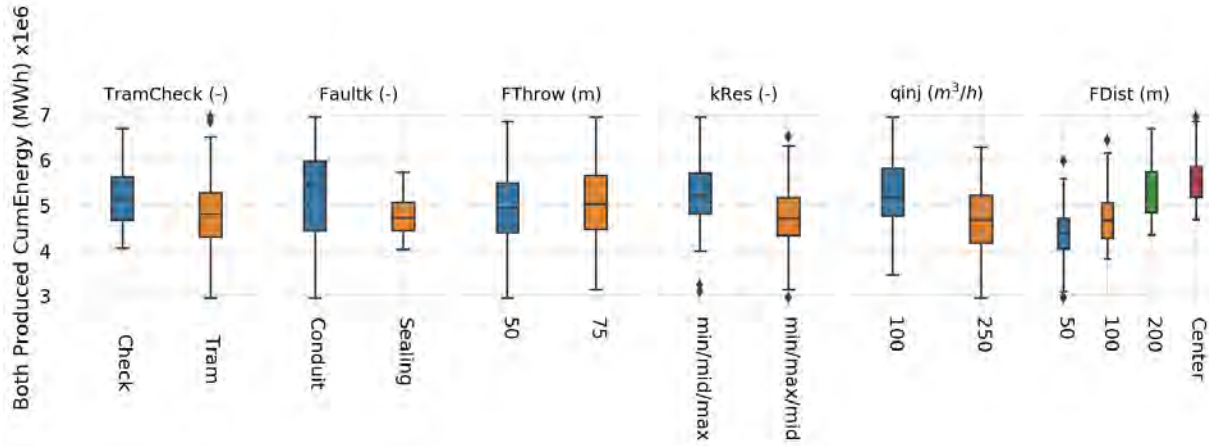


Figure 20 Sensitivity of the produced cumulative energy (MWh) to the input parameters

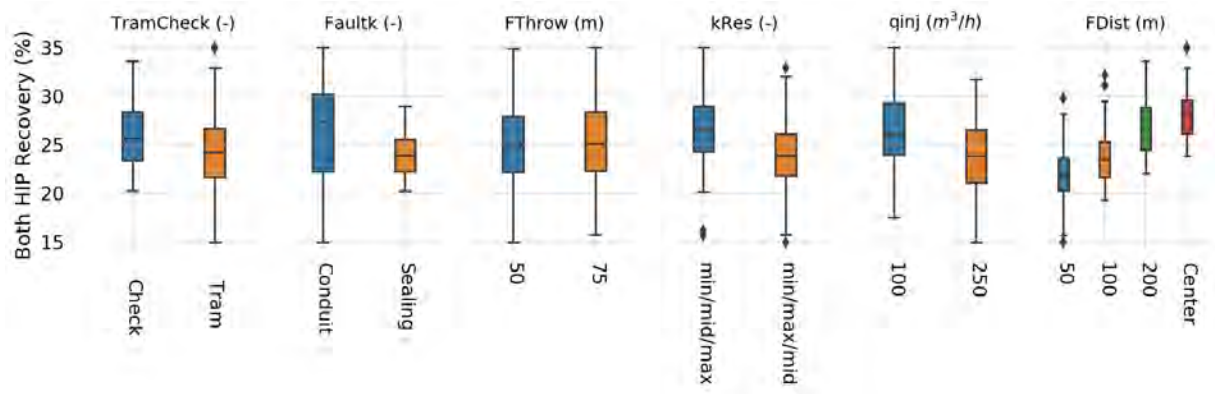


Figure 21 Sensitivity of the HIP recovery (%) to the input parameters

The NPV appears more sensitive to the flow rates that almost fully dominate the economic output of the system. The checkerboard configuration is marginally preferable compared to the tram configuration. A sealing fault leads to a slightly more confined distribution while a conduit one enables higher and lower NPV values at the extremes. The fault throw seems to have no impact. The reservoir architecture shows a slightly better NPV output when the maximum flowing layers is at the bottom of the reservoir. Lastly moving closer to the fault results in a more decisive and more negative impact to the generated NPV.

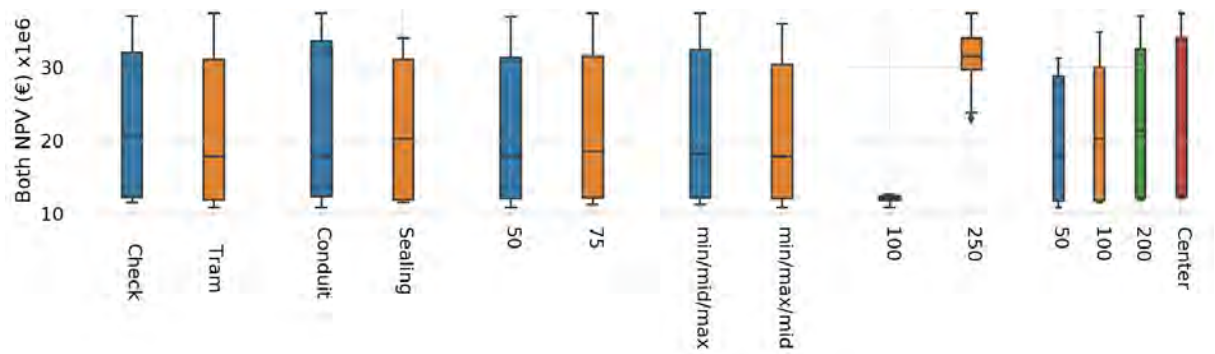


Figure 22. Sensitivity of the NPV to the input parameters

### 3.8.4 2D1F Summary

The analysis identifies flowrate, fault flow behavior and fault proximity to the west doublet as then main factors affecting both system lifetime, as well as energy production and recovery and NPV. The fault permeability combined with the doublet positioning with regards to the fault suggests that it is crucial to characterize the presence and flow properties of the fault for generating robust development plans. The impact of the fault throw however is found to be negligible.

For the NPV output the flow rate remains the most crucial parameter, followed by fault behavior and distance albeit with much less impact than flow rate. Importantly, for system lifetime the effect of the flow rate is dominant with other parameters exhibiting a smaller influence. Energy production and recovery exhibit a very similar sensitivity pattern between them but quite different than the one for system lifetime. Particularly, while the same parameters are more dominant, the impact of flow rate is not as pronounced and fault permeability, well configuration, reservoir architecture emerge as important factors.

# 4 Field application

## 4.1 Realistic 3D model

The insights generated from the model completion stage are included in the field application stage. The models presented here are based on the geological model described in the Panterra report (Hopman, 2016) that was confidentially provided to TU Delft. A summary of the porosity and permeability distribution of the respective model layers is showcased in Figure 23. An overview of the reservoir model used is shown in Figure 24.

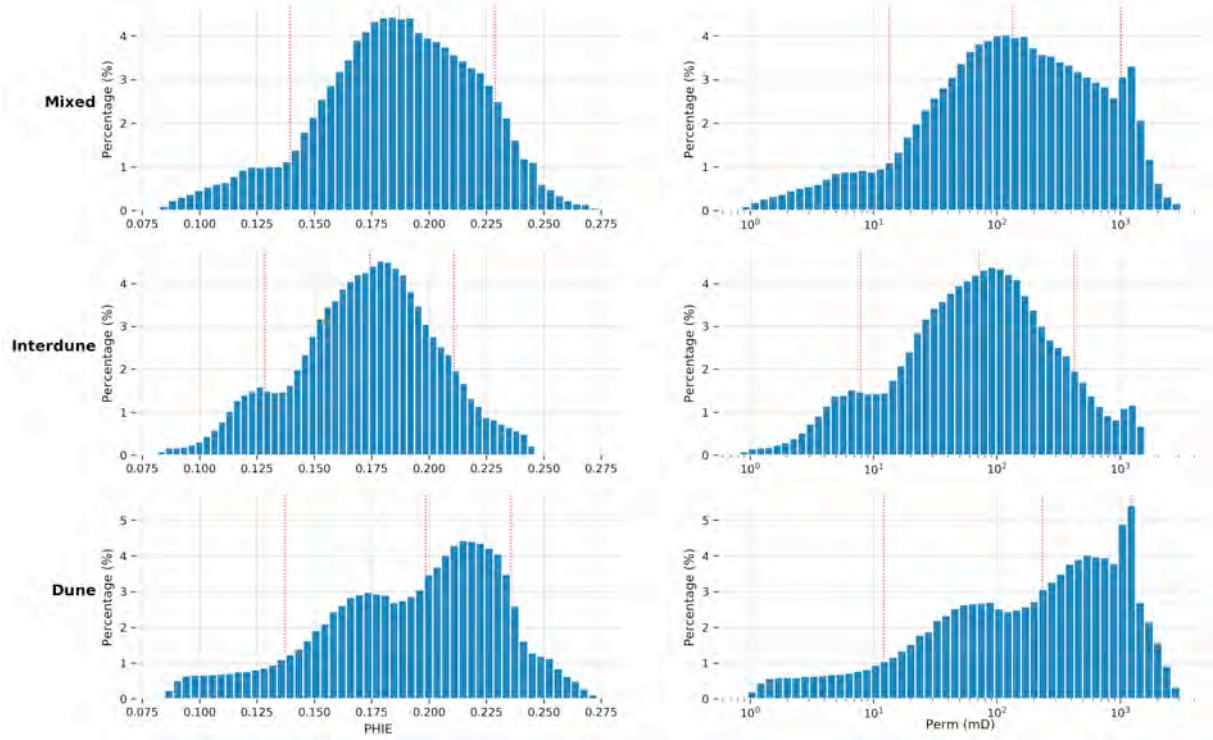


Figure 23. Porosity and permeability distributions from the Petrel model used in the full scale simulations. The red dashed lines represent P90, P50 and P10 values respectively.

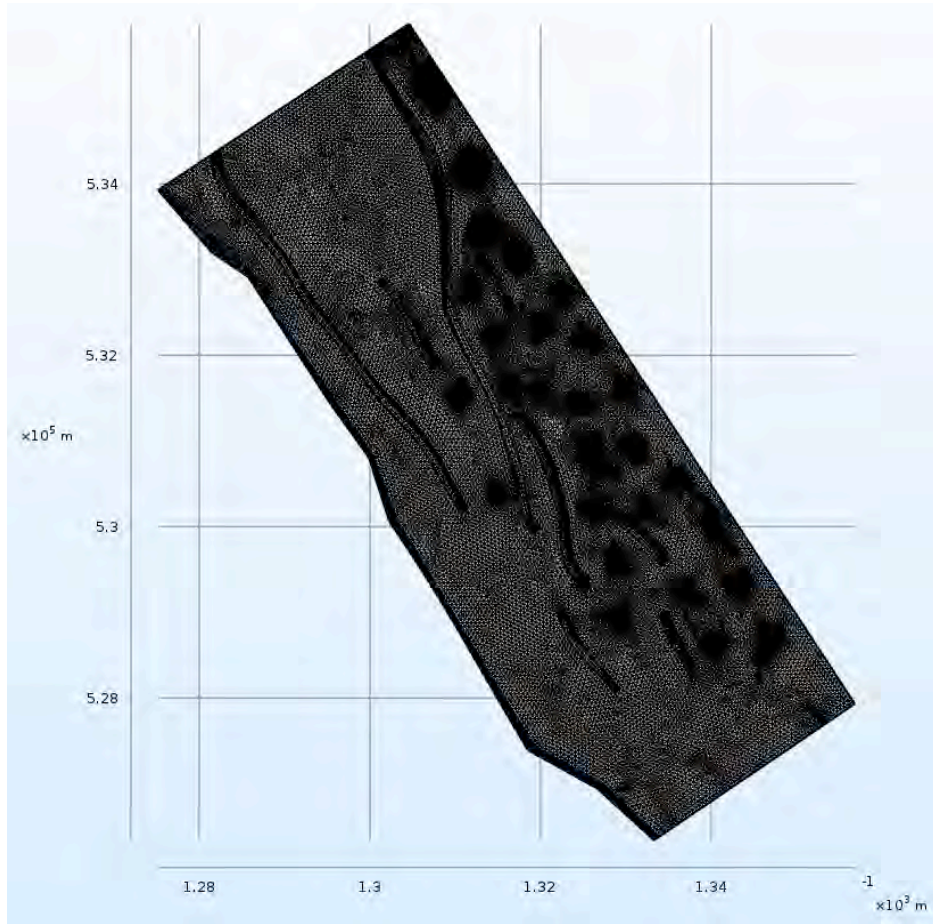


Figure 24. Overview of the meshed full scale reservoir model. Depending the scenario considered the total number of cells ranges between 1.9 and 3.9 million cells.

## 4.2 Considered scenarios

Four separate scenarios are considered for the full scale model. All scenarios use the 3D model provided by Panterra and implemented in the simulator as described in section 4.1. Their differences are tabulated in Table 5. The well arrangement for each scenario is depicted in Figures 25, 26 and 27. Scenarios S0, S1, and S2 are simulated with conductive faults. For S2 two simulations with conductive and sealing faults are conducted.

Table 5. Overview table of the considered scenarios

Scenario	Number of doublets	Well spacing (m)	Qinj (m <sup>3</sup> /h)	Tinj (degC)
S0	3		200	35
S1	3 + 14	~1000	200	35
S2	3 + 11	~1200	200	35
S3	3 + 6	~1600	200	35

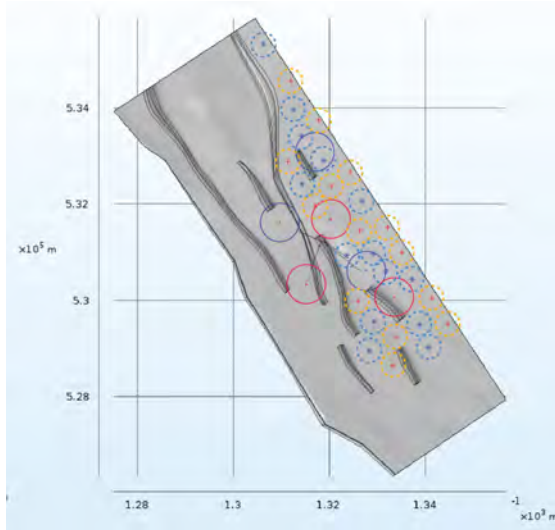


Figure 25. Scenario S1 well position and functions. Solid lines mark the S0 wells and dashed lines mark the additional wells in this scenario

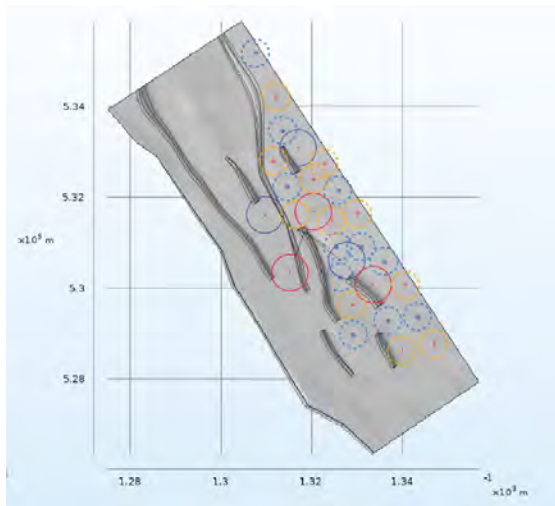


Figure 26. Scenario S2 well positions. Solid lines mark the S0 wells and dashed lines mark the additional wells in this scenario

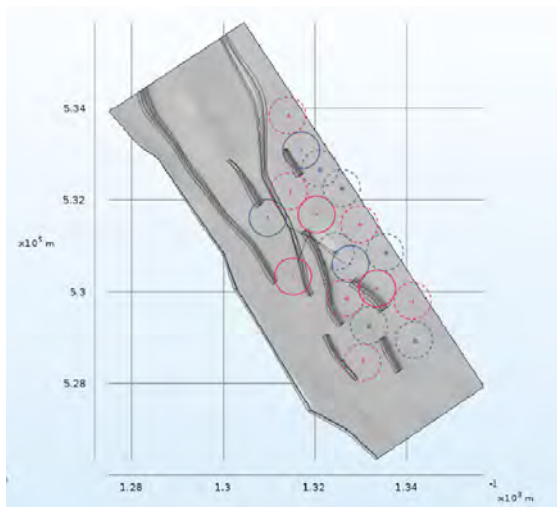


Figure 27. Scenario S3 well positions. Solid lines mark the S0 wells and dashed lines mark the additional wells in this scenario

### 4.3 Results

The mean production temperature of the considered scenarios suggests that increasing the number of well in the system can affect the overall system lifetime (Figure 28). Nonetheless, the temperature drop of scenario S3 only starts to differentiate between noticeable after about 20 years, while scenario S2 drops below 90 °C after about 27 years. Lastly, scenario S1 already drops below 90 degrees earlier than 20 years. Note that the average produced temperature for all the scenarios are above 85 °C after 25 years of production.

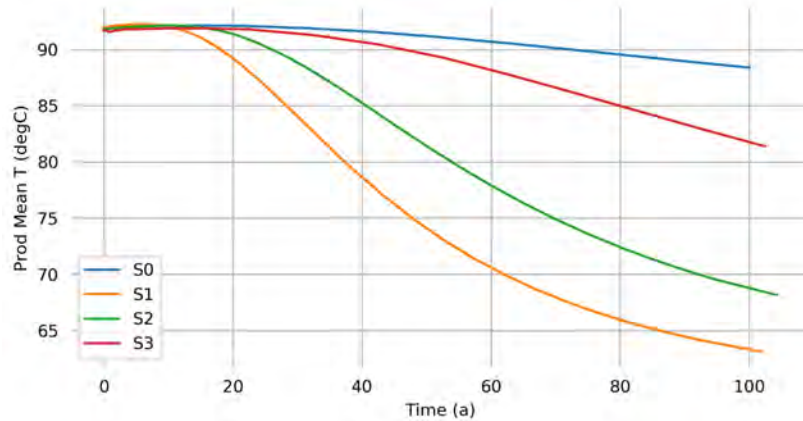


Figure 28 Average production temperature per scenario considered

The scenario power curves show that a larger number of wells results in an increased power with scenarios S0, S1, S2, and S3 delivering circa 37.5 MW, 215 MW, 175 MW and 112.5 MW respectively at the first years (Figure 29). Keeping the mean production temperatures in mind, it is clear that in terms of power scenario S0 shows no effective power drop in 100 years, while S3 only starts to decline after about 45 years. Scenarios S1 and S2 start to decline earliest at circa 12 and 18 years respectively. Nonetheless, the sharper power drop for scenario S1 is offset by the larger number of wells and therefore its power does not fall below that of scenario S2.

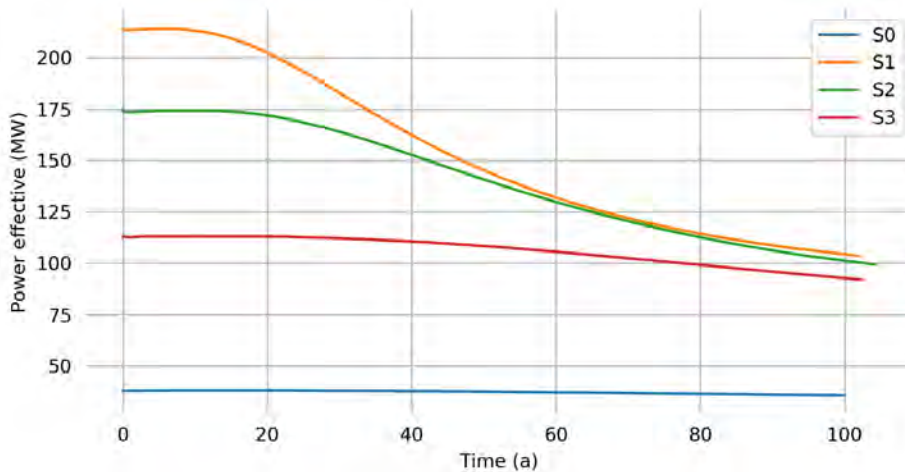


Figure 29. Effective power per considered scenario

The individual well production temperatures for scenario S1 reveal that a few wells exhibit early thermal breakthrough and only two maintain temperatures above 85 °C for longer than 45 years (Figure 30).

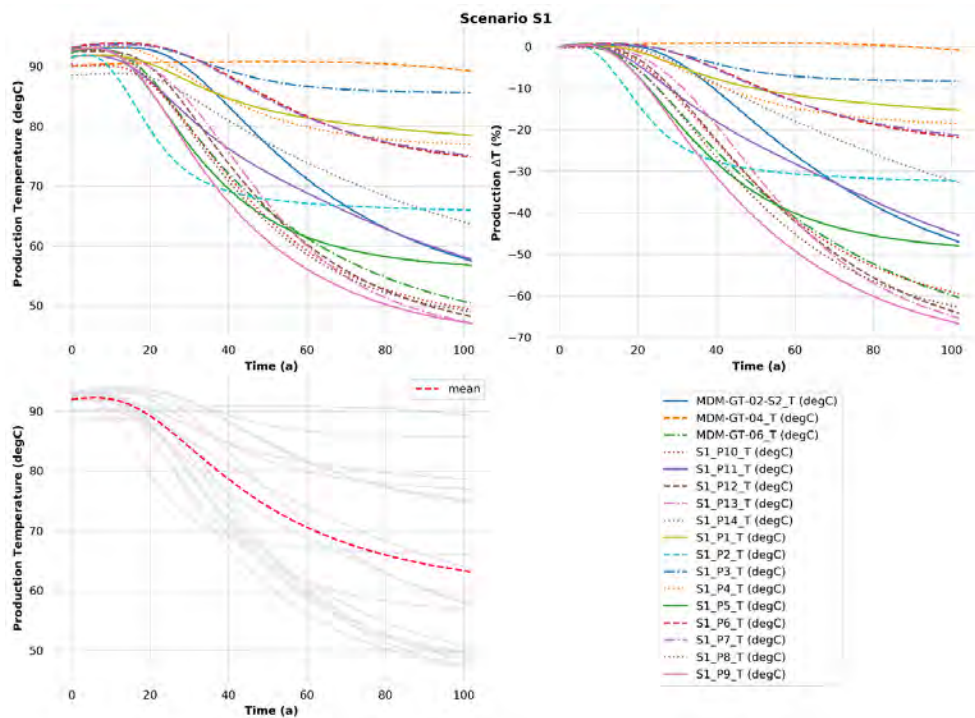


Figure 30. Scenario S1 production temperature, production  $\Delta T$  (%) and mean production temperature.

The individual well production temperatures for scenario S2 with sealing faults reveal that about half of the wells exhibit thermal breakthrough after around 20 years (Figure 31). The other half show significantly less temperature drop over time, maintaining production temperatures above 80 °C until 100 years. The mean production temperature fall below 80 °C just before 45 years of production. In the event of conduit faults the production temperature of the wells is slightly higher for longer period of time with the mean production temperature falling below 80 °C just after 45 years. In this scenario only a single well remains producing at very low temperatures.

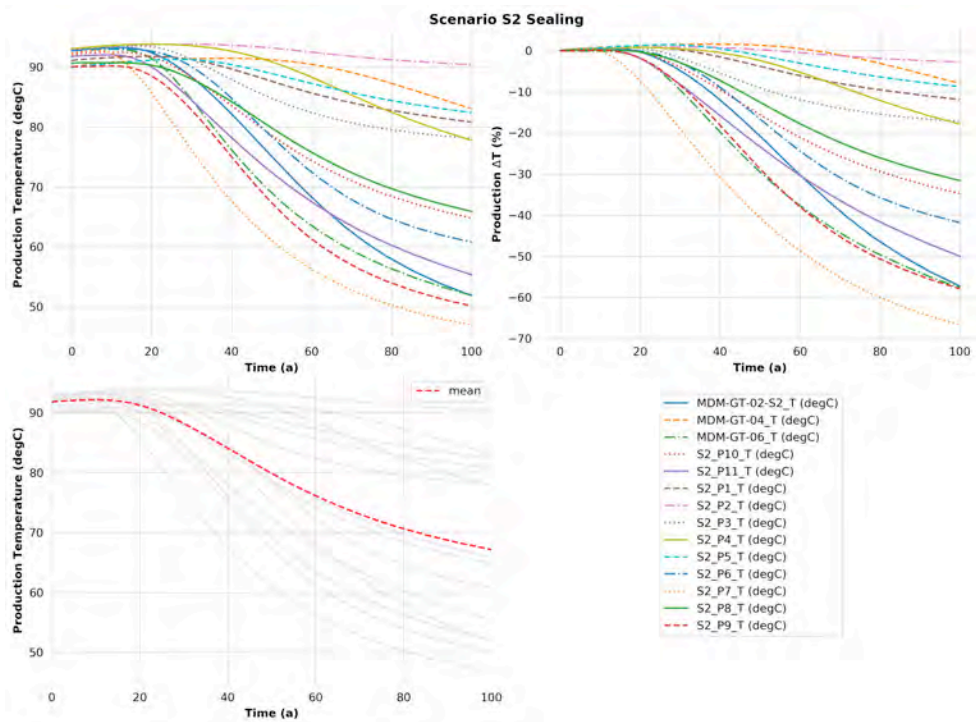


Figure 31. Scenario S2 with sealing faults production temperature, production  $\Delta T$  (%) and mean production temperature.

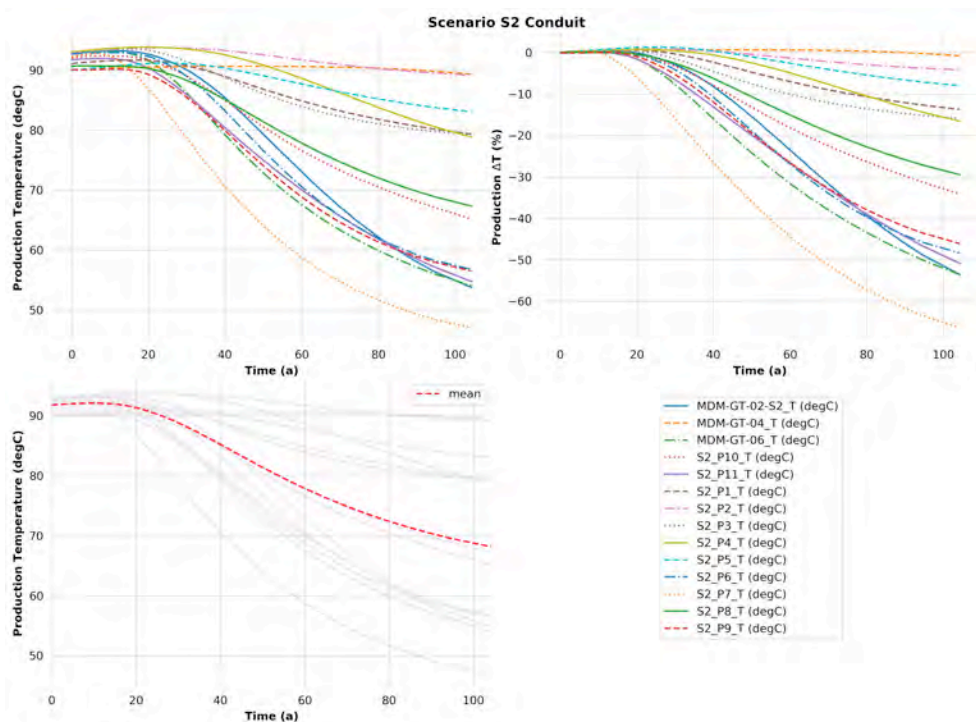


Figure 32. Scenario S2 with conduit faults production temperature, production  $\Delta T$  (%) and mean production temperature.

Scenario S3 exhibits a much longer lifetime with the mean production temperature not dropping below 80 °C within the 100 years of simulation. In this scenario three wells show an early production temperature drop, but this only happens after 20 years of production.

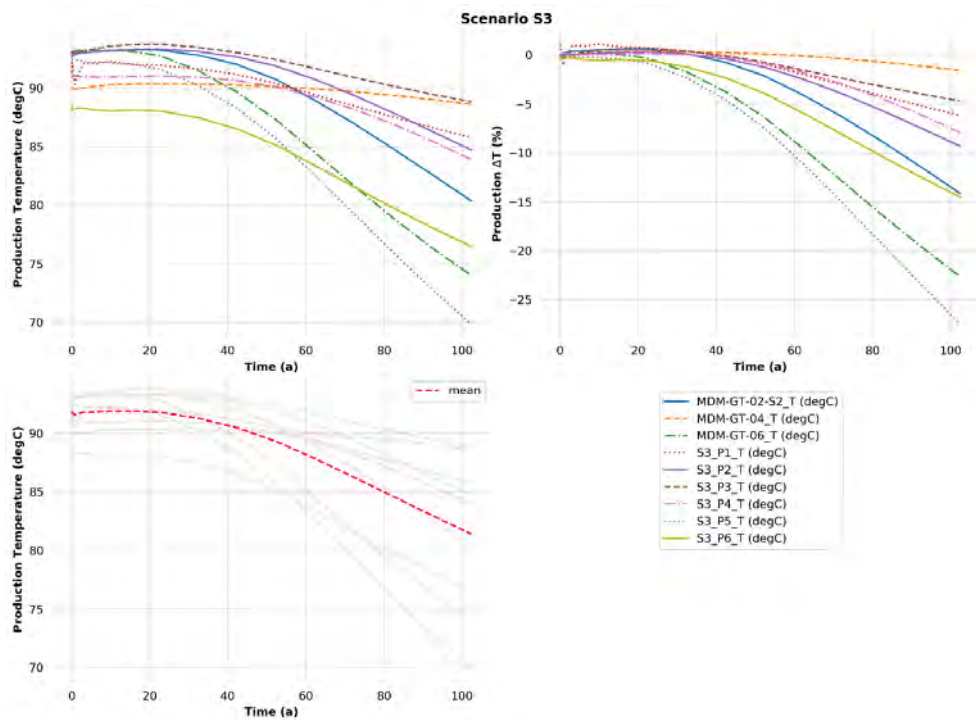


Figure 33. Scenario S3 production temperature, production  $\Delta T$  (%) and mean production temperature.

As the reservoir temperature for S1 at the different zone interfaces shows (Figure 34) pockets of high temperature remain. For all considered scenarios, an optimization routine on the well positioning would further improve the overall field performance and maintain higher power output over longer periods of time.

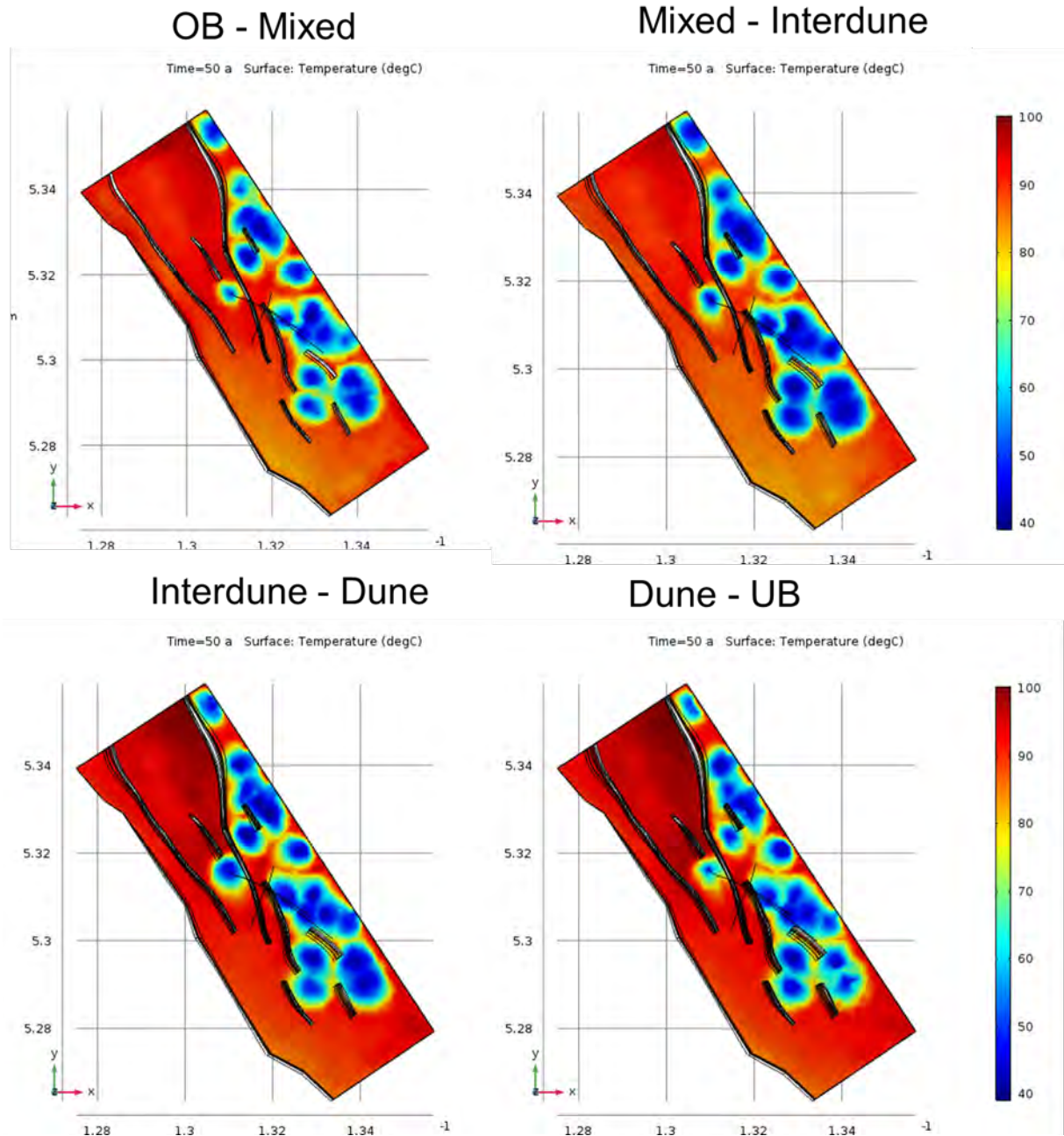


Figure 34. Temperature at the contact of the different reservoir zones for Scenario S1 after 50 years of production from shallow (top left) to deep (bottom right).

#### 4.4 Monitoring

Using 2600 computationally intensive numerical simulations of two doublets placed in a checkboard pattern, we studied if it is possible to find a relation between the extent of the cold plume and the production temperature (Babaei & Nick, 2019). To this end, we defined two licence sizes of  $L'$  and  $L''$  which are the size of a region with the average temperature drop of  $1\text{ }^{\circ}\text{C}$  at the lifetime and the farthest boundary away from the wells where the difference between the minimum temperature of that boundary and the initial temperature of that boundary is  $1\text{ }^{\circ}\text{C}$ , respectively. The required outline square to fully contain the  $1\text{ }^{\circ}\text{C}$  temperature drop for different injection rates ( $Q$ ) and well spacing ( $L$ ), with the spacing between doublets ( $dx$ ) being always equal to  $L$  is shown in Figure 35. It is shown that based on the heterogeneity of the aquifer different sizes of the licence region are required. The production temperature and the numerical modelling considering a realistic porosity and permeability heterogeneity can be instrumental for defining the size of the licence region.

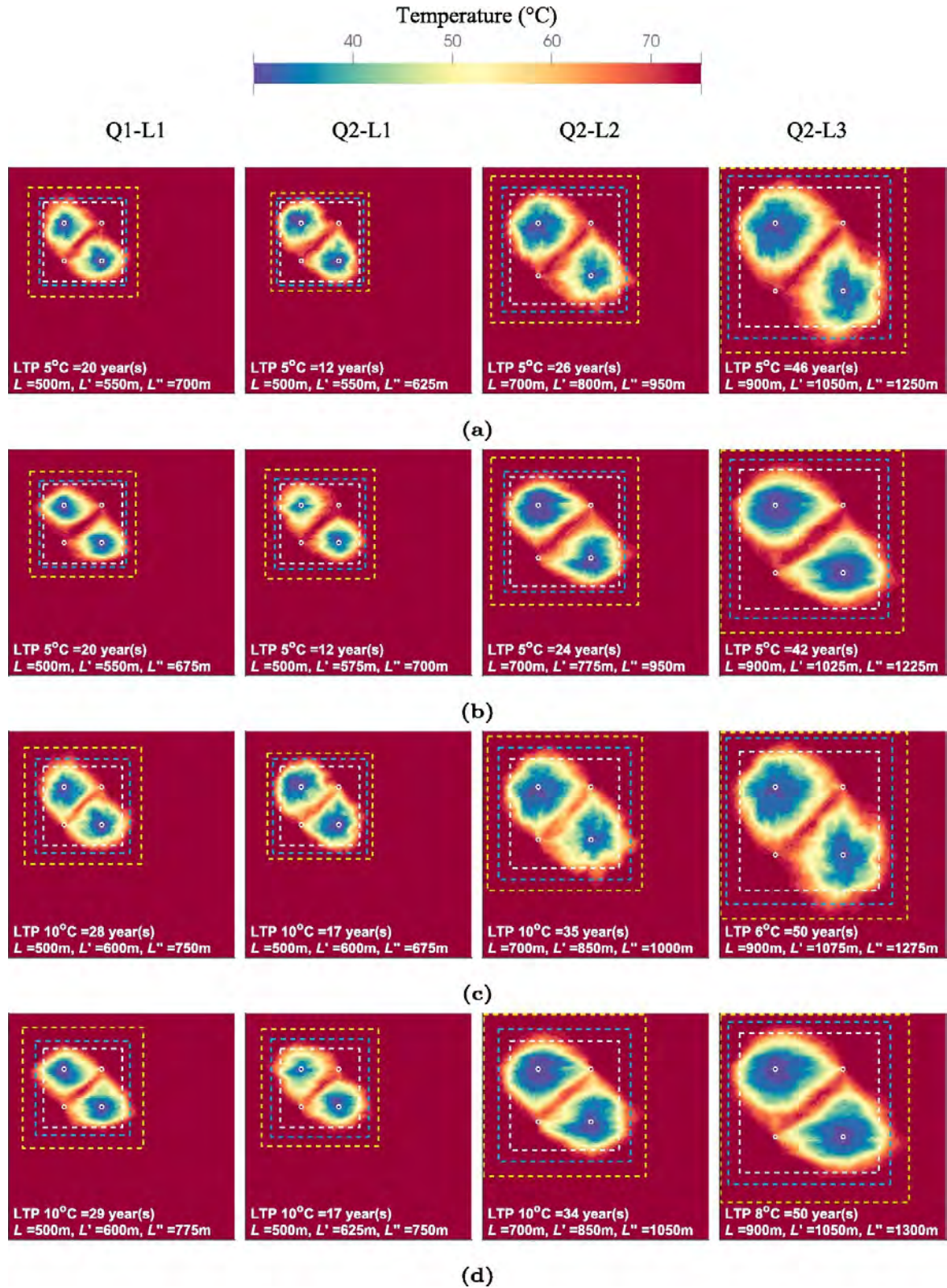


Figure 35. Positions of  $L'$  and  $L''$  for selected examples with different heterogeneity types for the converged solution and for (a) C1, LTP5, (b) C2, LTP5, (c) C1, LTP $_n$  and (d) C2, LTP $_n$ , where  $n$  is 10 °C if within 50 years experiences 10 °C drop, otherwise  $n$  is the temperature drop of  $T_P^t$  at the end of simulation (50 years). From left column to right column in all rows: Q1 = 150 m<sup>3</sup>/h and  $L = dx = 500$  m, Q2 = 250 m<sup>3</sup>/h and  $L = dx = 500$  m, Q2 = 250 m<sup>3</sup>/h and  $L = dx = 700$  m, and Q2 = 250 m<sup>3</sup>/h and  $L = dx = 900$  m. In all subfigures, white, cyan and yellow dashed lines represent the  $2L \times 2dx$  extent,  $L'$  extent and extent,  $L''$  respectively. Note that LTP $_n$  of the geothermal system is defined as the time (in years) when the average production temperature has dropped  $n$  °C with respect to the initial condition. Figure source: (Babaei & Nick, 2019)

## 5 Conclusions

The key findings of this study are as follows:

Heat recovery efficiency of up to 30% can be reached, but this requires denser doublet deployment with smaller injector-producer spacing than the currently implemented in WNB.

Higher doublet density than the current density in the WNB could still result in sufficient doublet life time but will result in higher interference. Tailor-made legislation is therefore required to facilitate exploitation of a single resource by multiple operators.

The characterization of fault flow properties is more significant compared to the fault offset. Additionally, system lifetime is less affected by the presence and flow behaviour of faults when a smaller well spacing is utilized. The fault flow properties have a significant impact to the shape and extent of the cold plume and therefore the system lifetime. In absolute numbers, faults that enable fluid flow lead to longer thermal breakthrough times since part of the flow is diverted away from reaching the production well. However, the presence of faults that enable fluid flow increases the sensitivity of the doublet positioning to the fault location. Contrary to this, a fault with a sealing behaviour renders the system lifetime less sensitive to the doublet positioning.

Results suggest that operators would always opt for higher flow rates, since the generated NPV using 400 m<sup>3</sup>/h is at all times higher than any scenario considered with a lower flow rate of 100 m<sup>3</sup>/h. Moreover, increasing the flow rate four times results in an NPV increase of a factor seven. NPV's of low flow rates are more sensitive to other parameters in absolute terms, while higher flow rates only appear sensitive to system lifetime. For both flow rates the NPV demonstrate an asymptotic behaviour implying that further extension of system lifetime does not yield additional benefits. This finding implies the presence of an optimum in terms of the balance between system lifetime and generated value.

Reservoir architectures with a low flowing layer in the middle, or two individual reservoirs separated by an impermeable layer showcase improved system lifetime and NPV generation. The presence of a less permeable layer in the middle acts as a heating body, leading to improved extraction from the production layers as well as from over- and under- burden bodies. This result is present for both high and low flow rates although it is more pronounced for the former. Note that, clearly having no low permeability layer at all in the reservoir can even improve NPV more as water is more evenly distributed.

Results from the synthetic models shown can serve as guidelines to reducing the considered options in full scale field models. The importance and relevance of these results remains very high for layered reservoirs with good horizontal homogeneity.

Increase in operational flow rate can increase Energy Sweep while decrease Coefficient of Performance,

Sufficient lifetime (>20 years) could be achieved for the well spacing of less than 900 m for a discharge of 250 m<sup>3</sup>/hr in heterogeneous reservoirs. The lifetime can be increased significantly or the well spacing can be further reduced if larger temperature drop (>1°C) at the producers are permitted. This would however require a larger license area than the  $2dx \times 2L$  in order to minimise the negative interference with the neighbouring geothermal projects.

The production temperature and the numerical modelling considering the porosity and permeability heterogeneity can be used for defining the size of the licence region and minimising the interference.

## 6 References

- Babaei M., Nick H.M., (2019). Performance of low-enthalpy geothermal systems: Interplay of spatially correlated heterogeneity and well-doublet spacings. *Applied Energy*, 253. <https://doi.org/10.1016/j.apenergy.2019.113569>
- Barbier, E. (2002). Geothermal energy technology and current status: an overview. *Renewable & Sustainable Energy Reviews*, 6(1–2), 3–65. [https://doi.org/10.1016/S1364-0321\(02\)00002-3](https://doi.org/10.1016/S1364-0321(02)00002-3)
- Blöcher, M. G., Zimmermann, G., Moeck, I., Brandt, W., Hassanzadegan, A., & Magri, F. (2010). 3D numerical modeling of hydrothermal processes during the lifetime of a deep geothermal reservoir. *Geofluids*, 10(3), 406–421. <https://doi.org/10.1111/j.1468-8123.2010.00284.x>
- Bonté, D., Wees, J. D. Van, & Verweij, J. M. (2012). Subsurface temperature of the onshore Netherlands: new temperature dataset and modelling. *Netherlands Journal of Geosciences-Geologie En Mijnbouw*, 91(4), 491–515.
- Crooijmans, R. A., Willems, C. J. L., Nick, H. M., & Bruhn, D. F. (2016). The influence of facies heterogeneity on the doublet performance in low-enthalpy geothermal sedimentary reservoirs. *Geothermics*, 64, 209–219. <https://doi.org/10.1016/j.geothermics.2016.06.004>
- Daniilidis, A., Nick H.M., Bruhn D. (2020). Interdependencies between physical, design and operational parameters for direct use geothermal heat in faulted hydrothermal reservoirs. under review.
- Daniilidis, A., Alpsoy, B., & Herber, R. (2017). Impact of technical and economic uncertainties on the economic performance of a deep geothermal heat system. *Renewable Energy*, 114, 805–816. <https://doi.org/10.1016/j.renene.2017.07.090>
- Daniilidis, A., Doddema, L., & Herber, R. (2016). Risk assessment of the Groningen geothermal potential: From seismic to reservoir uncertainty using a discrete parameter analysis. *Geothermics*, 64, 271–288. <https://doi.org/http://dx.doi.org/10.1016/j.geothermics.2016.06.014>
- Daniilidis, A., & Herber, R. (2016). Salt intrusions providing a new geothermal exploration target for higher energy recovery at shallower depths. <https://doi.org/10.1016/j.energy.2016.10.094>
- Garg, S. K., & Combs, J. (2015). A reformulation of USGS volumetric “heat in place” resource estimation method. *Geothermics*, 55, 150–158. <https://doi.org/10.1016/J.GEOTHERMICS.2015.02.004>
- Hopman, T. (2016). *Middenmeer Reservoir Model I - Project G1234*.
- Jalali, M., Embry, J.-M., Sanfilippo, F., Santarelli, F. J., & Dusseault, M. B. (2016). Cross-flow analysis of injection wells in a multilayered reservoir. *Petroleum*, 2(3), 273–281. <https://doi.org/10.1016/J.PETLM.2016.05.005>
- Limberger, J., Boxem, T., Pluymaekers, M., Bruhn, D., Manzella, A., Calcagno, P., ... van Wees, J.-D. (2018). Geothermal energy in deep aquifers: A global assessment of the resource base for direct heat utilization. *Renewable and Sustainable Energy Reviews*, 82, Part 1, 961–975. <https://doi.org/https://doi.org/10.1016/j.rser.2017.09.084>
- Moeck, I. S. (2014). Catalog of geothermal play types based on geologic controls. *Renewable and Sustainable Energy Reviews*, 37, 867–882. <https://doi.org/http://dx.doi.org/10.1016/j.rser.2014.05.032>
- Pluymaekers, M. P. D., Kramers, L., Wees, J. D. Van, Kronimus, A., Nelskamp, S., Boxem, T., & Bonté, D. (2012). Reservoir characterisation of aquifers for direct heat production: Methodology and screening of the potential reservoirs for the Netherlands. *Netherlands Journal of Geosciences-Geologie En Mijnbouw*, 91(4), 621–636.
- Saeid, S., Al-Khoury, R., Nick, H. M., & Barends, F. (2014). Experimental–numerical study of heat

flow in deep low-enthalpy geothermal conditions. *Renewable energy*, 62, 716-730.

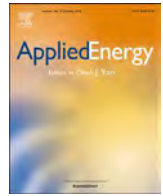
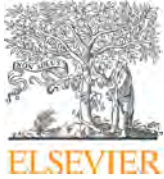
- Salimzadeh, S., & Nick, H. M. (2019). A coupled model for reactive flow through deformable fractures in Enhanced Geothermal Systems. *Geothermics*, 81, 88–100. <https://doi.org/10.1016/J.GEOTHERMICS.2019.04.010>
- Salimzadeh, S., Nick, H. M., & Zimmerman, R. W. (2018). Thermoporoeleastic effects during heat extraction from low-permeability reservoirs. *Energy*. <https://doi.org/10.1016/j.energy.2017.10.059>
- Vik, H., Salimzadeh, S., & Nick, H. M. (2018). Heat recovery from multiple-fracture enhanced geothermal systems: The effect of thermoelastic fracture interactions. *Renewable Energy*, 121, 606–622. <https://doi.org/10.1016/J.RENENE.2018.01.039>
- TNO. (2018). ThermoGIS v2.0 - Economic model. Retrieved July 2, 2019, from <https://www.thermogis.nl/en/economic-model>
- Willems, C. J.L., & M. Nick, H. (2019). Towards optimisation of geothermal heat recovery: An example from the West Netherlands Basin. *Applied Energy*, 247(April), 582–593. <https://doi.org/10.1016/j.apenergy.2019.04.083>
- Willems, C.J.L., Nick, H. M., Weltje, G. J., & Bruhn, D. F. (2017a). An evaluation of interferences in heat production from low enthalpy geothermal doublets systems. *Energy*, 135, 500–512. <https://doi.org/10.1016/j.energy.2017.06.129>
- Willems, C. J.L., Nick, H. M., Goense, T., & Bruhn, D. F. (2017b). The impact of reduction of doublet well spacing on the Net Present Value and the life time of fluvial Hot Sedimentary Aquifer doublets. *Geothermics*, 68, 54–66. <https://doi.org/10.1016/j.geothermics.2017.02.008>

## 7 Acknowledgements

The authors would like to acknowledge the constructive feedback of Harmen Mijnlief (TNO), Raymond Godderij (EBN), Bertran de Lange (ECW Netwerk) and Frank Schoof (Platform Geothermie) that helped shaping this work.

## Appendices:

- Willems, C.J.L., & Nick, H.M. (2019). Towards optimisation of geothermal heat recovery: An example from the West Netherlands Basin. *Applied Energy*, 247(April), 582–593.
- Babaei M., & Nick H.M., (2019). Performance of low-enthalpy geothermal systems: Interplay of spatially correlated heterogeneity and well-doublet spacings. *Applied Energy*, 253.



# Towards optimisation of geothermal heat recovery: An example from the West Netherlands Basin

C.J.L. Willems<sup>a</sup>, H. M. Nick<sup>b,c,\*</sup>

<sup>a</sup> Systems Power and Energy Division, University of Glasgow, United Kingdom

<sup>b</sup> Department of Geoscience and Engineering, Delft University of Technology, Delft, Netherlands

<sup>c</sup> The Danish Hydrocarbon Research and Technology Centre, Technical University of Denmark, Copenhagen, Denmark

## HIGHLIGHTS

- First benchmark of on-going Hot Sedimentary Aquifer exploitation.
- Scope for heat recovery optimisation from geothermal resources.
- Application of hydrocarbon exploitation concepts in geothermal context.

## ARTICLE INFO

### Keywords:

Direct-use  
Low-enthalpy  
Reservoir engineering  
Geothermal field-development  
Low-carbon heat  
Hot Sedimentary Aquifers  
Recovery factor

## ABSTRACT

The Netherlands experienced the fastest European expansion of geothermal energy exploitation in the past decade. The first Dutch geothermal sites proved that Hot Sedimentary Aquifers exploitation can play an important role in a future low-carbon energy mix. In this study, we estimate that with the expansion rate of the past four years, geothermal heat production from Lower Cretaceous Hot Sedimentary Aquifers could cover up to 20% of the heat demand in the province of Zuid-Holland by 2050. Although this is a significant amount, we show in this study that only 1% of the potentially recoverable heat will be recovered by 2050. This is because of inefficient doublet deployment on a ‘first-come, first served’ basis with operational parameters that focus on objectives of small decentralised heat grid demands. Instead, similar to the common-practise approach in the hydrocarbon industry, a regional coordinated ‘masterplan’ approach could be used to increase heat recovery. Utilising numerical simulations for flow and heat transfer in the subsurface, we showed that the heat recovery efficiency could be increased by tens of percentages with such coordinated doublet deployment. Based on calculations of the Levelized Costs Of Heat for both deployment strategies, we also show that current financial support schemes do not favour heat recovery optimisation. This study emphasises that although Hot Sedimentary Aquifer resources have the potential to cover a significant part of our energy demand, a radical change in financial support schemes and legislation are required to unlock their true potential.

## 1. Introduction

Huge amounts of heat are stored in Hot Sedimentary Aquifers (HSA) in regions all over the world (e.g., [1–4]). These resources are especially suitable for district heating applications and could play a significant role in our future energy mix when integrated into district heating networks or industrial processes (e.g., [5,6]). With an increasing demand for low-carbon heat, ambitious targets are presented to enhance exploitation of these under-developed resources (e.g., [7–9]). It is, however, unclear if these targets are realistic because it is unknown how much heat could be recovered from aquifers. The Recovery

efficiency, i.e. the ratio of the total recovered energy and the estimated energy in the resource or recovery factor, is a key performance indicator in hydrocarbon production [10] but rarely mentioned in relation to geothermal energy [11–16]. It is mainly discussed in HSA feasibility studies as conjectures [2,17–19] or in relation to hydrocarbon and heat co-production (e.g., [20–22]). So far, it has not been an objective of geothermal exploitation strategies. The reason for this is that geothermal resources are often exploited to provide heat to local decentralised grids, instead of optimising heat recovery from the entire resource [23–25]. Geothermal resources are often exploited by multiple independent operators with potentially conflicting objectives [26,27].

\* Corresponding author.

E-mail addresses: [Cees.Willems@glasgow.ac.uk](mailto:Cees.Willems@glasgow.ac.uk) (C.J.L. Willems), [H.M.Nick@tudelft.nl](mailto:H.M.Nick@tudelft.nl) (H. M. Nick).

<https://doi.org/10.1016/j.apenergy.2019.04.083>

Received 10 December 2018; Received in revised form 12 April 2019; Accepted 15 April 2019

Available online 20 April 2019

0306-2619/© 2019 The Authors. Published by Elsevier Ltd. This is an open access article under the CC BY license (<http://creativecommons.org/licenses/by/4.0/>).

As a result, exploration licences are issued on a ‘first-come, first-served’ basis as legislators have no desire to be held responsible for future failure of the individual projects’ objectives. Alternatively, doublet deployment could be based on a regional masterplan that aims to optimise heat recovery of the entire HSA resource (e.g., [26,28]), similar to the common-practise approach in the hydrocarbon industry [29–31].

This study compares the impact of those two contrasting approaches in doublet deployment on the recoverable heat from (henceforth recovery efficiency) low-enthalpy HSA resources. A case-study is presented from the West Netherlands Basin (WNB) in the Dutch province of Zuid-Holland with an overview of key-parameters of the on-going geothermal exploitation. Based on trends of the geothermal expansion rate, predictions were made on future annual heat production, the recovery efficiency and available production license space in the WNB. In the second part of this study, we compare results of flow and heat transfer simulations for the WNB aquifer exploitation with the current ‘first-come, first-served’ doublet deployment and the ‘masterplan’ approach to doublet deployment.

The WNB is selected as the study area because of the availability of geothermal operational data, studies on regional heat demand [32–34], as well as extensive geothermal potential studies and Heat in Place (HIP) evaluation [17,35]. Moreover, it was the epicentre of geothermal development in the Netherlands, the country with one of the fastest expansions of geothermal development in Europe in the past decade [36,37]. Current geothermal doublets are operated by independent operators and mainly provide heat for the large greenhouse sector. The main aquifer targets are formed by fluvial sandstones of the Lower Cretaceous Nieuwerkerk Formation at depths between 2 and 3 km (e.g., [38–40]). The estimated HIP of this formation is 52,000 PJ [33], which could potentially cover the regional heat demand of 120 PJ/yr the province of Zuid-Holland [41] for decades with a low carbon footprint [42]. After the first doublets in the basin confirmed this significant geothermal potential, a next challenge is to make sure this resource is exploited efficiently increasing the role of geothermal heat production in a future low-carbon energy mix. In Section 2 of this paper, the geothermal development in the WNB is evaluated and predictions for future expansion are made. Section 3 describes how numerical production simulations are employed to explore the scope of optimisation of heat recovery from the main geothermal resource in the WNB. The results of the numerical simulations are presented in Section 4 and discussed in Section 5.

## 2. Geothermal development in the West Netherlands Basin

### 2.1. Exploitation between 2007 and 2018

From 2007 to 2018, 13 doublet systems have been realised in the WNB (Fig. 1). Challenges for efficient doublet deployment in the future are evident from this figure. Available space for new operators is limited by the extend of the main aquifer target, a mandatory distance of faults, hydrocarbon fields and the irregular shape and layout of licences that have been granted to independent operators. An overview of key parameters of this development is presented in Table 1. These parameters include doublet capacity in  $\text{MW}_{\text{th}}$ , aquifer name, area of influence, combined screen length as a proxy for net-aquifer thickness, injector-producer spacing, production rates and production temperatures and start date. The parameters values were derived from ‘End-Of-Well’ reports from the publicly available database Nlog.nl [32], and from the database of the Netherlands Enterprise Agency [33]. Most doublets in the WNB exploit aquifers of the Lower Cretaceous Nieuwerkerk Formation. The True Vertical Depth (TVD) ranges from 1850 to 2480 m (Table 1). An increase of doublet production rate could be recognised in newer doublets. Doublets that have been realised before 2015 were designed for production rates of up to  $200 \text{ m}^3/\text{h}$ , whereas newer doublets operate at rates between 250 and  $360 \text{ m}^3/\text{h}$ . As a result, the capacity of the doublet increased up to  $18 \text{ MW}_{\text{th}}$ . Injector-producer

spacing ( $L$ ) ranges from 1 to 2.1 km with an average of 1.6 km.  $L$  is derived from ‘End-Of-Well’ reports or interference test reports. We derived  $L$  as from the horizontal distance between top of the production and injection liners of the doublets was used to determine  $L$ . The values are provided in kilometres and rounded off to 1 decimal. A course indication of injector-producer spacing is indicated here, whereby we neglected the impact of the slight tilting of the aquifer, and the increasing  $L$  along the wellbore because the wells are deviated with a  $30\text{--}50^\circ$  angles [32]. The tilting angle of the aquifer could be estimated assuming a  $3.5 \text{ m/ms}$  seismic velocity at  $2.5 \text{ km}$  depth [43] and recognising  $\sim 250 \text{ ms}$  Two Way Travel-time difference of the top of the Nieuwerkerk over  $10 \text{ km}$  in one of the WNB fault blocks from Willems et al. [40]. Such a TWT difference would result in some tens of meters over a typical injector producer spacing of  $1\text{--}2 \text{ km}$ . Furthermore, exact calculation of the injector producer spacing at aquifer level is complicated by uncertainty in aquifer thickness of several tens of meters [40]. The associated area of influence ( $A$ ) that captures the expected extent of the cold-water plume at the moment of cold-water breakthrough is approximated by:  $A = 2L^2$ . In the WNB,  $A$  ranges between  $2$  and  $7.2 \text{ km}^2$ , with an average of  $5.4 \text{ km}^2$ . The associated energy production per square kilometre is  $1.1\text{--}4.7 \text{ MW}/\text{km}^2$ , with an average of  $2.4 \text{ MW}/\text{km}^2$ . Note that for recently drilled doublets not all parameters could be listed. This is because data was not publicly available, or doublets are still in a test/workover phase. Values in italic indicate that they are derived from prognoses instead of measurements.

### 2.2. Future expansion of WNB geothermal exploitation

Between 2007 and 2018, the average expansion rate of the installed capacity was  $13 \text{ MW}_{\text{th}}/\text{yr}$  (Fig. 2A). In the last four years, an increased expansion rate could be recognised of  $24 \text{ MW}_{\text{th}}/\text{yr}$ . With these expansion rates, the total installed capacity could be either  $540$  or  $1000 \text{ MW}_{\text{th}}$  in 2050 (Fig. 2A). Subsequently, the potential annual heat production in the basin is determined by integrating the total installed capacity in  $\text{MW}_{\text{th}}$  over time and assuming an annual downtime of 20%. The associated annual energy production will be approximately  $18$  for the expansion rate of  $13 \text{ MW}_{\text{th}}/\text{yr}$  and  $30 \text{ PJ}$  for the expansion rate of  $24 \text{ MW}_{\text{th}}/\text{yr}$  in 2050 (Fig. 2B). Schoof et al. [9] defined a target of  $50 \text{ PJ}/\text{yr}$  of geothermal heat production in the Netherlands in 2030. This target could only be met if geothermal exploitation both within and outside the WNB would expand at significantly higher rates, which are shown in Fig. 2A. The recovery of the available geothermal heat is expressed in terms of the recovery efficiency ( $R$ , Eq. (1)) and in the Heat Demand Coverage (HDC, Eq. (2)), the percentage of the regional heat that is covered by geothermal exploitation. The recovery efficiency is derived from dividing cumulative heat production ( $E_{\text{cu}}$ ) by  $52,000 \text{ PJ}$ , the estimated HIP in the main Lower Cretaceous aquifer target by Kramers et al. [35]:

$$R = E_{\text{cu}}/\text{HIP} \quad (1)$$

HDC is derived by dividing the total combined installed capacity of all doublets ( $C_T$ ) [ $\text{MW}_{\text{th}}$ ] by the total annual heat demand ( $H_D$ ) [ $\text{MW}_{\text{th}}$ ] in the province of Zuid-Holland which was  $120 \text{ PJ}/\text{yr}$  in 2016 according to [41]:

$$\text{HDC} = C_T/H_D \quad (2)$$

In 2018, HSA exploitation provided approximately 4% of Zuid-Holland heat demand (Fig. 2C). In 2050, this could increase to approximately 15–25% depending on the expansion rate trend. Even in the more optimistic expansion trend of  $24 \text{ MW}_{\text{th}}/\text{yr}$ , some 0.75–1.2% of the HIP would be recovered (Fig. 2D). Fig. 2C and D underline that a different doublet deployment strategy is required to increase the percentage of geothermal heat in a future low-carbon energy mix and to optimise heat recovery.

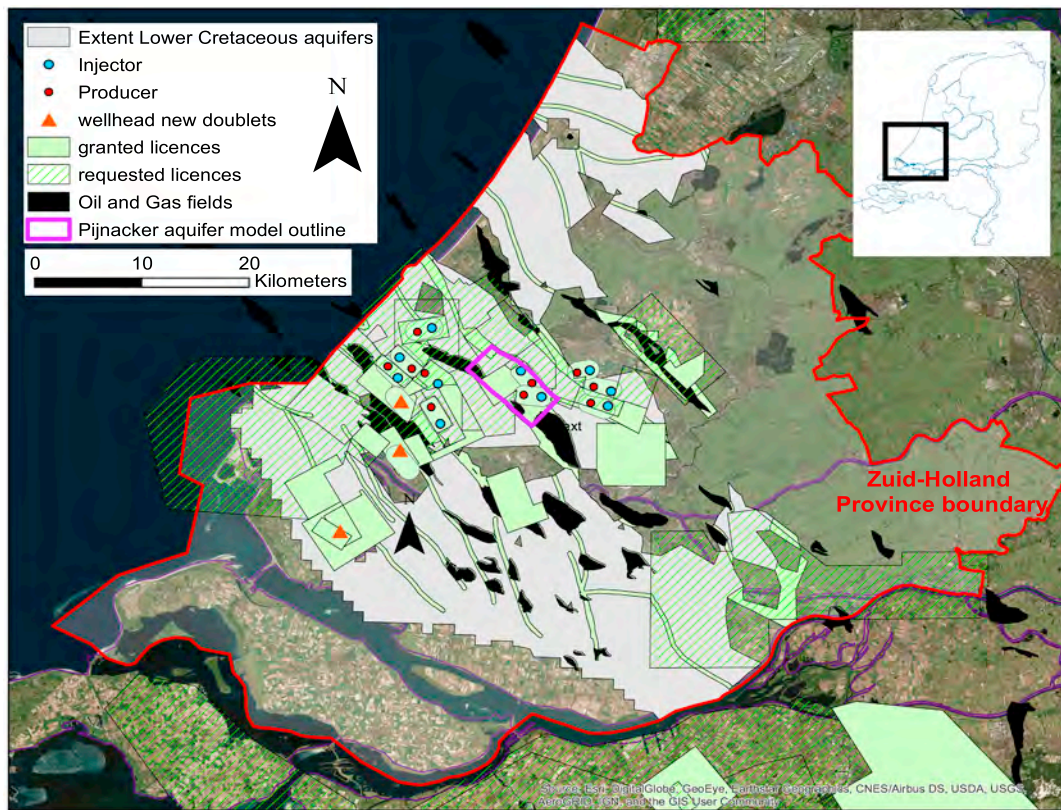


Fig. 1. Overview of geothermal activity in the province of Zuid-Holland (red border). Red and blue dots indicate the location of injectors and producers at aquifer level. For three new doublets the well trajectories are unknown and only the wellhead (i.e. the surface termination of a wellbore) locations are shown (orange triangles).

2.3. Available space for production licenses in the WNB

When the installed capacity will continue to grow with 13 MW<sub>th</sub>/yr, some 50 doublets will have been realised by 2050. Assuming an that the average injector-producer spacing of the doublets remains 1.6 km (Table 1), it was calculated that these 50 doublets will cover some 225 km<sup>2</sup>. This is approximately 20% of the surface area below which Lower Cretaceous aquifers are expected to have sufficient potential according to Pluymaekers et al. [44]. When the expansion rate of geothermal exploitation is faster, for example 24 MW<sub>th</sub>/yr like in the past four years, some 80 doublets can be realised by 2050, occupying some 35% of the surface area below which the aquifer has sufficient

potential. Note that in both expansion scenarios, not even 1% of the HIP will be recovered in 2050 (Fig. 2D) and pressure interference will become increasingly imminent [45]. Therefore, Fig. 3 shows that a change in doublet deployment and permitting strategy is required to increase the number of doublets and heat recovery efficiency in this basin.

3. Method

3.1. Study area, aquifer model, heat demand

In a second phase of the study, numerical production simulations are employed to compare the recovery efficiency and HDC for different

Table 1

Performance indicators of WNB doublets. Grey italic values are derived from prognoses. R. GR: Rijnland Group aquifer, N. Fm. Nieuwerkerk Formation aquifer., Buntsst.: Buntsandstein aquifer.

Nr	Start	Aquifer	TVD [m]	Spacing (L) [km]	Area of influence (A) [km <sup>2</sup> ]	Production rate [m <sup>3</sup> /h]	Production temperature [°C]	Screen length [m]	Capacity [MW]	MW/km <sup>2</sup>
1	Aug-07	R. Gr.	1659	1.7	5.8	170	57	103	9	1.6
2	Sep-09	N. Fm.	1859.5	1.0	2.0	150	64	57	7.3	3.7
3	Aug-10	N. Fm.	2264	1.5	4.5	180	70	86	7	1.6
4	Dec-10	N. Fm.	2305	1.8	6.5	–	78	87	7	1.1
5	Feb-11	N. Fm.	2352.5	1.6	5.1	180	70	100	8	1.6
6	Jun-12	N. Fm.	2539	1.5	4.4	180	85	50	11.5	2.6
7	Sep-14	N. Fm.	2449	1.6	5.1	185	90	200	16	3.1
8	Oct-15	Buntsst.	2173	1.7	5.8	255	83	200	14	2.8
9	Dec-16	N. Fm.	2460	2.1	8.8	300	87	124	16	1.8
10	Mar-17	N. Fm.	2480	1.9	7.2	–	85	224	16	2.2
11	Nov-17	N. Fm.	–	–	–	–	95	–	18	–
12	Dec-17	N. Fm.	2473	1.5	4.5	360	87	83	21	4.7
13	Jan-18	N. Fm.	1855	1.6	5.4	360	65	93	15	2.8
<b>Average</b>			<b>2239</b>	<b>1.6</b>	<b>5.4</b>	<b>232</b>	<b>78</b>	<b>117</b>	<b>13</b>	<b>2.4</b>

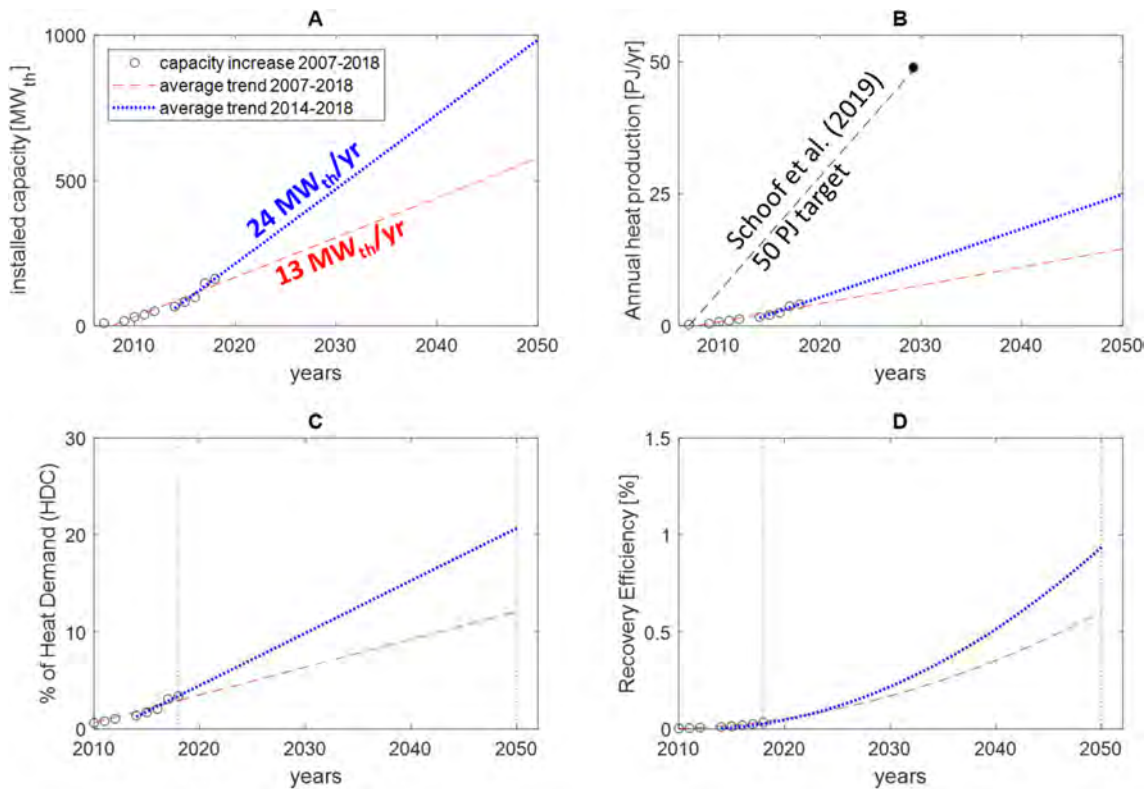


Fig. 2. Predictions of future geothermal development in the WNB based on past development trends for (A) total combined installed capacity, (B) Annual energy production with the expansion rates in (A) as well as for the Dutch national target of Schoof et al. [9], (C) Heat Demand Coverage (HDC) and (D) Recovery efficiency.

deployment strategies. For this purpose, an aquifer model of the main WNB target, the Lower Cretaceous Nieuwerkerk Fm. is created for the Pijnacker fault block (Fig. 4). For the sake of simplicity, the aquifer is modelled as a homogeneous and horizontal sandstone layer with constant thickness. For the development of an optimised exploitation strategy, reservoir heterogeneity for flow properties would have to be considered [13], but this is out of the scope of this study. The model consists of a horizontal 100 m thick homogeneous sandstone layer, which is confined between 300 m impermeable over- and under-burden layers providing thermal recharge (Fig. 4). The thickness is derived from averaging aquifer thickness of currently active doublets in the WNB. Two of the four boundaries of the model are formed by the northwest to southeast trending faults, derived from the WNB structural analysis of Duin et al. [46]. The aquifer properties are assumed isotropic and values are derived from Willems et al. [45] (Table 2). Element size ranged from 0.3 m to 40 m in the aquifer layer and from 40 m to 300 m in the over- and under-burden layers. The total heat demand in the surface area covered by the aquifer model is approximately 80 MWth (Fig. 4). The aquifer model has a surface area of 24.5 km<sup>2</sup> and the average surface heat demand of 3.8 MW<sub>th</sub>/km<sup>2</sup> (based on heat demand values for horticulture and domestic heating for both municipalities derived from the Dutch National Energy Atlas [34]). The heat demand in our study area is higher than the current geothermal heat production per square kilometre in the province of Zuid-Holland of 2.4 MW<sub>th</sub>/km<sup>2</sup>.

### 3.2. Doublet deployment scenarios

Heat exploitation from the introduced aquifer model is considered by utilising three doublet deployment scenarios. In the first scenario, 3 doublets are deployed. This scenario represents the currently applied ‘first come, first served’ deployment strategy. Two doublets are exploiting the Lower Cretaceous aquifer in the Pijnacker fault block. A third exploration license is granted where a new doublet is planned in 2019 [47]. The injector-producer spacing in this scenario ranged from

1200 m for doublet 3, to almost 1700 m for doublet 1 (Fig. 5). Deployment scenarios 2 and 3 represent optimised deployment scenarios according to a ‘masterplan’ strategy. In scenario 2, nine doublets are deployed with an injector-producer spacing of 800 m. Following Willems et al. [45], the optimal distance ( $dx$ ) between individual doublets was 1040 m. Doublets were placed in a so called ‘checkerboard’ configuration whereby adjacent wells have opposite functions. In scenario 3, sixteen doublets are deployed in checkerboard configuration, but here the distance between individual doublets is equal to the injector-producer spacing, which is 800 m. For simplification, the production rate of all doublets is equal to 200 m<sup>3</sup>/h and production commenced at the same moment. These simplifications are made because the aim is to show that the recovery efficiency can be improved with optimised doublet deployment. We do not try to develop an optimised deployment strategy. To recognise interference in the doublet deployment scenarios 1, 2 and 3, two additional simulations with a single doublet and injector-producer spacing of 800 m and 1650 m, respectively, are conducted.

### 3.3. Thermal flow modelling

Numerical production simulations are used to calculate the net energy production and life time of the doublet in the different deployment scenarios. In the numerical modelling procedure, the energy balance is solved for a rigid medium fully saturated with water, with thermal equilibrium between the fluid and solid phases:  $\partial/\partial t (\rho C_p T) + \rho_w C_w \nabla \cdot (\mathbf{q} T) - \nabla \cdot (\lambda \nabla T) = 0$ . In this balance,  $t$  [s] is time,  $T$  [K] is the temperature,  $\rho$  [kg/m<sup>3</sup>] and  $C_i$  [J/(kgK)] are the temperature independent mass density and specific heat capacity, respectively. Subscripts reference to the rock ( $r$ ) and brine ( $w$ ) phase.  $\lambda$  [W/(mK)] is the thermal conductivity tensor  $\mathbf{q} = -K\mu\nabla\cdot\mathbf{h}$  is the Darcy velocity vector, with hydraulic conductivity  $K = k_r \rho_w g$ , where  $k_r$  [m<sup>2</sup>] is the sandstone or shale permeability,  $g$  gravitation acceleration and  $\mu$  the temperature dependent viscosity. The thermal conductivity tensor is calculated

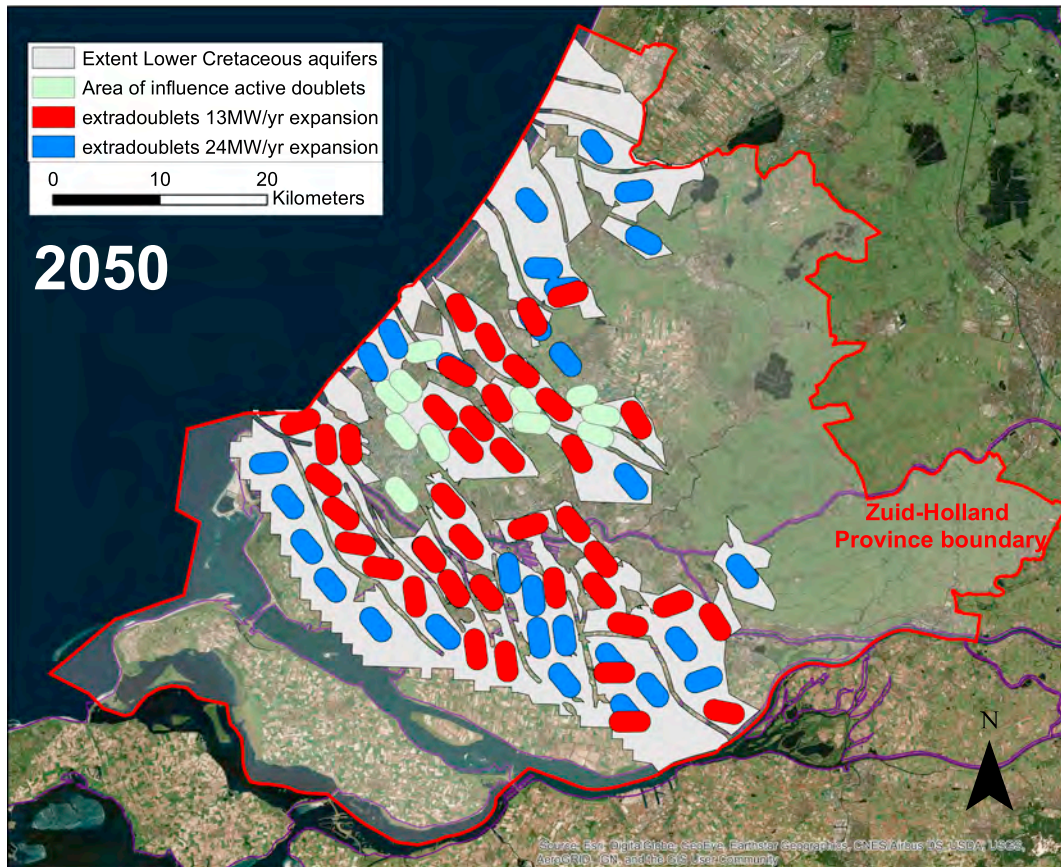


**Fig. 3.** Surface area covered by geothermal doublets in 2018 (green) and 2050 with expansion rate of 13 MW<sub>th</sub>/yr (red) or 25 MW<sub>th</sub>/yr (blue). The red line outlines the extent of the Province of Zuid-Holland and the black dashed polygon indicates the area with assumed sufficient geothermal potential of the Lower Cretaceous aquifers according to Plummaekers et al. [44].

through:  $\lambda = (\lambda_{eq} + (\alpha_T)|\mathbf{q}|)I + \rho_f C_f (\alpha_L - \alpha_T) \mathbf{q}\mathbf{q}/|\mathbf{q}|$ . In this equation,  $|\mathbf{q}|$  is the magnitude of the Darcy velocity vector,  $I$  is the identity matrix,  $\alpha_L$  and  $\alpha_T$  are the thermal dispersion coefficients in the longitudinal and transversal direction, respectively. The approach of Diersch [48] is followed using the empirical viscosity temperature dependency of Mercer and Pinder [49]. The equivalent heat conductivity, density and the volumetric heat capacity are assumed to be independent of temperature for simplicity and described by:  $\lambda_{eq} = (1 - \phi)\lambda_r + \phi\lambda_w$  and  $\rho C = (1 - \phi)\rho_r C_r + \phi\rho_w C_w$  in which  $\phi$  is the porosity. The pressure field is obtained through solving the continuity equation:  $\phi (\partial\rho_w)/\partial t + \nabla \cdot (\rho_w \mathbf{q}) = \rho_w S$ , where  $S$  [s<sup>-1</sup>] is external sinks and sources. The detailed modelling procedure follows the approach explained in Saeid et al. [50,51]. The values of all constant parameters are listed in Table 2. The production simulations yield a production temperature development over time and the required injection and production pressure for the associated production rate and set of parameters. A constant temperature boundary condition of 75 °C was assigned to the top and base of the aquifer model. Another temperature boundary condition is assigned to the nodes of the injection well trajectories of 35 °C. The two long edges of the model representing the faults flanking the aquifer model are no-flow boundaries. The short edges of the model are open-flow boundaries. Fig. 4 presents an overview of these boundary conditions.

### 3.4. Net energy production

The production simulations yield a production temperature development over time and the required injection and production pressure for the associated production rate. The difference between injection and production pressures ( $\Delta P$ ) is used to estimate pump energy losses:  $E_{pump} = (Q\Delta P)/\varepsilon$  (e.g., [52]), where  $Q$  is the production rate and  $\varepsilon$  the

pump efficiency of 60%. The produced power ( $E_{prod}$ ) is estimated by:

$$E_{prod} = Q\rho_w C_w (T_{prod} - T_{inj}) \quad (3)$$

In Eq. (3),  $T_{inj}$  is the injection temperature of 35 °C and  $T_{prod}$  is the production temperature that changes over time after thermal breakthrough. The net energy ( $E_{net}$ ) production is determined by the sum of the produced energy and the pump energy losses. Integration of  $E_{net}$  over the production time gives the cumulative energy production. In this calculation, the net energy production is reduced by 20% to account for maintenance down-time. To obtain the recovery efficiency, the cumulative produced heat is divided by the HIP of the aquifer model, following Eq. (1). This HIP is estimated by:  $HIP = V (T_{prod} - T_{inj}) (\phi C_w \rho_w + (1 - \phi) C_{sst} \rho_{sst})$ , where  $V$  is the bulk rock volume of the active aquifer and  $C_{sst}$  is the heat capacity of sandstone (sst) (Table 2).

### 3.5. Levelized Cost of Heat

The Levelized Cost of Heat (LCOH) is determined for each doublet deployment scenario, using Eq. (4):

$$LCOH = \frac{\sum_{t=1}^n \frac{CAPEX_t + OPEX_t}{(1+r)^t}}{\sum_{t=1}^n \frac{E_{net,t}}{(1+r)^t}} \quad (4)$$

In this equation,  $CAPEX_t$  and  $OPEX_t$  are the respective total Capital and Operational expenses in year  $t$ , which are derived from  $n$  the parameters listed in Table 3,  $r$  is the discount rate and  $E_{net,t}$  is the cumulative generated amount of heat in year  $t$ , which is derived from the production simulations. A fifteen-year period is chosen because this relates to the maximum duration of the Dutch feed-in tariff subsidies

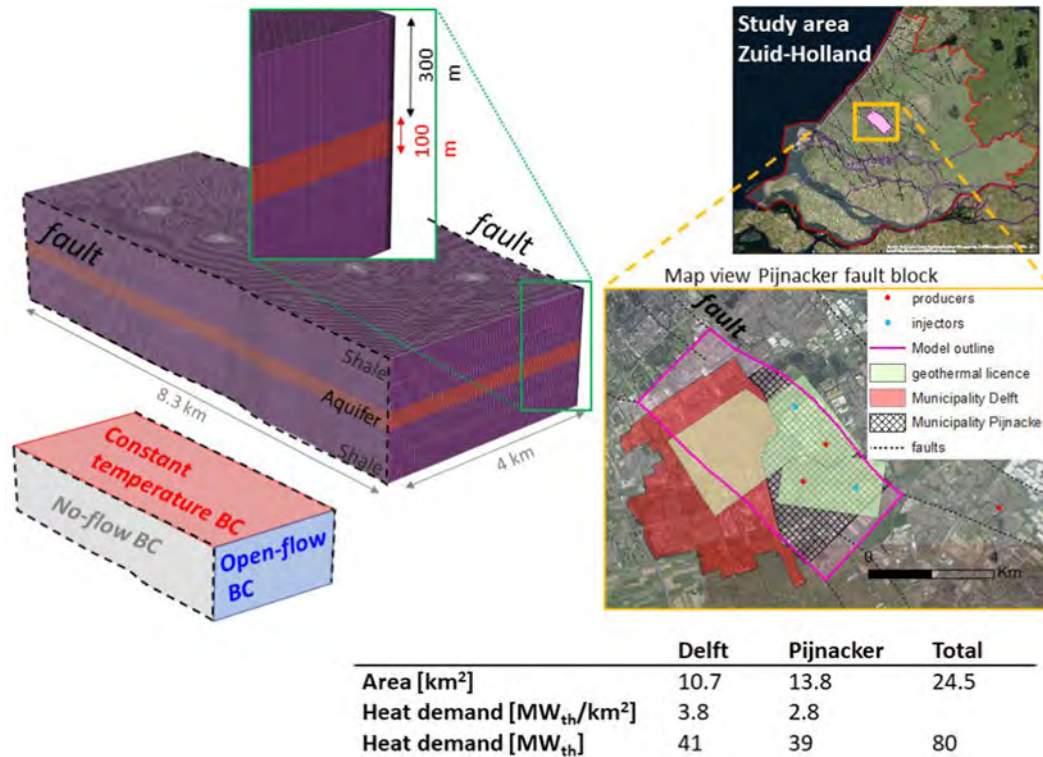


**Fig. 4.** Overview of the Pijnacker aquifer model. On the left, the aquifer model with vertical exaggeration and grid block outlines. The purple layers are the impermeable over- and under-burden that provide thermal recharge to the aquifer layer (red). Boundary conditions (BC) for the numerical flow modelling are indicated in the bottom-left of the figure. On the right, the location of the model in the WNB confined between the northwest to southeast trending faults, the location of currently applied geothermal licences, the location of active injector and production wells at aquifer level and a table showing the calculation of heat demand for horticulture and space heating in the surface area overlying the aquifer model.

**Table 2**  
Aquifer and fluid properties used in the numerical simulations.

Property		Value	Units
Sandstone porosity	$\phi_{sst}$	28	[%]
Shale porosity	$\phi_{sh}$	10	[%]
Sandstone permeability	$k_{sst}$	1000	[mD]
Shale permeability	$k_{sh}$	1	[mD]
Specific heat capacity sandstone	$C_{sst}$	1.93	[MJ/m <sup>3</sup> /K]
Specific heat capacity shale	$C_{sh}$	2.47	[MJ/m <sup>3</sup> /K]
Thermal Conductivity Sandstone	$\lambda_{sst}$	2.7	[J/m/s/K]
Thermal Conductivity Shale	$\lambda_{sh}$	2	[J/m/s/K]
Density Sandstone	$\rho_{sst}$	2650	[kg/m <sup>3</sup> ]
Density Shale	$\rho_{sh}$	2600	[kg/m <sup>3</sup> ]

[53]. ESP pump replacement costs have been considered for each injection well in the sixth and eleventh year. Using the LCOH as performance indicator, the financial advantage of optimisation of heat exploitation is quantified for each doublet deployment scenario and compared to the LCOH of conventional gas heating [54].

In our CAPEX calculations we assume that if a single operator exploits the entire aquifer model, this would require an investment for a surface heat distribution grid for selling the produced heat. We neglect these costs for operators with only a single doublet because we assume that in this scenario the geothermal doublet provides heat to an existing decentralised grid. We assume a simplified heat grid that connects all doublets in the three scenarios with associated heat grid costs ( $C_{grid}$ ) estimated by:  $C_{grid} = (N - 1) \cdot dx \cdot C_{netw}$ . In this equation  $N$  is the number of doublets,  $dx$  [m] is the doublet distance in each scenario, and  $C_{netw}$  is the network costs of 1000 €/m following Daniilidis et al. [56] (Fig. 6). Our heat grids only connect the doublet wellheads (i.e. the surface termination of a wellbore). We neglect additional costs for connecting the grid to heat customers because that would require additional heat

consumer analyses, which is out of the scope of this study.

## 4. Results

### 4.1. Production temperature development and doublet life time

Results of the numerical production simulations show that with deployment scenario 1, it could take more than some 140 years before the production temperature will drop below uneconomic temperatures for space heating (70 °C, [1]). In one of the doublets, the production temperature drops faster than that of the single doublet reference simulation due to its proximity to the north western model boundary. Thermal breakthrough occurs after approximately 90 years in scenario 1. After thermal breakthrough, the net energy production reduces. In scenario 1, it takes between 140 and 200 years for the capacity to drop by 1 MW<sub>th</sub>. In deployment scenarios 2 and 3, the smaller injector-producer spacing of 800 m and closer doublet distance reduce the thermal breakthrough time significantly to approximately 25 years. Nevertheless, the production temperature does not drop below the minimal required temperature for 45 °C for greenhouse heating ( $T_{min}$  greenhouse, [1]) in 200 years in scenario 2 and 100 years in scenario 3. The minimal required temperature for space-heating of 70 °C is reached in ~40 years in scenario 3 and in 50 years in scenario 2. The results in Fig. 7 show that not only well spacing ( $L$ ) but also the doublet distance ( $dx$ ) affects the life time of the doublets (see Fig. 6 for comparison of  $L$  and  $dx$ ). In scenario 2 and 3, the doublets have the same injector-producer spacing ( $L$ ) of 800 m, but the distance between each doublet ( $dx$ ) is different. In scenario 3, 16 doublets are deployed with an average doublet distance of 800 m. In scenario 2, 9 doublets are deployed, and the average distance between each doublet is 1040 m. Because of the smaller doublet distance, the production temperature and the associated capacity in MW<sub>th</sub> reduces faster after thermal breakthrough in

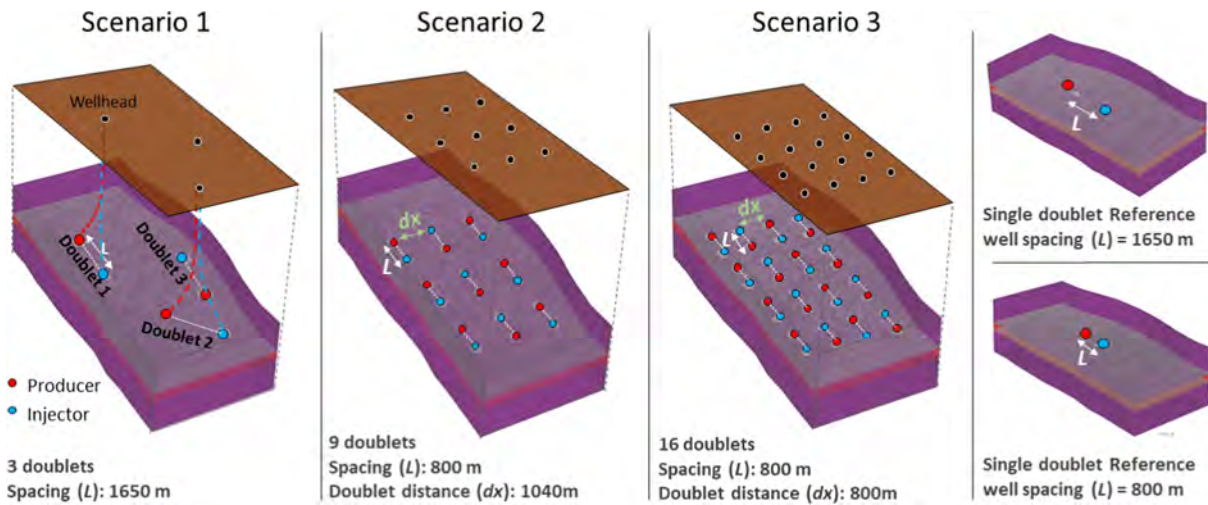


Fig. 5. Doublet deployment scenarios 1, 2 and 3. Well trajectories are only shown in scenario 1 and the well intersection with the aquifer indicated by the red and blue dots. Black dots indicate the surface location of the wellheads (i.e. the surface termination of a wellbore) of the different doublets.

**Table 3**  
Economic parameters for the LCOH calculations based on Van Wees et al. and Daniilidiis et al. [55,56].

Economic parameters		
Electricity price for operations	0.08	EUR/GJ
Discount rate (r)	7	%
CAPEX		
Well costs	2	M€/km
Drilling location costs	1	M€
ESP	0.80	M€
Gas separator	0.21	M€
Heat exchanger	0.10	M€
Geological risk insurance [53]	0.69	M€
Surface heat distribution network		
Single doublet	1	M€
Deployment scenario 1	6.6	M€
Deployment scenario 2	12.8	M€
Deployment scenario 3	24	M€
OPEX	5	% of Capex/yr
electricity price	0.073	EUR/kWh

deployment scenario 3. In scenario 2, the capacity of the doublets is reduced with 50% in 100 years. In scenario 3, the capacity of the doublets reduces to 50% of their original value after some 60 years. This shows that, geothermal production licences that target the same aquifer cannot be regarded as stand-alone features because interference is inevitable when multiple operators exploit the same aquifer. The spread

of the curves in scenario 2 and 3 is a result of slight variations in well spacing and doublet spacing of up to  $\pm 50$  m and the proximity of some doublets to no-flow boundaries.

Higher production rates will increase doublets capacity, but also result in earlier thermal breakthrough and faster reduction of the production temperature thereafter. Fig. 8A–C compare the production temperature development for simulations with production rates of 200 and 400 m<sup>3</sup>/h. Fig. 8D–F compare the associated development of the capacity of each doublet. As a result of the more rapid reduction of production temperature, the capacity of most of the doublets with 400 m<sup>3</sup>/h drops below that of doublets with 200 m<sup>3</sup>/h after 50 years in deployment scenario 2 (Fig. 8E), and after some 40 years in deployment scenario 3 (Fig. 8F). The results in Fig. 8 highlight that an optimised exploitation strategy requires a trade-off between doublet capacity and well density as well as the minimum required production temperature.

#### 4.2. Heat recovery efficiency – Pijnacker aquifer model

With the current ‘first come, first served’ deployment strategy (scenario 1) and doublets operating at 200 m<sup>3</sup>/h, geothermal exploitation could cover almost 40% of the heat demand of the surface area overlying the aquifer model (Fig. 9A). This could be increased to some 60% when the production rate of the three doublets is 400 m<sup>3</sup>/h. An even higher percentage of the regional heat demand could be covered by geothermal exploitation when more doublets are deployed like in scenario 2 and 3. This suggests that HSA exploitation could play a more significant role in the regional energy mix if doublets would be

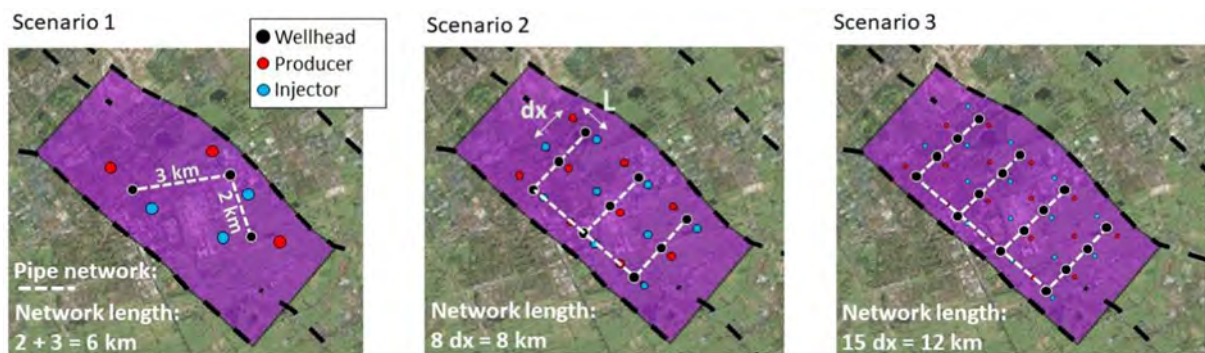


Fig. 6. Schematic map-view of the surface heat grid network (white dashed lines) length for three doublet deployment scenarios. It is assumed that operator that exploit multiple doublets need to invest in surface heat grids to sell their heat. Black dots indicate the wellhead surface locations.

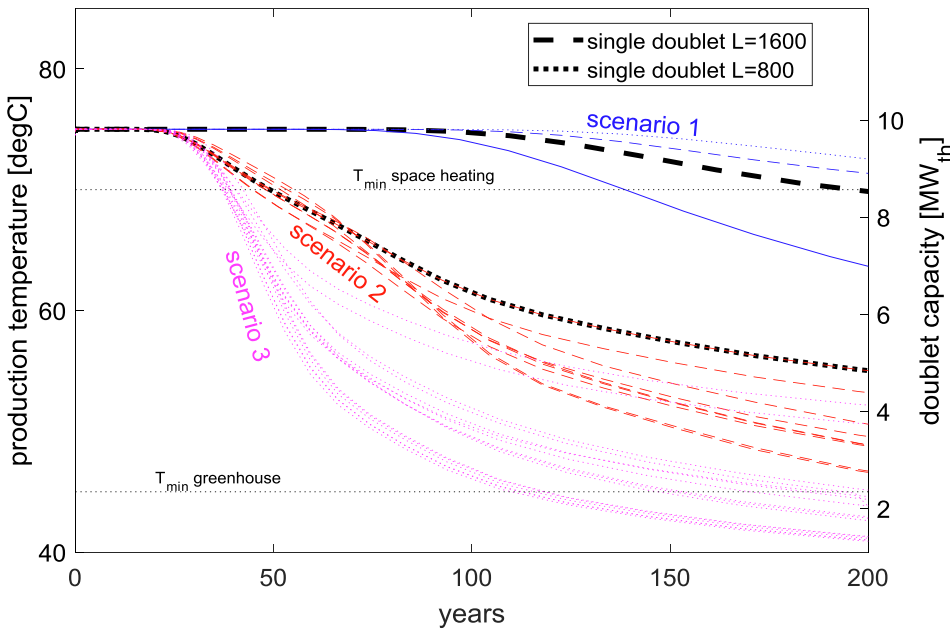


Fig. 7. Development of production temperature in doublet deployment scenario 1, 2 and with a constant production rate of 200 m<sup>3</sup>/h. The injector-producer spacing in scenario 1 is derived from Table 1 and in scenario 2 and 3 this spacing is 800 m for each doublet. Each line represents the production temperature development of a single doublet.

deployed with higher density according to a ‘masterplan’ approach. Fig. 9B shows that recovery efficiency could be enhanced in a similar way. with deployment scenario 1 and 200 m<sup>3</sup>/h production rate in each doublet, ~15% of the HIP could be produced in some 50 years. In simulations with scenarios 2 and 3, 40–65% of the HIP was produced in the same period of time. Because of the large and irregular well spacing in the current ‘first come, first served’ strategy, most of the heat in the acquirer remains untapped in scenario 1 at the moment of thermal breakthrough (Fig. 9C). The efficiency of heat extraction can be enhanced by denser doublet deployment like in scenarios 2 and 3 (Fig. 9D and E).

4.3. Financial impact of optimised doublet deployment

The Levelized Cost Of Heat (LCOH), calculated over a 15 year period, is compared for different doublet deployment scenarios in Fig. 10. Our calculations result in a LCOH for exploitation with a single doublet of approximately 3 €ct/kWh. This is in between the assumed LCOH with ‘today’s technology’ by Beckers et al. [57] and the Dutch gas heating price according to ECN [54]. The LCOH does not reduce for operators that exploit three doublets at the same time, like in deployment scenario 1. Only a very small reduction in LCOH could be recognised for deployment scenarios 2 and 3. Production rate increase has a much more significant impact on LCOH. The LCOH calculation for the

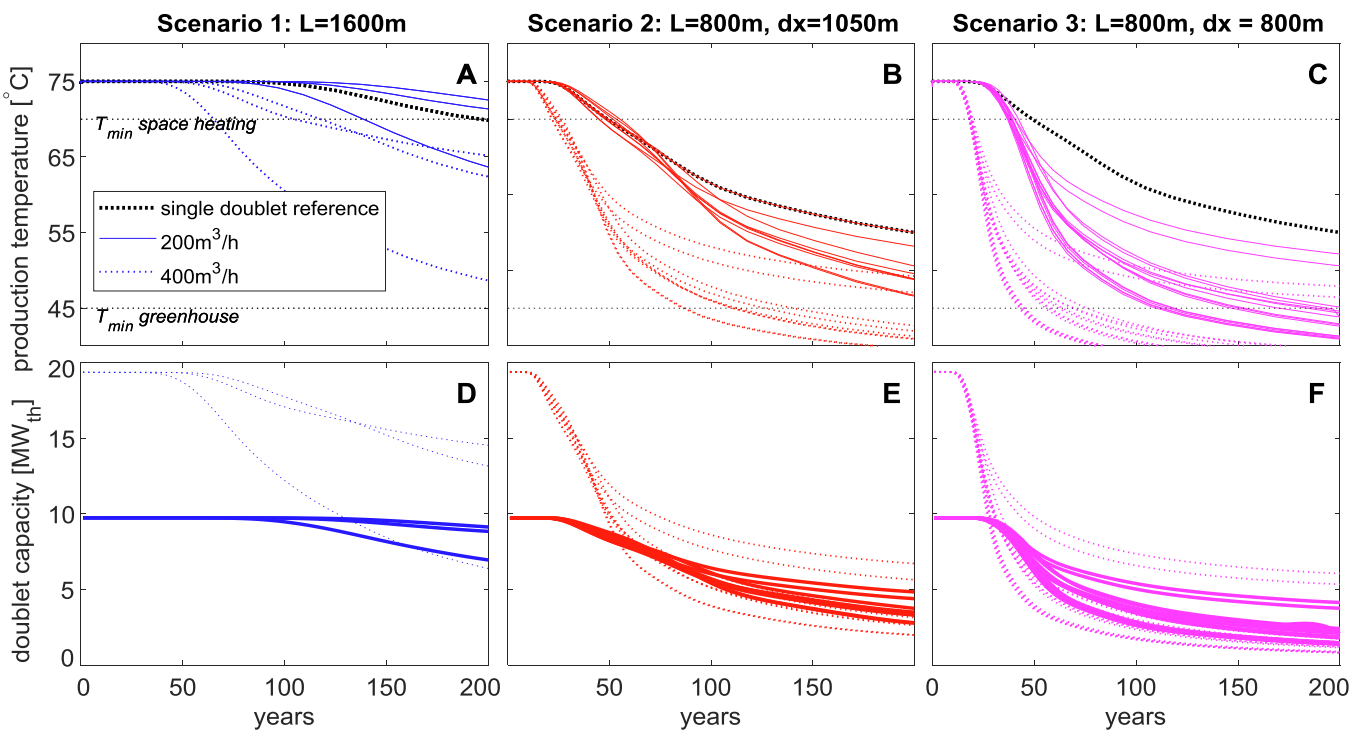
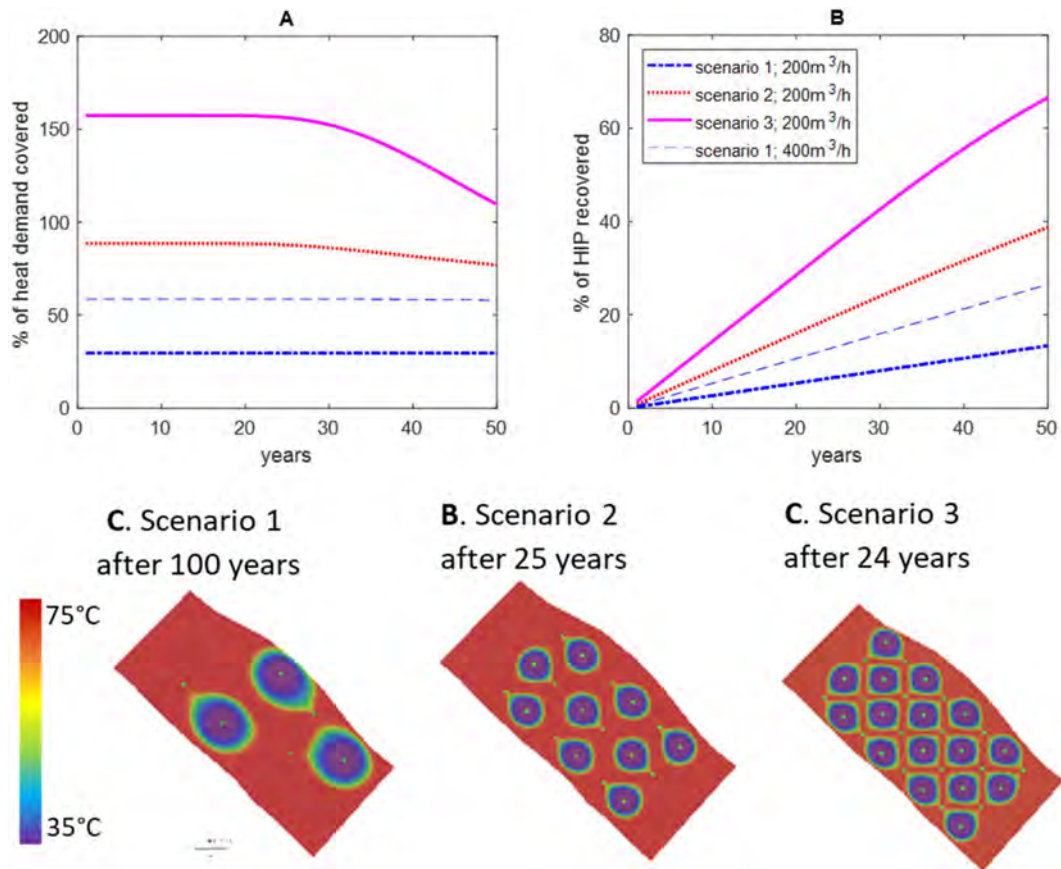
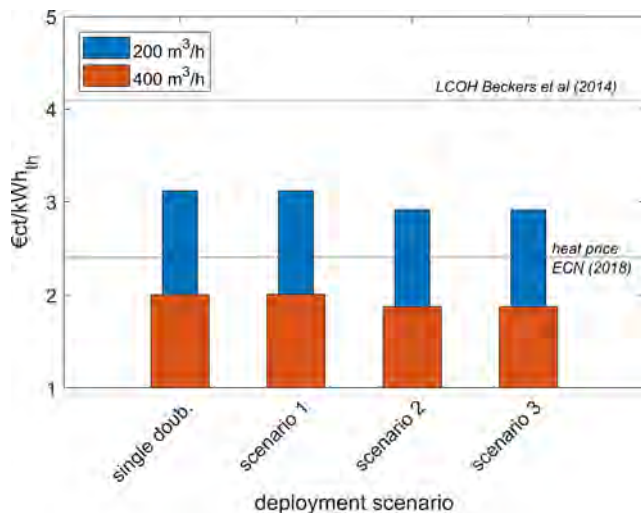


Fig. 8. Impact of production flow rate on production temperature development (A–C) and capacity (D–F), for each doublet in the different deployment scenarios (columns). Dotted lines represent simulation results with 400 m<sup>3</sup>/h production rates, solid lines represent production simulations with 200 m<sup>3</sup>/h production rates.



**Fig. 9.** (A) Percentage of surface heat demand of the Pijnacker aquifer model (Fig. 4) that is produced from the aquifer for the three doublet deployment scenarios. (B) Percentage of the HIP that is produced based on 20% annual down time and 200 m<sup>3</sup>/h production rate for all doublets. (C–E) Map view of the temperature distribution projected on a horizontal slice in the aquifer on when thermal breakthrough occurs in deployment scenarios 1, 2 and 3.



**Fig. 10.** Levelized Cost of Heat (LCOH) calculations for different deployment scenarios and 15 year production period assuming 20% annual downtime (blue-diamond markers) and 40% annual downtime (red, circle markers). For reference, the LCOH value of heat for direct-use applications by Beckers et al. [57] and the heat price of traditional gas heating are indicated.

simulations with 400 m<sup>3</sup>/h production rates drops to approximately 2.0 €/kWh for deployment scenario 1 and single doublet deployment, and 1.9 €/kWh for deployment scenario 2 and 3. Note that we included additional 25% CAPEX costs that would be required to upscale well diameter and surface facilities to accommodate for the increased flow rates. These calculations suggest that for current operators in the WNB

no financial incentive exists that promotes upscaling exploitation. There is no significant financial advantage of the ‘masterplan’ doublet deployment that could potentially increase the heat recovery efficiency as was shown in Fig. 9A. For individual operators it is financially more attractive to optimise heat production of a single doublet, then to consider optimisation of the heat recovery efficiency.

## 5. Discussion

### 5.1. Heat recovery efficiency

The pioneering first geothermal projects in the WNB proved the technical potential of HSA exploitation. The next challenge for this new industry is to optimise heat exploitation strategies to utilise the full potential of these resources. This study presents predictions of the current and future role of geothermal heat production in the region. Our results show that with the current expansion rate of the installed geothermal capacity the recovered heat will only be approximately 1% or less of the estimated HIP in 2050. This is much lower than the estimated recovery efficiency values of 20–30%, which are typically used in HSA potential studies [2,19,35,55]. Our simulations do not aim to provide an optimal exploitation strategy, but we aim to show that there is a significant scope for optimisation of the recovery efficiency of heat from HSA resources. With a regional approach to doublet deployment, significantly more heat could be extracted from HSA and geothermal heat exploitation could play a larger role in the low-carbon energy mix of the province of Zuid-Holland and similar regions world-wide than it does today. Our estimation of the recovery efficiency in the WNB could be refined by improving the HIP estimate. In calculation of the HIP in the WNB, Kramers et al. [35] considers neither the uncertainty of the

specific heat capacity, porosity and variation of the required injection and production temperature nor the significant impact of thermal recharge on the amount of recoverable heat [58]. Especially because of the significant impact of thermal recharge, we expect that the HIP is actually much larger and therefore our recovery efficiency calculations are still conservative. Other improvements of our recovery efficiency predictions could be made by incorporating fluctuating heat demand and associated variations in production rate in estimations of the total produced heat (Fig. 2B). We assume an annual down time of 20%, for example for maintenance, in calculating energy production from the capacity in  $MW_{th}$ . This assumption is made because actual annual heat production records are not available. Heat recovery might have been slower in the first 10 years because of extra downtime for unforeseen maintenance, but because of increasing exploitation experience this might be lower in the future. Our annual heat production calculations are based on values from Table 1, which are derived from ‘End of Well Reports’, and the websites of the geothermal branch-organisation [59] and governmentally managed publicly available databases. Therefore, these table entries represent snapshots of performance indicators and actual values may vary over time. Also, the regional heat demand derived of the Province of Zuid-Holland [41] may be subject to development in the future, which will affect the percentage of heat that geothermal exploitation could cover (Fig. 2C).

### 5.2. Expansion of geothermal exploitation in the WNB

In our analysis, we assumed linear growth trends for WNB geothermal exploitation. Several factors such as increasing demand for low-carbon heat or fluctuating process of conventional gas heating could have an impact on the growth trend of geothermal exploitation in the WNB. Finally, future expansion might be decelerated by the potential impact of interference and availability of space for new production licences. On the other hand, improved understanding of technical challenges may reduce costs for future operators, enhancing financial competitiveness and therefore also the expansion rate. For example, a major current challenge is the casing steel selection. Corrosion of casing- and Electrical Submersible Pump (ESP) systems had significant financial implications in the past years [60]. Improved and consistent hydro-chemical analyses of formation water in future studies are required to improve steel selection, reduce corrosion risk and accelerate exploitation further. Because the above-mentioned simplifications may have negative and positive impact on the recovery efficiency estimate, we expect that the order of magnitude of our estimations is still realistic. This study therefore emphasizes that a radical change is required in doublet deployment rates to make HSA exploitation a more significant contributor to the regional energy mix in Zuid-Holland.

### 5.3. Well placement optimisation

The numerical production simulations in this study are used to explore the potential scope for heat recovery optimisation from HSA resources from a reservoir engineering perspective. HSA exploitation is simulated utilising the current ‘first come, first served’ doublet deployment and an optimised deployment approach. The results suggest that the heat recovery efficiency could be increased by several tens of percentages when doublet deployment is coordinated according to a masterplan and when smaller injector-producer spacing distances are considered for doublets. The current WNB spacing standard of 1.6 km is derived from exploitation in the Paris Basin, where no thermal breakthrough has been observed, not even after 40 years of exploitation [23]. In our ‘masterplan’ deployment we use approximately half of the current WNB spacing. This is chosen to emphasize that the current standard might lead to unnecessary long breakthrough times and reduces the possible number of doublets that can exploit the aquifer ([45,61], Fig. 7). Optimised well spacing and doublet deployment is basin

dependent and it should be derived based on detailed geological modelling. This is because the sedimentary facies architecture will reduce thermal breakthrough time when the same production rates are used but also reduce the rate of the production temperature decline after thermal breakthrough [13,61]. Optimal doublet deployment further depends on net aquifer thickness as well as the tilting of the aquifer, lateral thickness variation and aquifer background flow [45,62]. Also, logistical and financial factors must be considered related to the design of surface heat distribution networks, location of consumers as well as minimisation of drilling costs, which could affect wellhead locations at the surface. For simplification, neglected the time it would take to realise doublets. Increased insight of the geological heterogeneities will be obtained with an increasing number of wells. The masterplan should therefore be flexible enough to adopt with the future gained progressive insights on aquifer heterogeneities. In our simulations, doublets commence exploitation at the same time. In reality, it would take several months to realise doublets. This would reduce the cumulative heat production and recovery efficiency and affect the results of Fig. 9. Finally, the use of doublets may not be the most optimal method to extract heat from geothermal aquifers. Alternatively ‘triplet’ systems could be considered similar to the examples in the Paris Basin and the Soultz-sous-forets EGS system [23,63,64] or even more advanced injector-producer layout could be imagined. Several software tools have been developed that could aid in finding optimised well placement strategies [e.g. 65,66]. The impact of reservoir heterogeneity [13,16,67] on well placement optimisation should be also considered.

### 5.4. Implementation of masterplan deployment

Application of the ‘masterplan’ deployment approach has so far been hindered by the economic and legislative hurdles. The feed-in tariff schemes and geological risk insurance schemes made a significant contribution to initiate geothermal development in for example France, Germany and the Netherlands [23,53,68]. However, our LCOH calculations (Fig. 10) indicate that little financial incentive exists to promote heat recovery optimisation or the use of the ‘masterplan’ deployment approach. LCOH does not reduce for exploitation with deployment scenarios 2 and 3. If neighbouring operators would be able to significantly reduce their CAPEX by sharing surface facilities and investments for data acquisition and risk insurance, the LCOH could potentially be reduced with large scale exploitation. Also, larger-scale exploitation with multiple doublets would become attractive if the heat demand or market is far larger than the capacity of a single well. When neighbouring operators are connected to the same heat network, successful doublets could compensate unexpected poor performance of other doublets, which could be a result of local geological heterogeneities. One possible way to promote heat recovery optimisation could be through the creation of regional surface heat distribution networks. This would of course require a large upfront investment but Blom et al. [69] showed that such networks could be profitable as stand-alone infrastructure if users pay a fee for heat traffic. This type of government support was also provided by the Dutch government in the 60s to support gas exploitation after the discovery of the Groningen gas field. A national gas grid was installed connecting every household to the gas grid and ensuring long term domestic gas consumption in the Netherlands [70]. Not only financial support mechanisms but also permitting mechanisms need to be adapted to facilitate and promote heat recovery optimisation. Our production simulations show that interference is inevitable. In Article 42 of the Dutch mining law it is currently stated that neighbouring geothermal operators must come to an agreement in dealing with potential interference [71]. With increasing doublet density, and uncertainty on subsurface flow-paths of reinjected water (e.g., [62]), this will become increasingly challenging. Especially because no accurate methods for monitoring cold-water plume development or the area of influence of doublets are considered.

Interference is also a challenge in the exploitation of other types of geothermal resources. Differently from HSA exploitation, negative interference effects can more readily be solved in Aquifer Thermal Energy Storage (ATES) development [26,28] or high enthalpy geothermal electricity production [14,27], by varying operational parameters or drilling extra (injection) wells to improve sustainable exploitation. The low financial competitiveness of HSA heat production makes it more difficult to justify such measures. Upfront investment for the creation of adequate financial- and legislative incentives as well as coordination of doublet deployment plans are therefore required to enhance HSA exploitation. Our study emphasises that although geological aspects influence considerably operational boundary conditions, the main challenges for efficient HSA exploitation are related to ‘man-made’ hurdles such as economic competitiveness and conflicting interests of operators.

## 6. Conclusion

Results of this study show that exploitation of HSA with a ‘first-come, first-served’ approach by individual operators that only develop a single doublet system leads to sub-optimal use of geothermal resources. Geothermal exploitation could cover a significantly larger part of our heat demand, if well placement strategies follow a regionally coordinated ‘masterplan’ approach. Such an approach could focus on optimising the recovery efficiency. Instead, the commonly applied ‘first-come, first-served’ approach aims to cover heat demand of individual operators. So far, geothermal exploitation has been supported by various governments with pilot projects, feed-in tariff schemes and geological insurance schemes. New, tailor-made financial and legislative mechanisms are required to promote more efficient use of geothermal resources. The West Netherlands Basin is used as case study, but in general these results apply to Geothermal resource exploitation worldwide. We conclude that in the WNB:

- In 2018, geothermal heat exploitation provided approximately 4% of the total heat demand of the province of Zuid-Holland.
- The installed capacity grew with 24 MW<sub>th</sub> per year, in the past 4 years. With this expansion rate, geothermal heat exploitation could cover up to 20% of the heat demand in Zuid-Holland in 2050.
- Less than 0.1% of the estimated recoverable heat from Lower Cretaceous aquifers has been recovered so far. With the current expansion rates, this recovery efficiency might not have exceeded 1% by 2050.

The numerical production simulations show that for geothermal resource exploitation in general:

- Heat recovery efficiency of up to 30% can be reached, but this requires denser doublet deployment with smaller injector-producer spacing than the current WNB standard of some 1.6 km and co-ordinated doublet deployment.
- Heat recovery optimisation does not reduce LCOH under current financial support schemes.
- Higher doublet density than the current density in the WNB could still result in sufficient doublet life time but will result in higher interference. Tailor-made legislation is therefore required to facilitate exploitation of a single resource by multiple operators.

## Acknowledgements

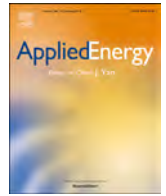
Part of this study is completed at the Department of Geoscience and Engineering, Delft University of Technology, Delft, Netherlands. We kindly thank the consortium of share- and stakeholders of the Delft Geothermal Project (DAP) for their support. The authors are grateful to G.J. Weltje (KU Leuven), M.E. Donselaar (TU Delft) and D.F. Bruhn (TU Delft) for inspiring discussions. Geothermal operators and Axel Sandén (Veegeo B.V.) in the Netherlands are thanked for the discussions and for

sharing their geological and production data. We thank MIKE for providing the academic licence of FEFLOW for the production simulations. Finally, we would like to thank the editor and anonymous reviewers for their help with revising this paper.

## References

- [1] Limberger J, Boxem T, Pluymaekers MPD, Bruhn DF, Manzella A, Calcagno P, et al. Geothermal energy in deep aquifers: a global assessment of the resource base for direct heat utilization. *Renew Sustain Energy Rev* 2018;82:961–75. <https://doi.org/10.1016/j.rser.2017.09.084>.
- [2] Gluyas J, Adams C, Busby JP, Craig J, Hirst C, Manning D, et al. Keeping warm: a review of deep geothermal potential of the UK. *J Power Energy* 2018;1–12. <https://doi.org/10.1177/0957650917749693>.
- [3] Mathiesen A, Nielsen LH, Bidstrup T. Identifying potential geothermal reservoirs in Denmark. *Geol Surv Denmark Greenl Bull* 2010;20:19–22.
- [4] Banks J, Harris NB. Geothermal potential of Foreland Basins: a case study from the Western Canadian Sedimentary Basin. *Geothermics* 2018;76:74–92. <https://doi.org/10.1016/j.geothermics.2018.06.004>.
- [5] Barkaoui A, Boldyryev S, Duic N, Krajacic G, Guzovic Z. Appropriate integration of geothermal energy sources by Pinch approach: case study of Croatia. *Appl Energy* 2016;184:1343–9. <https://doi.org/10.1016/j.apenergy.2016.04.112>.
- [6] Daniilidis A, Scholten T, Hooghiem J, De Persis C, Herber R. Geochemical implications of production and storage control by coupling a direct-use geothermal system with heat networks. *Appl Energy* 2017;204:254–70. <https://doi.org/10.1016/j.apenergy.2017.06.056>.
- [7] Geothermie Bundesverband. Geothermie statt Kohle – Erdwärme kann einen bedeutenden Beitrag zum Kohleausstieg leisten. *Pressemitteilung* 2018.
- [8] Harber A, Gillies I. Study into the potential for deep geothermal energy in Scotland, vol. 1. Edinburgh; 2013.
- [9] Schoof F, van der Hout M, van Zanten J, van Hoogstraten JW. *Masterplan Aardwarmte in Nederland* 2018.
- [10] OGA. Recovery factor benchmarking. London; 2017.
- [11] Babaei M. Integrated carbon sequestration – geothermal heat recovery: performance comparison between open and close systems. *Transp Porous Media* 2018. <https://doi.org/10.1007/s11242-018-1042-1>.
- [12] Vik HS, Salimzadeh S, Nick HM. Heat recovery from multiple-fracture enhanced geothermal systems: the effect of thermoelastic fracture interactions 500 m. *Renew Energy* 2018;121:606–22. <https://doi.org/10.1016/j.renene.2018.01.039>.
- [13] Crooijmans RA, Willems CJL, Nick HM, Bruhn DF. The influence of facies heterogeneity on the doublet performance in low-enthalpy geothermal sedimentary reservoirs. *Geothermics* 2016;64:209–19. <https://doi.org/10.1016/j.geothermics.2016.06.004>.
- [14] Williams CF. Updated methods for estimating Recovery Factors for geothermal resources. *Thirty-Second Work. Geotherm. Reserv. Eng., Stanford, California*; 2007. p. 7.
- [15] Salimzadeh S, Grandahl M, Medetbekova M, Nick HM. A novel radial jet drilling stimulation technique for enhancing heat recovery from fractured geothermal reservoirs. *Renew Energy* 2019;139:395–409. <https://doi.org/10.1016/j.renene.2019.02.073>.
- [16] Vasilyeva M, Babaei M, Chung ET, Spiridonov D. Multiscale modeling of heat and mass transfer in fractured media for enhanced geothermal systems applications. *Appl Math Model* 2019;67:159–78. <https://doi.org/10.1016/j.apm.2018.10.025>.
- [17] Van Wees JDAM, Kronimus A, Van Putten M, Pluymaekers MPD, Mijnlief H, Van Hooff P, et al. Geothermal aquifer performance assessment for direct heat production – methodology and application to Rotliegend aquifers. *Netherlands J Geosci* 2012;91:651–65.
- [18] Busby JP. Geothermal energy in sedimentary basins in the UK. *Hydrogeol J* 2014;22:129–41. <https://doi.org/10.1007/s10040-013-1054-4>.
- [19] Garg SK, Combs J. A reformulation of USGS volumetric “heat in place” resource estimation method. *Geothermics* 2015;55:150–8. <https://doi.org/10.1016/j.geothermics.2015.02.004>.
- [20] Ziabakhsh-Ganji Z, Nick HM, Donselaar ME, Bruhn DF. Synergy potential for oil and geothermal energy exploitation. *Appl Energy* 2018;212:1433–47. <https://doi.org/10.1016/j.apenergy.2017.12.113>.
- [21] Wang F, Deng S, Zhao J, Zhao J, Yang G, Yan J. Integrating geothermal into coal-fired power plant with carbon capture: a comparative study with solar energy. *Energy Convers Manag* 2017;148:569–82. <https://doi.org/10.1016/j.enconman.2017.06.016>.
- [22] Wang F, Deng S, Zhao J, Wang J, Sun T, Yan J. Performance and economic assessments of integrating geothermal energy into coal-fired power plant with CO<sub>2</sub> capture. *Energy* 2017;119:278–87. <https://doi.org/10.1016/j.energy.2016.12.029>.
- [23] Lopez S, Hamm V, Le Brun M, Schaper L, Boissier F, Cotiche C, et al. 40 years of Dogger aquifer management in Ile-de-France, Paris Basin, France. *Geothermics* 2010;39:339–56. <https://doi.org/10.1016/j.geothermics.2010.09.005>.
- [24] Nador A, Kujbus A, Toth AN. Geothermal energy use, country update for Hungary. *Eur Geotherm Congr* 2016, Strasbourg, France; 2016.
- [25] Szanyi J, Kovács B. Utilization of geothermal systems in South-East Hungary. *Geothermics* 2010;39:357–64. <https://doi.org/10.1016/j.geothermics.2010.09.004>.
- [26] Bloemendal M, Jaxa-Rozen M, Olsthoorn T. Methods for planning of ATES systems. *Appl Energy* 2018;216:534–57. <https://doi.org/10.1016/j.apenergy.2018.02.068>.
- [27] Tureyen OI, Sarak H, Altun G, Satman A. A modeling analysis of unitized production: understanding sustainable management of single-phase geothermal resources

- with multiple lease owners. *Geothermics* 2015;55:159–70. <https://doi.org/10.1016/j.geothermics.2015.02.002>.
- [28] Bloemendal M, Olsthoorn T, Boons F. How to achieve optimal and sustainable use of the subsurface for Aquifer Thermal Energy Storage. *Energy Pol* 2014;66:104–14. <https://doi.org/10.1016/j.enpol.2013.11.034>.
- [29] van Beek F, Troost PJPM. The groningen gas field: a case history of the development of a giant gas field. *J Pet Technol* 1979;31:815–20. <https://doi.org/10.2118/7423-pa>.
- [30] Temizel C, Zhiyenkulov M, Ussenova K, Kazhym T, Canbaz CH, Saputelli LA. Optimization of well placement in waterfloods with optimal control theory under geological uncertainty. SPE annual technical conference and exhibition. Society of Petroleum Engineers; 2018.
- [31] Van Essen GM, Zandvliet MJ, Van den Hof PMJ, Bosgra OH, Jansen JD. Robust waterflood optimization of multiple geological scenarios. *SPE J* 2009;14:202–10. <https://doi.org/10.2118/102913-pa>.
- [32] TNO. NLOG; 2018. < [www.nlog.nl](http://www.nlog.nl) > [accessed February 2, 2018].
- [33] RVO. Risico's dekken voor Aardwarmte 2017:1–16.
- [34] NEA. < [www.nationaleenergieatlas.nl](http://www.nationaleenergieatlas.nl) > 2012. < <http://www.nationaleenergieatlas.nl/en> > [accessed February 28, 2018].
- [35] Kramers L, Van Wees JDAM, Pluymaekers MPD, Kronimus A, Boxem T. Direct heat resource assessment and subsurface information systems for geothermal aquifers; the Dutch perspective. *Netherlands J Geosci* 2012;91:637–49.
- [36] Eurostat. Supply, transformation and consumption of renewable energies – annual data 2016. [appsso.eurostat.ec.europa.eu](https://ec.europa.eu/eurostat) [accessed September 11, 2018].
- [37] Van Heekeren V, Bakema G. Geothermal energy use, country update for the Netherlands. *Eur Geotherm Congr* 2013;2013:6.
- [38] Devault B, Jeremiah JM. Nieuwerkerk Formation West Netherlands Basin 2002;10:1679–707.
- [39] Donselaar ME, Groenenberg RM, Gilding DT. Reservoir geology and geothermal potential of the Delft Sandstone Member in the West Netherlands Basin. *World Geotherm Congr* 2015, Melbourne; 2015, p. 9.
- [40] Willems CJL, Vondrak AG, Munsterman DK, Donselaar ME, Mijnlief HF. Regional geothermal aquifer architecture of the fluvial Lower Cretaceous Nieuwerkerk Formation – a palynological analysis. *Netherlands J Geosci* 2017;96:319–30. <https://doi.org/10.1017/njg.2017.23>.
- [41] Provincie Zuid-Holland. Investeringsstrategie Warmteparticipatiefonds. Den Haag; 2017.
- [42] Feliks MEJ, McCay AT, Roberts J. Life cycle assessment of the carbon intensity of deep geothermal heat systems: a case study from Scotland. *Sci Total Environ* 2019. [in press].
- [43] Pluymaekers MPD, Doornenbal JC, Middelburg H. Velmod-3.1. Utrecht; 2017.
- [44] Pluymaekers MPD, Kramers L, Van Wees JDAM, Kronimus A, Nelskamp S. Reservoir characterisation of aquifers for direct heat production: methodology and screening of the potential reservoirs for the Netherlands. *Netherlands J Geosci* 2012;91:621–36.
- [45] Willems CJL, Nick HM, Weltje GJ, Bruhn DF. An evaluation of interferences in heat production from low enthalpy geothermal doublets systems. *Energy* 2017;135:500–12. <https://doi.org/10.1016/j.energy.2017.06.129>.
- [46] Duin EJT, Doornenbal JC, Rijkers RHB, Verbeek JW, Wong TE. Subsurface structure of the Netherlands – results of recent onshore and offshore mapping. *Netherlands J Geosci* 2006;85:245–76.
- [47] Bruhn DF, Wolf K, Woning M, Dalen E Van, Nick HM, Willems CJL, et al. The Delft Aardwarmte Project (DAP): providing renewable heat for the university campus and a research base for the geothermal community. *World Geotherm. Congr.* 2015, Melbourne, Australia; 2015.
- [48] Diersch HJG. FEFLOW – finite element subsurface flow & transport simulation system, reference manual; 2005.
- [49] Mercer JW, Pinder GF. *Finite element analysis of hydrothermal systems*. Univ Alabama Press; 1974.
- [50] Saeid S, Al-Khoury R, Nick HM, Barends F. Experimental-numerical study of heat flow in deep low-enthalpy geothermal conditions. *Renew Energy* 2014. <https://doi.org/10.1016/j.renene.2013.08.037>.
- [51] Saeid S, Al-Khoury R, Nick HM, Hicks MA. A prototype design model for deep low-enthalpy hydrothermal systems. *Renew Energy* 2015. <https://doi.org/10.1016/j.renene.2014.12.018>.
- [52] Willems CJL, Nick HM, Donselaar ME, Weltje GJ, Bruhn DF. On the connectivity anisotropy in fluvial Hot Sedimentary Aquifers and its influence on geothermal doublet performance. *Geothermics* 2017;65:222–33. <https://doi.org/10.1016/j.geothermics.2016.10.002>.
- [53] Mijnlief H, Ramsak P, Lako P, Smeets J, Veldkamp H. Geothermal energy and support schemes in The Netherlands. *Eur Geotherm Congr* 2013:1–8.
- [54] Energieonderzoek Centrum Nederland (ECN). Eindadvies basisbedragen SDE+ 2018. Amsterdam; 2017.
- [55] Van Wees JDAM, Kramers L, Kronimus RA, Pluymaekers MPD, Mijnlief HF, Vis GJ. ThermoGISTM V1.0 Part II: methodology. TNO Rep; 2010.
- [56] Daniilidis A, Alpsyoy B, Herber R. Impact of technical and economic uncertainties on the economic performance of a deep geothermal heat system. *Renew Energy* 2017;114:805–16. <https://doi.org/10.1016/j.renene.2017.07.090>.
- [57] Beckers KF, Lukawski MZ, Anderson BJ, Moore MC, Tester JW. Levelized costs of electricity and direct-use heat from Enhanced Geothermal Systems. *J Renew Sustain Energy* 2014;6:013141. <https://doi.org/10.1063/1.4865575>.
- [58] Poulsen SE, Balling N, Nielsen SB. A parametric study of the thermal recharge of low enthalpy geothermal reservoirs. *Geothermics* 2015;53:464–78. <https://doi.org/10.1016/j.geothermics.2014.08.003>.
- [59] Platform Geothermie. Platform Geothermie; 2018. < <https://geothermie.nl/> > [accessed March 30, 2018].
- [60] Van Wees JDAM, Degens G, Zijp M, De boer J, Odbam A, Eyvazi FJ. TNO BIA geothermal report: the causes and solutions to poor well performance in Dutch geothermal projects; 2012.
- [61] Willems CJL, Nick HM, Goense T, Bruhn DF. The impact of reduction of doublet well spacing on the Net Present Value and the life time of fluvial Hot Sedimentary Aquifer doublets. *Geothermics* 2017;68:54–66. <https://doi.org/10.1016/j.geothermics.2017.02.008>.
- [62] Weijermars R, Van Harmelen A. Breakdown of doublet recirculation and direct line drives by far-field flow in reservoirs: implications for geothermal and hydrocarbon well placement. *Geophys J Int* 2016;19–47. <https://doi.org/10.1093/gji/ggw135>.
- [63] Lund JW, Boyd TL. Direct utilization of geothermal energy 2015 worldwide review. *Geothermics* 2016;60:66–93. <https://doi.org/10.1016/j.geothermics.2015.11.004>.
- [64] Genter A, Fritsch D, Cuenot N, Baumgartner J, Graff JJ. Overview of the current activities of the European EGS Soutz project: from exploration to electricity production. Thirty-fourth work. *Geotherm Reserv Eng, Stanford, California*; 2009. doi: 10.1159/000337025.
- [65] Hørsholt S, Nick HM, Jørgensen JB. Oil production optimization of black-oil models by integration of matlab and eclipse E300. *IFAC-PapersOnLine* 2018;51:88–93. <https://doi.org/10.1016/j.ifacol.2018.06.360>.
- [66] Kahrobaei S, Fonseca RM, Willems CJL, Wilschut F, Van Wees JDAM. Regional scale geothermal field development optimization under geological uncertainties. *Eur Geotherm Congr* 2019 Den, Den Haag; 2019. p. 11–4.
- [67] Salimzadeh S, Nick HM, Zimmerman RW. Thermoporoelectric effects during heat extraction from low-permeability reservoirs. *Energy* 2018;142:546–58. <https://doi.org/10.1016/j.energy.2017.10.059>.
- [68] Bechberger M, Reiche D. Renewable energy policy in Germany: pioneering and exemplary regulations 2004;VIII:25–35.
- [69] Blom MJ, Aarnink SJ, Roos J, Braber K. MKBA Warmte Zuid-Holland. Delft, Netherlands; 2014.
- [70] Weijermars R, Luthi SM. Dutch natural gas strategy: historic perspective and challenges ahead. *Geol En Mijnbouw/Netherlands J Geosci* 2011;90:3–14. <https://doi.org/10.1017/S0016774600000627>.
- [71] Mijnbouwwet 2018. < <https://wetten.overheid.nl/BWBR0014168/2018-11-08> > [accessed November 8, 2018].



# Performance of low-enthalpy geothermal systems: Interplay of spatially correlated heterogeneity and well-doublet spacings

Masoud Babaei<sup>a,\*</sup>, Hamidreza M. Nick<sup>b,c</sup>

<sup>a</sup> The University of Manchester, School of Chemical Engineering and Analytical Science, Manchester, UK

<sup>b</sup> The Danish Hydrocarbon Research and Technology Centre, Technical University of Denmark, Lyngby, Denmark

<sup>c</sup> Department of Geoscience & Engineering, Delft University of Technology, Delft, Netherlands

## HIGHLIGHTS

- 2600 computationally intensive simulations for geothermal doublet systems conducted.
- Discharge, well/doublet spacing, poro-perm correlation lengths and variance varied.
- A doublet spacing equal to well spacing produced consistently best performance.
- Anisotropic heterogeneity led to shorter/longer lifetime for short/long spacing.
- Sufficient lifetime for shorter well spacing than the ones conventionally designed.

## ARTICLE INFO

### Keywords:

Low-enthalpy geothermal systems  
Well spacing  
Doublet spacing  
Heterogeneity  
Geothermal license area  
Performance indicators

## ABSTRACT

The low-enthalpy geothermal systems are commonly deployed in sedimentary geological settings that feature significant levels of deposition-induced heterogeneity. In this paper, realistic levels of heterogeneity in the form of varying porosity variance and spatial correlation lengths are considered for a 3D geothermal system. Using 2600 computationally intensive numerical simulations of two doublets placed in a checkboard pattern, the influence of well and doublet spacings on performance metrics of low-enthalpy geothermal systems are investigated. The simulations strongly support that in varying heterogeneous systems, the lifetimes of operation are shorter, and depending on isotropicity or anisotropicity of correlated heterogeneity, the lifetimes vary. Most notably the anisotropically correlated heterogeneity can lead to either positive impact (by diverting the cold water plume) or negative impact (by facilitating an early breakthrough of cold water plume) on the lifetime of the operation compared to isotropically correlated heterogeneity. We also calculate the boundary of the region around the wells designated as the “license area” (where the cold water front reaches to or where a threshold temperature drop of 1 °C occurs). By doing so, it is found that the operator can assume larger extents (of up to 50%) for the license areas of the aquifer than the ones conventionally assumed. To minimize the impact of heterogeneity on operation, the best practice was found to place the doublets in the same spacings as of the wells. Moreover, it is found that the well distance can be significantly shorter than what is commonly realised for heterogeneous geothermal aquifers.

## 1. Introduction

Many of the low-enthalpy deep geothermal systems are deployed in sedimentary reservoirs at depths between 2 and 2.5 km with a temperature between 70 and 90 °C [1]. The most common method of geothermal energy recovery from low-enthalpy aquifers are doublet systems that utilize two wells, one for hot water production and another for cold water injection. The lifetime of the doublet (how long the

doublet can produce economically), energy sweep (produced energy compared to the total amount of available energy) and energy production rate of doublets determine the performance of doublet systems. The accuracy of predictive simulation tools is essential for the successful design of doublet systems.

The sedimentary reservoirs are characterised by their lithographical, geological, structural and thermal properties. These characteristics govern the geothermal performance indicators. Various

\* Corresponding author.

E-mail address: [masoud.babaei@manchester.ac.uk](mailto:masoud.babaei@manchester.ac.uk) (M. Babaei).

<https://doi.org/10.1016/j.apenergy.2019.113569>

Received 17 January 2019; Received in revised form 6 July 2019; Accepted 15 July 2019

0306-2619/ © 2019 Elsevier Ltd. All rights reserved.

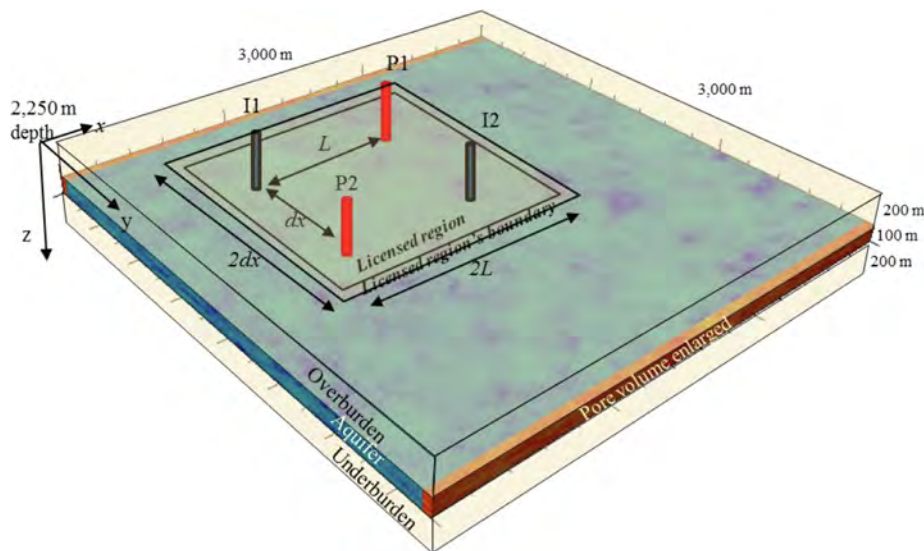


Fig. 1. The doublets configuration and the license-boundary control region of the subsurface system used in this study.

studies have focused on influence of some of the above-mentioned characteristics on doublet performances. For example, Poulsen et al. [2] investigated the impact of thermal conductivity. Several authors focused on brine viscosity and density dependence on temperature, e.g., Ma & Zheng [3] found that mean discrepancy between the simulated temperature distributions with and without considering the effects of variable density and viscosity is approximately 2.5%. Using a numerical study on density and viscosity variations with temperature, Saeid et al. [4] found that ignoring the variations leads to overestimation of the geothermal system lifetime in hot injection scenarios, and underestimation of the system lifetime in cold injection scenarios. Mottaghy et al. [5] showed that thermal and hydrogeological data are crucial to planning geothermal resource development, and numerical codes should take temperature dependence of thermal properties into account. Vogt et al. [6] demonstrated the importance of accounting for heterogeneity of rock parameters resulting in significant variations of production temperature and well pressure with time.

Several authors including [7–10] studied impacts of well spacing. Saeid et al. [7] showed that the lifetime increases linearly with the well spacing for homogeneous aquifers with no geological complexity or barriers. Willems et al. [8], also for homogeneous aquifers only, optimized well spacing so that the interference between the aquifers are minimized. Pandey & Vishal [9] showed that, for homogeneous aquifers again, at higher well spacing, the flow length/volume increased and so did the pumping power, leading to improved overall performance in heat extraction. Willems et al. [10], for homogeneous aquifers, evaluated both the possible financial advantage of well spacing reduction and its impact on doublet life time.

A recent review of Pandey et al. [11] on geothermal reservoirs coupled thermo-hydro-mechanical-chemical approaches shows that the impact of aquifer heterogeneity on performance of doublets is less studied. The presence of spatial heterogeneity inside a reservoir may induce flow channeling and reduce the volume of reservoir participating in flow fields [11]. Most of the studies on performance of low enthalpy systems, as referred above, have considered homogeneous systems or simple lithographical variations. There are only few existing research works that specifically deal with heterogeneity for geothermal doublet systems [12,6,13–16]. Watanabe et al. [12] found that the most significant factors in the analysis of thermo-hydro-mechanical coupled processes in heterogeneous porous media are permeability and heat capacity. Vogt et al. [6] studied the transient temperature and pressure at the production well for 400 sets of heterogeneous realizations of the fault zone in a doublet system. The authors concluded that the

distribution of porosity/permeability and thermal conductivity inside the fault zone significantly impact heat extraction rate from the reservoir. Crooijmans et al. [13] studied the impact of heterogeneity in a fluvial system for a single doublet and they have suggested a correlation for the lifetime as a function of production rate and net-to-gross values. The authors showed that at lower net-to-gross ratio the temperature drop at the production well was slower than the higher net-to-gross ratio for all sets of the heterogeneous reservoirs. Willems et al. [14] studied the impact of heterogeneity on the connectivity in geothermal systems. The authors found that the impact of heterogeneity is significant on heat production and pumping loss was less if the wells were placed parallel to the paleo flow direction. Niederau et al. [15] studied the effect of spatially heterogeneous permeability on the formation and shape of hydrothermal porous flow in the Yarragadee aquifer, Australia. Their results showed the spatially heterogeneous permeability can affect the local convection patterns. Very recently, Liu et al. [16], showed that for a doublet system with increasing correlation length, the possibility of flow channels appearing in well pair system increases, causing a short average thermal breakthrough time and a lower surface settlement around the injection well.

For heterogeneous aquifers, attention has been also mostly paid to geothermal doublet systems with fracture networks. Performance of deep geothermal doublets in fractured reservoirs have been studied either for a single fracture [17], parallel fractures [18] or complex fracture networks [19–21]. Salimzadeh et al. [20] showed that both heat production and required pump energy is very sensitive to fracture spacing, density and connectivity. Pandey & Chaudhuri [22] studied the impact of fracture aperture heterogeneity on geothermal heat recovery in fractured aquifers and found that small correlation lengths in fracture sets do not create much variation in temperature at production well while [23] illustrated the aperture variation induced by thermal or chemical stresses can significantly influence the performance of the geothermal system. Vasilyeva et al. [19] developed multiscale model of heat and flow transport in EGS systems with varying degree of fracturisation. No systematic works, however, have been carried out on geothermal doublet systems to delineate the impact of heterogeneity on well or doublet spacing.

An important design factor for geothermal doublets is the required distance between wells in a doublet system as well as the distance between the multiple doublets. There are research studies dealing with the optimisation of low-enthalpy doublets [24,25]. Chen et al. [24] coupled a complex hydrothermal simulation model and a multivariate adaptive regression spline-based surrogate model to investigate the

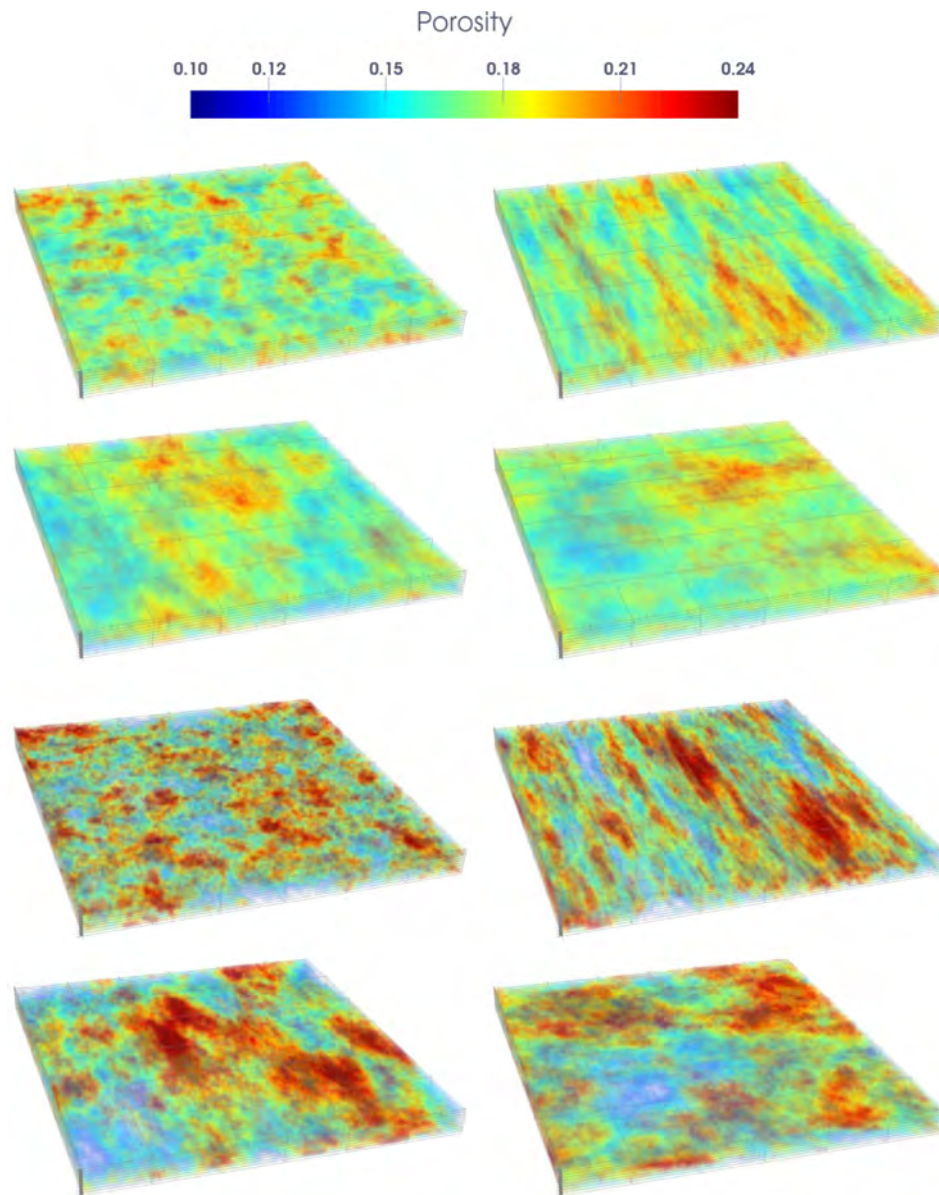


Fig. 2. The porosity fields (mD) fields for four correlation lengths times two variances. The first four fields are for  $\sigma^2 = 0.02$  (C1, C2, C3 and C4) and the second four fields are for  $\sigma^2 = 0.04$  (C1, C2, C3 and C4).

effects of geological uncertainties (fault size and geological unit permeability) on optimal well placement and control (re-injection well location, production rate) in a geothermal prospect near Superstition Mountain in Southern California, USA. The model used was homogeneous, so that in each case a constant permeability was chosen in the range of  $-13.8 < \log(\text{perm}) [\text{m}^2] < -13.3$ . The authors found the optimal production rate is 30.7 kg/s and distance between production and injection well is 473 m in order to maximize the net profit after 50 years of potential geothermal extraction. Kong et al. [25] used numerical modelling, economic analysis and a homogeneous domain of a synthetic aquifer and obtained an optimal well placement of 400 m.

There are no existing work specifically focusing on well/doublet spacing for heterogeneous geothermal systems. The area of research is important because administering a sub-optimal well/doublet spacing can potentially lead to negative interferences that, in turn, may influence the utilisation efficiency of wells and doublet systems. An accurate modelling-based design that provides optimal solutions will prevent such interferences. Currently, thermal breakthrough which is the moment when the extent of re-injected cold water plume reaches the

production wells is the basis to determine production lifetimes as an indicator for the temperature drop at the license boundary. However, the license areas temperature may not immediately drop to non-economic values when thermal breakthrough occurs at production wells. As a result, thermal energy is still available in economic levels and heat production could continue after thermal breakthrough as long as the average temperature at the license boundary has not experienced notable temperature drop (i.e.  $>1^\circ\text{C}$ ). The temperature drop over the license area's boundary can instead be used to determine the lifetime of the geothermal doublet systems. This can be obtained utilising accurate and realistic production simulations. The temperature distribution and shape of cold water front are strongly controlled by underlying heterogeneities in the geological properties of geothermal aquifers.

To address above-mentioned knowledge gap in the design of geothermal system, in this study, we address the following questions.

1. How does well spacing or doublet spacing under different levels of heterogeneity impact performance of the geothermal system? The performance criteria include lifetime of the operation, energy or

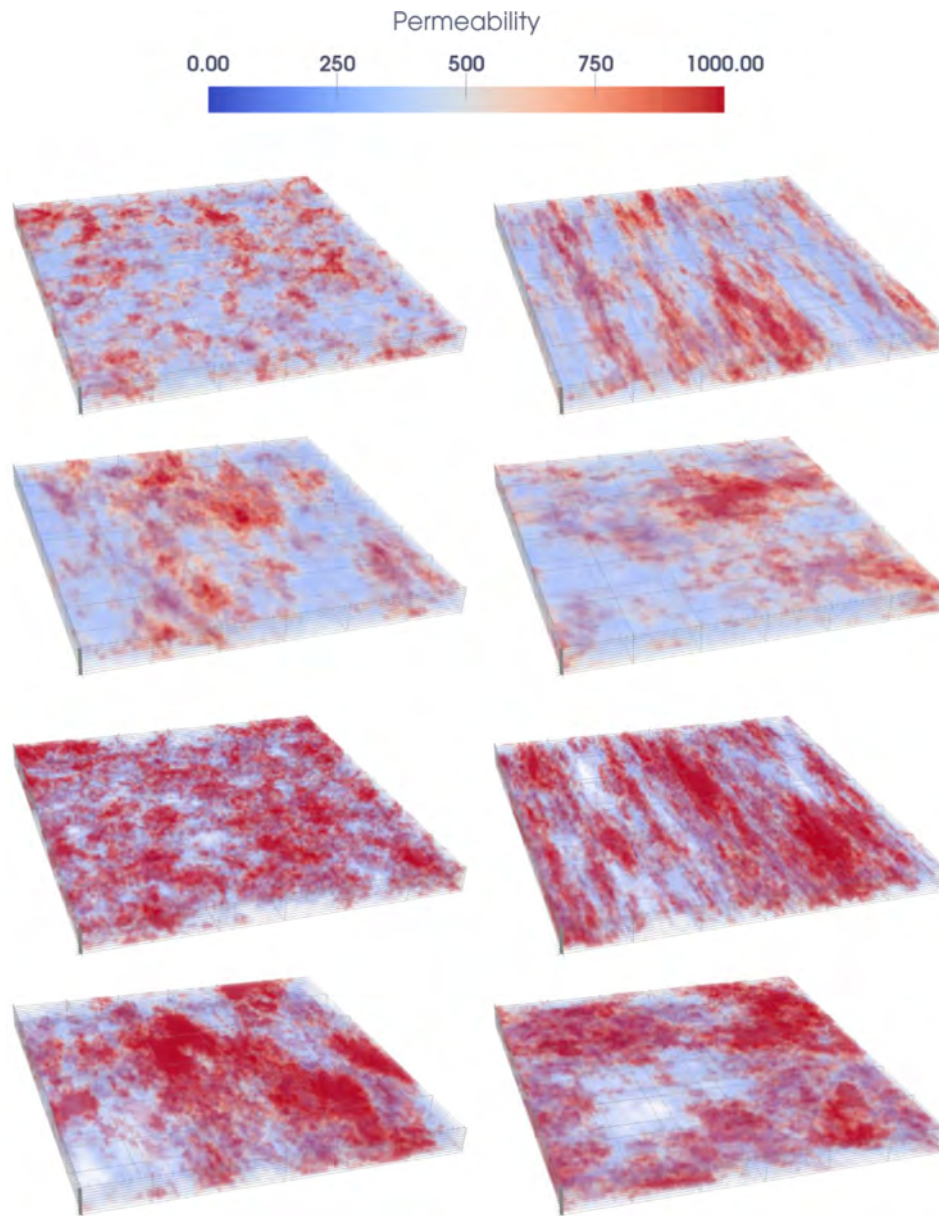


Fig. 3. The permeability fields (mD) fields for four correlation lengths times two variances. The first four fields are for  $\sigma^2 = 0.02$  (C1, C2, C3 and C4) and the second four fields are for  $\sigma^2 = 0.04$  (C1, C2, C3 and C4).

Table 1

A summary of simulation varying parameters considered for heterogeneous simulations (total number of simulations are  $2 \times 2 \times 4 \times 5 \times 4 \times 8 = 2,560$ ).

Parameter	Variance of porosity fields ( $\sigma^2$ )	Injection rate (Q)	Well spacing (L)	doublet spacing (dx/L)	Correlation lengths ( $c_x$ and $c_y$ )	Realizations ( $\ell$ )
Magnitudes	0.02 and 0.04	150 m <sup>3</sup> /h and 250 m <sup>3</sup> /h	500 m, 700 m, 900 m, and 1100 m	0.7, 0.85, 1, 1.15 and 1.3	100 m and 500 m varied directionally	
Notations	v1 and v2	Q1 and Q2			C1, C2, C3 and C4	
Number of cases	2	2	4	5	4	8

thermal sweep efficiency, energy production, and coefficients of performance.

2. What is the correlation between temperature drop in the production wells and that of license boundary?
3. How significant is the impact of heterogeneity on well spacing design?

To address these questions, we use a numerical simulation tool

described in Section 2 alongside the geological properties, heterogeneous property generation, heat recovery scenarios as functions of well or doublet spacing and definition of performance metrics. The results and discussions are presented in Section 3 and the paper is concluded in Section 4.

By answering the above-mentioned research questions, we provide a novel unprecedented understanding of interplay between “realistically-represented fluvial aquifer heterogeneity and geothermal doublet

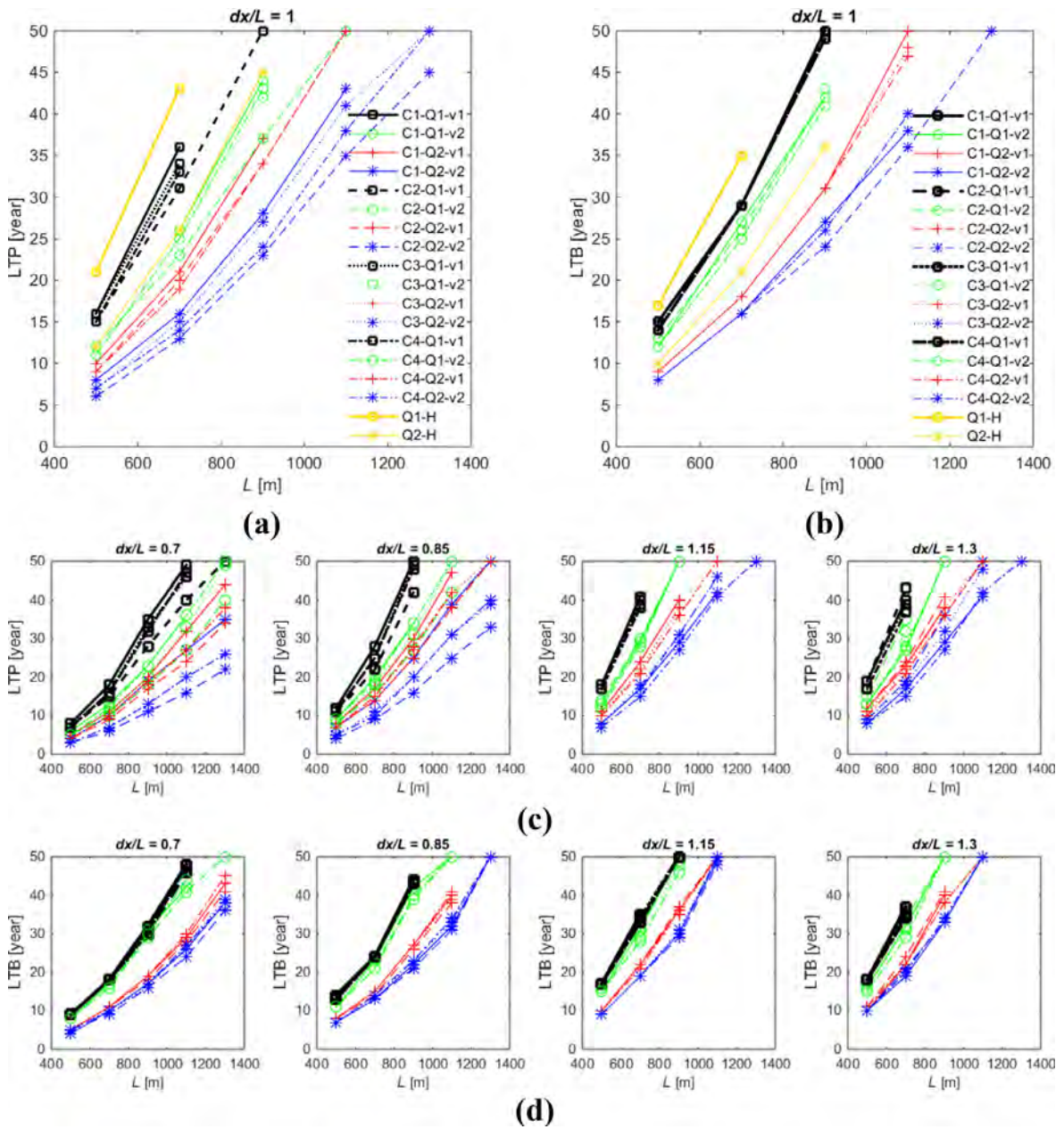


Fig. 4. Comparison between (a) lifetimes calculated from production wells (LTP) for  $dx/L = 1$ , (b) lifetimes calculated from license area's boundary (LTB) for  $dx/L = 1$ , (c) lifetimes calculated from production wells (LTP) for other  $dx/L$  values, and (d) lifetimes calculated from license area's boundary (LTB) for other  $dx/L$  values.

design". This is of direct relevance to subsurface energy application and geothermal heat recovery.

## 2. Methodology

The numerical simulations are carried out by ECLIPSE E300 simulator [26]. Previously for geothermal heat recovery simulations (including low-enthalpy doublets or deep enhanced geothermal systems), the simulator have been successfully employed [27]. Here, a multi-parametric analysis is carried out on the simulation results to delineate the interplay of heterogeneity and well or doublet spacing. In the following, first we describe the methodology including a brief description of the governing equations for coupled heat transfer and flow in porous media, the geological model considered with heterogeneities of porosity and permeability fields, the simulation scenarios and the performance metrics.

### 2.1. Coupled heat transfer and flow in porous media

To simulate coupled heat transfer and flow in porous media, a fully implicit finite volume method utilising a two-point flux approximation scheme is employed. The flow and heat transfer solves a coupled problem integrating (i) the conservation equation for each fluid component (water) in each gridblock at each timestep (leading to the non-linear residual  $r_{fl}$ ), and (ii) the energy conservation equation in each gridblock at each timestep (leading to the non-linear residual  $r_e$ ):

$$r_{fl} = \frac{d}{dt}(V_p m) + F + Q = 0 \quad (1)$$

$$r_e = \frac{d}{dt}(V_b e) + F_e + C_e + Q_{HL} + Q_e = 0 \quad (2)$$

where  $m$  is the moles of fluid component (water) in each gridblock,  $V_p$  is the pore volume,  $F$  is the net flow rate into neighbouring grid blocks,  $Q$

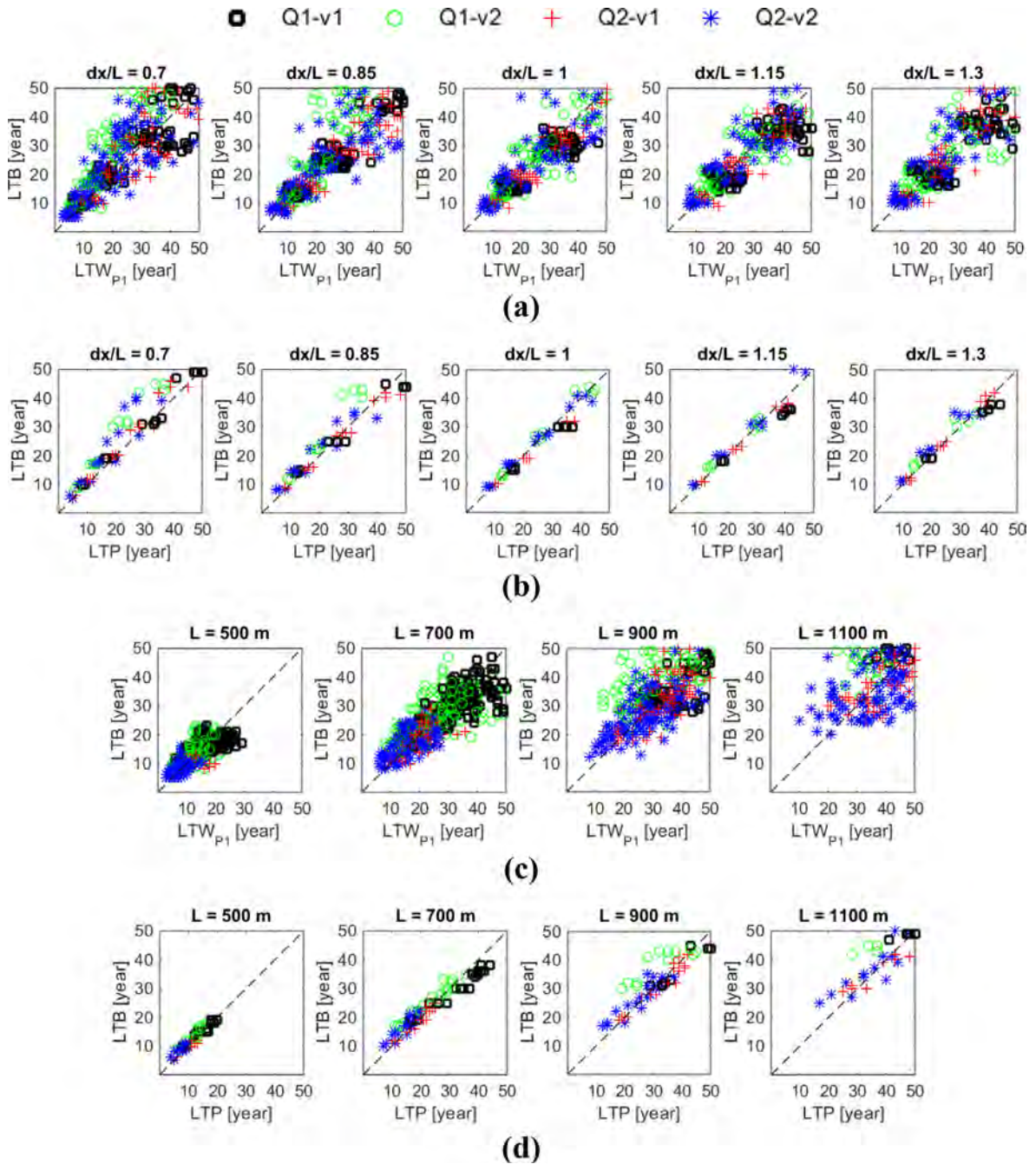


**Fig. 5.** The comparison between LTB and LTW from all realizations, and between LTP and LTB calculated from converged solutions: (a) LTB vs.  $LTW_{p1}$  per realization grouped for each  $dx/L$  ( $L$  varies in each plot), (b) LTB vs. LTP per realization grouped for each  $dx/L$  ( $L$  varies in each plot), (c) LTB vs.  $LTW_{p1}$  from converged solution grouped for each  $L$  ( $dx/L$  varies in each plot), and (d) LTB vs. LTP grouped from converged solution for each  $L$  ( $dx/L$  varies in each plot).

is the net flow rate into wells during the timestep,  $V_b$  is the bulk volume,  $e$  is the energy in gridblock that is  $e = (\rho C)_{eq}(T - T_{ref})$ , where  $(\rho C)_{eq} = \phi(\rho C)_w + (1 - \phi)(\rho C)_r$  in which  $\phi$  is the porosity of gridblock,  $\rho$  is density of water/rock and  $C$  is the specific heat capacity of water/rock. In Eq. (2),  $F_c$  is the convective enthalpy flow rate into neighbouring gridblocks,  $C_e$  is the conductive energy flow rate into neighbouring gridblocks,  $Q_{HL}$  is the conductive energy flow rate to the surrounding rocks (heat loss),  $Q_e$  is the net enthalpy flow rate into wells during the timestep [26]. The net flow of water from cell  $i$  into neighbouring cells is obtained by

$$F_{n,i} = \sum_n \Gamma_i \frac{b_w}{\mu_w} d\Phi_{ni} \quad (3)$$

where  $\Gamma_i$  is the transmissibility between cells  $n$  and  $i$  which is constructed using the harmonic mean of absolute permeability ( $K$ ) of cells  $n$  and  $i$ ,  $b_w$  is the molar density of water,  $\mu_w$  is the viscosity of water, and  $d\Phi_{ni}$  is the potential difference of water phase between cells  $n$  and  $i$ . The net flow rate of energy (convection) from cell  $i$  into neighbouring cells is obtained in a similar manner:

$$F_{e,i} = \sum_n \Gamma_i (\rho C)_w T \frac{b_w}{\mu_w} d\Phi_{ni} \quad (4)$$

The heat conduction term for cell  $i$  is given by summing conduction between all neighbouring cells  $n$  as [26]:

$$C_{ei} = - \sum_n \Gamma_{hi} (T_i - T_n) \quad (5)$$

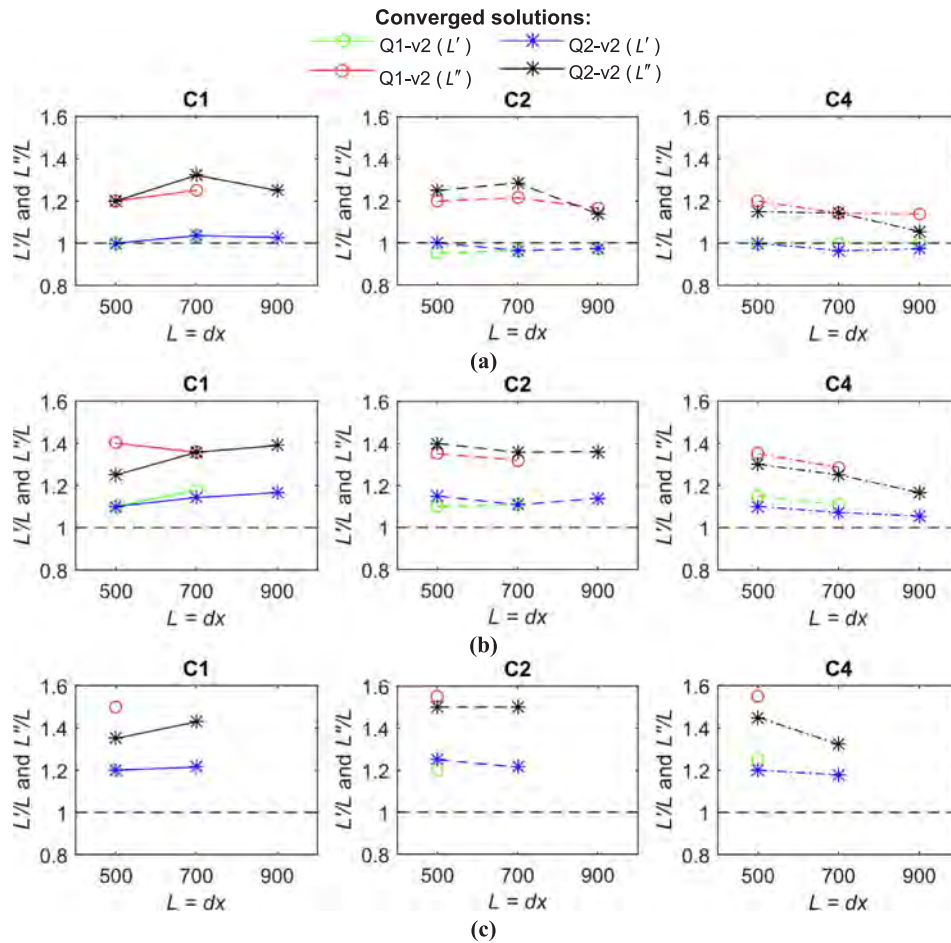


Fig. 6. (a)  $L'/L$  and  $L''/L$  vs.  $L$  for LTP1, (b) for LTP5 and (c) for LTP10. From left to right:  $L'/L$  and  $L''/L$  vs.  $L$  calculated from converged solutions of C1, of C2, and of C4.

where  $\Gamma_{hi}$  is the thermal conduction transmissibility between cells  $n$  and  $i$  constructed using the harmonic mean of the equivalent conductivity of cells  $n$  and  $i$ . The equivalent conductivity is  $\lambda_{eq} = \phi\lambda_w + (1 - \phi)\lambda_r$ , where  $\lambda_w$  is the water conductivity and  $\lambda_r$  is the rock conductivity.

In this study we have not included the heat transfer in the production and injection wells. This has been studied in detail by Saeid et al.[7] for two tubing materials for a discharge rate of 150 m<sup>3</sup>/h. They concluded that the heat gain and loss in the injection and production wells, respectively, after five days of operation are negligible.

## 2.2. Geological model and fluid properties

We assume a structurally simple, synthetic, 3D rectangle for the geological system under study with 3 km × 3 km × 500 m lengths in x, y and z directions (Fig. 1). The system comprises of an overburden (200 m thick), an aquifer (100 m thick) and an underburden (200 m thick). The system is discretized into laterally uniform 120 × 120 mesh (25 m × 25 m gridblocks). However, vertical discretization is non-uniform. The overburden and underburden are each discretized into one layer only with 200 m thickness. Whereas the aquifer is discretized into 10 layers (each layer 10 m thick). Therefore overall we have 12 layers and 172,800 gridblocks. The top face of the structure is 2250 m deep.<sup>1</sup>

The initial conditions are set as  $p_{init}$  (initial pressure) equals to 200 bar at the reference depth of 2500 m, and  $T_{init}$  (initial temperature)

equals 67.5 °C at 2250 m, 75 °C at 2500 and 82.5 °C at 2750 m. The boundary conditions are fully close to flow in x- and z-directions and fully open to flow in y-direction (the direction of anisotropic heterogeneity). In order to implement open boundaries, the pore volumes of the boundary blocks in y-direction are multiplied by 1,000. This method has been previously used to emulate open flow boundary conditions or infinite domains [28–30].

### Rock properties

Thermal conductivity of rock is 0.91 W/m/K, rock density is 2650 kg/m<sup>3</sup>, rock specific heat capacity is 2,000 J/kg/K and rock compressibility is  $4.93 \times 10^{-5} \text{ bar}^{-1}$  at 250 bar. In this study, we neglect the dependence of rock density and heat capacity on porosity as considered by Liu et al.[16]. Porosity of the overburden and underburden is set to 0.01, and permeability of the overburden and underburden is set to 0.001 mD. To generate porosity of the aquifer, a code available online [31] is used to generate correlated fields. The method utilizes the Fourier-transform of the covariance function as the power spectral density function of all realizations. Random autocorrelated fields are generated by creating random phase spectra meeting the conditions of real numbers in the physical domain. The realizations are then converted by back-transformation of the power- and phase-spectrum into the physical domain.

Correlated porosity fields are generated all with a mean of 0.17 and a variance of  $\sigma^2 = 0.02$  and 0.04, hereafter referred to as v1 and v2 for simplicity. The covariance matrices of porosity fields are assigned as exponential. Four different correlation lengths in lateral directions ( $c_x$  denotes correlation length in x-direction and  $c_y$  denotes correlation length in y-direction) are used in the process:

<sup>1</sup> Our preliminary modelling practices refining the mesh did not yield significant change in the results of a homogeneous and several heterogeneous examples we considered for mesh sensitivity analyses.

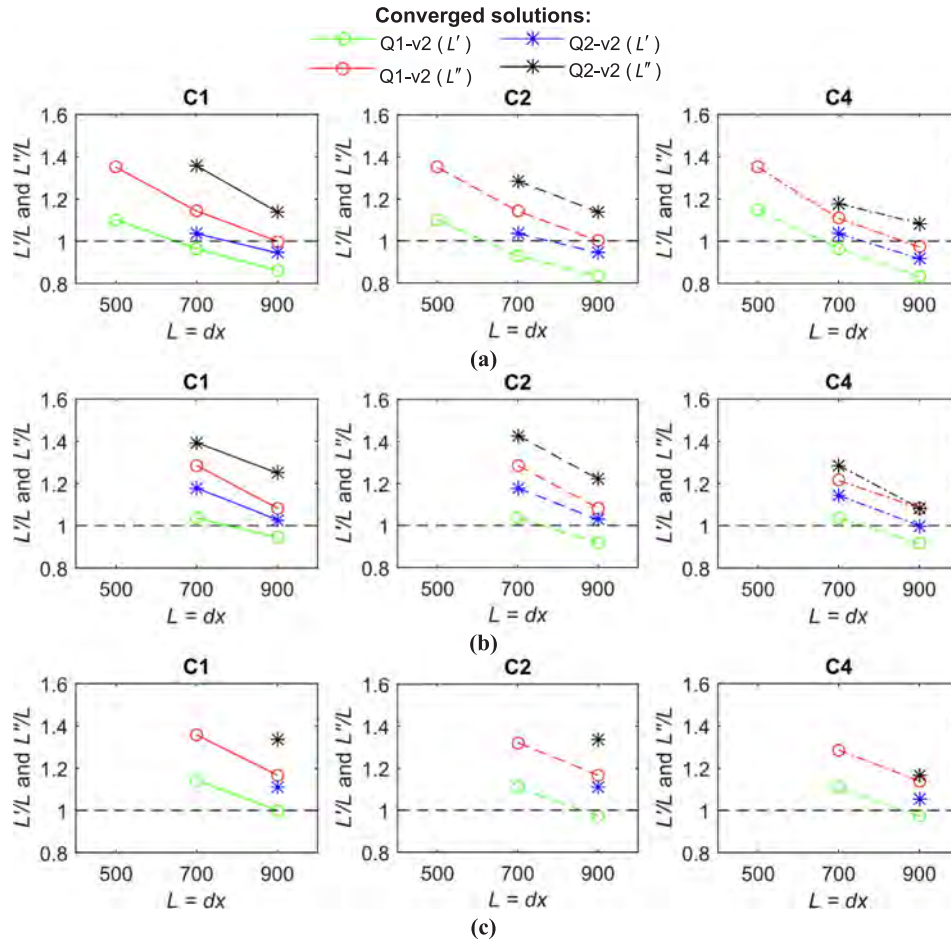


Fig. 7. (a)  $L'/L$  and  $L''/L$  vs.  $L$  for 20 year, (b) for 30 year and (c) for 40 year. From left to right:  $L'/L$  and  $L''/L$  vs.  $L$  calculated from converged solutions of C1, of C2, and of C4.

- $c_x = 100$  m and  $c_y = 100$  m hereafter referred to as C1
- $c_x = 100$  m and  $c_y = 500$  m hereafter referred to as C2
- $c_x = 250$  m and  $c_y = 500$  m hereafter referred to as C3
- $c_x = 500$  m and  $c_y = 500$  m hereafter referred to as C4

where  $c_x = 100$  m means 4 gridblocks are correlated in x-direction. As such we generate eight fields (2 variances multiplied by 4 different correlation lengths). Eight realizations are generated for each field, totalling 64 porosity fields. Next, the permeability fields are derived from porosities through the following relationship for the fluvial Delft Sandstone aquifers in the Netherlands [32]:

$$K = -2.03 \times 10^{-7} \phi^5 + 2.55 \times 10^{-5} \phi^4 - 1.04 \times 10^{-3} \phi^3 + 8.91 \times 10^{-3} \phi^2 + 3.58 \times 10^{-1} \phi - 3.21 \times \phi^0 \quad (6)$$

Figs. 2 and 3 show the profiles of porosity and permeability for one realization of each 8 pairs of correlation length and variance used to generate porosity and permeability fields, respectively.

*Fluid (water) properties*

Water thermal conductivity is set to 0.59 W/m/K, water specific heat is 4200 J/kg/K, water viscosity is written as a function of temperature according to IAPWS [33], and water density is input as a function of pressure and temperature through:

$$\rho_w(p, T) = \frac{\rho_w(p_{ref})}{(1 - c_w(p - p_{ref})) (1 + c_{T1}(T - T_{ref}) + c_{T2}(T - T_{ref})^2)} \quad (7)$$

where  $T_{ref}$  is the reference temperature which is 293.15 K,  $p_{ref}$  is the reference pressure which is 200 bar,  $c_{T1}$  is a coefficient which is set to  $3.0 \times 10^{-4} \text{ K}^{-1}$ ,  $c_{T2}$  is a coefficient which is set to  $3.0 \times 10^{-6} \text{ K}^{-2}$ ,  $\rho_w(p_{ref})$

is the water density at reference pressure and is set to  $1000 \text{ kg/m}^3$ , and  $c_w$  is water compressibility and is set to  $4.0 \times 10^{-5} \text{ bar}^{-1}$ .

*2.3. Heat recovery scenarios*

The geothermal heat recovery operation is carried out by two doublets using a checkboard pattern [8]. The injection wells are hereafter referred to as I1 and I2, and the production wells are referred to as P1 and P2 (see Fig. 1). The distance between the injection and production wells in each doublet is  $L$ , and the distance between the two doublets is  $dx$ . The position of I1 is fixed for all of the heat recovery scenarios and it is at  $x = 750$  m and  $y = 750$  m. However, the positions of I2, P1 and P2 change with different  $L$  and  $dx$  values. We assign four values for well spacing,  $L = 500$  m,  $700$  m,  $900$  m, and  $1100$  m. For each  $L$ , five doublet spacing,  $dx$ , are considered:  $dx = 0.7L$ ,  $dx = 0.85L$ ,  $dx = L$ ,  $dx = 1.15L$  and  $dx = 1.3L$ .

Cold water is injected using two well injection rates of  $Q = 150 \text{ m}^3/\text{h}$  and  $250 \text{ m}^3/\text{h}$ , hereafter referred to as Q1 and Q2 for simplicity. The injection rates are selected based on the actual production rates applied for the deep geothermal doublets in sedimentary aquifers [34]. The maximum allowable pressure at each well is 260 bar to avoid inducing hydraulic fractures. Above this threshold, the injection rate is decreased and as a result the production rate is also decreased to equate with the total injection rate. However, assuming that for each well stimulation operations have been carried out, porosity and permeability of connection blocks at perforation depths are increased so that they are equal to the average of porosity and permeability of the perforation column. By means of this, the injection and production rates are maintained

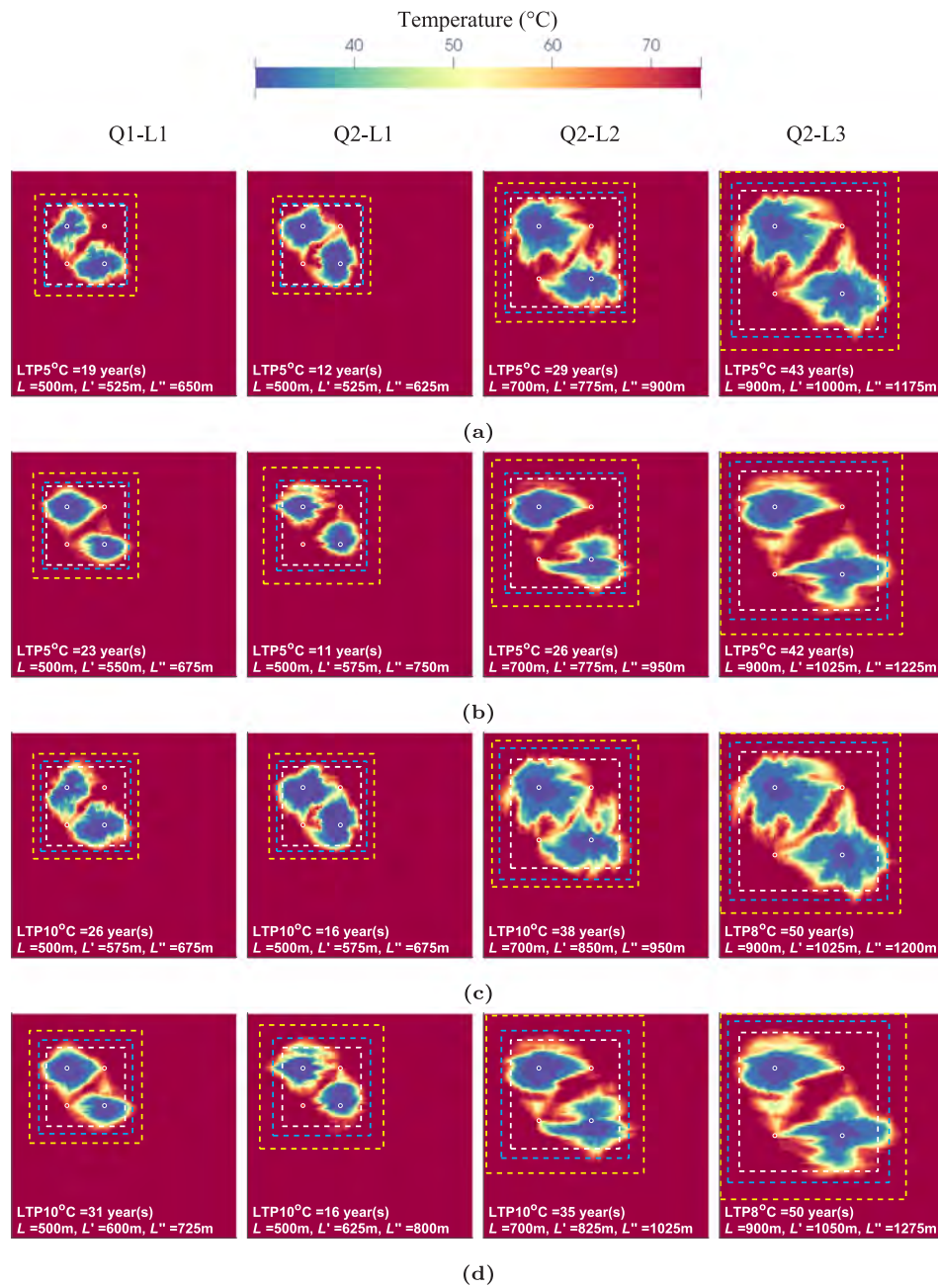


Fig. 8. Positions of  $L'$  and  $L''$  for selected examples of  $L = dx$  for the realization 1 and for (a) C1, LTP5, (b) C2, LTP5, (c) C1, LTPn and (d) C2, LTPn, where n is 10 °C if within 50 years ( $T_p'$ ) experiences 10 °C drop, otherwise n is the temperature drop of ( $T_p'$ ) at the end of simulation (50 years). From left column to right column in all rows: Q1 and  $L = dx = 500$  m, Q2 and  $L = dx = 500$  m, Q2 and  $L = dx = 700$  m, and Q2 and  $L = dx = 900$  m. In all subfigures, white, cyan and yellow dashed lines represent the  $2L \times 2dx$  extent,  $L'$  extent and  $L''$  extent, respectively.

throughout the simulation time for all the simulations in this study.

The temperature of injected water is 30 °C. The operation is continued for 50 years. A robust set of timestepping criteria is employed by the simulator to ensure convergence. The detailed presentation of the timestepping strategy in thermal mode of the simulator is prohibitive to describe here and can be found in ECLIPSE Technical Description manual [26] under Thermal Features/Timestepping Criteria. Using this strategy and checking the production profiles for highest injection rate and most heterogeneous porosity/permeability, we checked that there are no significant convergence issues in our simulations.

Using 64 models of porosity and permeability fields, overall we conduct 2,560 simulations: 2 variances multiplied by 4 correlation lengths multiplied by 8 realizations for each pair of variance-correlation length multiplied by 4  $L$  values multiplied by 5  $dx$  values, multiplied by

2 injection rates. These parameters are summarised in Table 1. Each simulation in average takes 3,800 s to complete using a Windows Server 2012-operated HP ProLiant server with two Intel Xeon E5-2690 12-core 2.60 GHz CPU processors. A parallel code is developed in MATLAB to call 8 simulations at the same time. This parallelisation saves run time significantly. In order to make comparisons of heterogeneous systems with homogeneous systems, additional simulations are carried out with constant aquifer porosity and permeability of  $\phi = 0.17$  and  $K = 360.2045$  mD (from Eq. 6). Using these homogeneous values, Q1 and Q2,  $L = 500$  m, 700 m, 900 m, and 1100 m, and  $dx = 0.85L$ ,  $dx = L$ ,  $dx = 1.15L$  and  $dx = 1.3L$ ,  $2 \times 4 \times 5 = 40$  additional simulations are conducted. Therefore in total 2,600 simulations are conducted in this work.

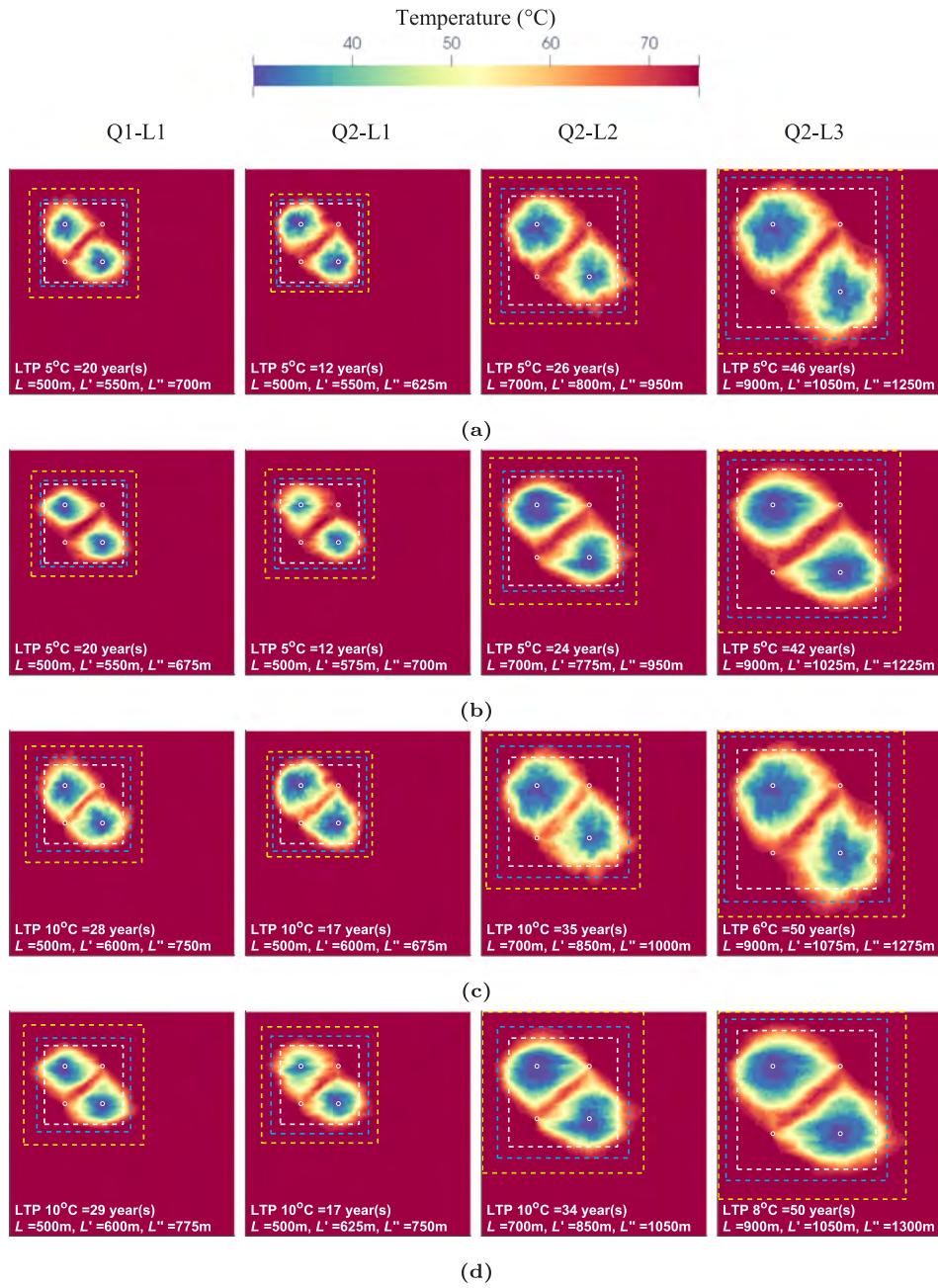


Fig. 9. Positions of  $L'$  and  $L''$  for selected examples of  $L = dx$  for the converged solution and for (a) C1, LTP5, (b) C2, LTP5, (c) C1, LTPn and (d) C2, LTPn, where  $n$  is  $10^\circ\text{C}$  if within 50 years ( $T_p^i$ ) experiences  $10^\circ\text{C}$  drop, otherwise  $n$  is the temperature drop of ( $T_p^i$ ) at the end of simulation (50 years). From left column to right column in all rows: Q1 and  $L = dx = 500$  m, Q2 and  $L = dx = 500$  m, Q2 and  $L = dx = 700$  m, and Q2 and  $L = dx = 900$  m. In all subfigures, white, cyan and yellow dashed lines represent the  $2L \times 2dx$  extent,  $L'$  extent and  $L''$  extent, respectively.

#### 2.4. Definition of performance metrics

In order to investigate the interplay of well or doublet spacing and heterogeneity of the system, first the following parameters are defined:

1. *Licensed regions boundary*: this is the shell-like lateral inner boundary blocks of the license area. The license area is taken as the  $2L \times 2dx \times 10$ -layer rectangle around the wells as shown in Fig. 1.
2. *Average temperature of production wells* defined by

$$\langle T_W^i \rangle = \frac{\int_{k=1}^{10} q_{W,k}^{prd,t} T_{ijk}^i}{\int_{k=1}^{10} q_{W,k}^{prd,t}} \quad (8)$$

where  $q_{W,k}^{prd,t}$  is the water production rate at connection (layer)  $k$  of

well  $W$ , at time  $t$ , and  $T_{ijk}^i$  is the block  $ijk$  temperature at time  $t$ . For each production well, obviously  $ij$  are fixed and only  $k$  changes from 1 to 10 (uppermost layer of the aquifer to lowermost layer). The denominator of above equation is equal to  $Q_{prd,W}$  which is a constant.

3. *Converged solution* for a variable  $\alpha$  over  $\ell$  realizations is defined as  $\alpha_\ell = (\sum_{i=1}^{\ell} \alpha_i) / \ell$ . By looking into the plot of  $\alpha_\ell$  vs.  $\ell$ , the convergence of realizations can be assessed, that is,  $\alpha_\ell$  should converge for a particular  $\ell$  so that for  $i > \ell$ ,  $\alpha_\ell$  remains constant. Based on our simulations, the converged solution for  $\langle T_W^i \rangle$  is obtained through 6 realizations, proving that 8 realizations are sufficient for convergence.
4. *Life time based on production wells*:  $LTW_{p1}$  and  $LTW_{p2}$  of geothermal heat recovery operation defined as the time (in years) when average

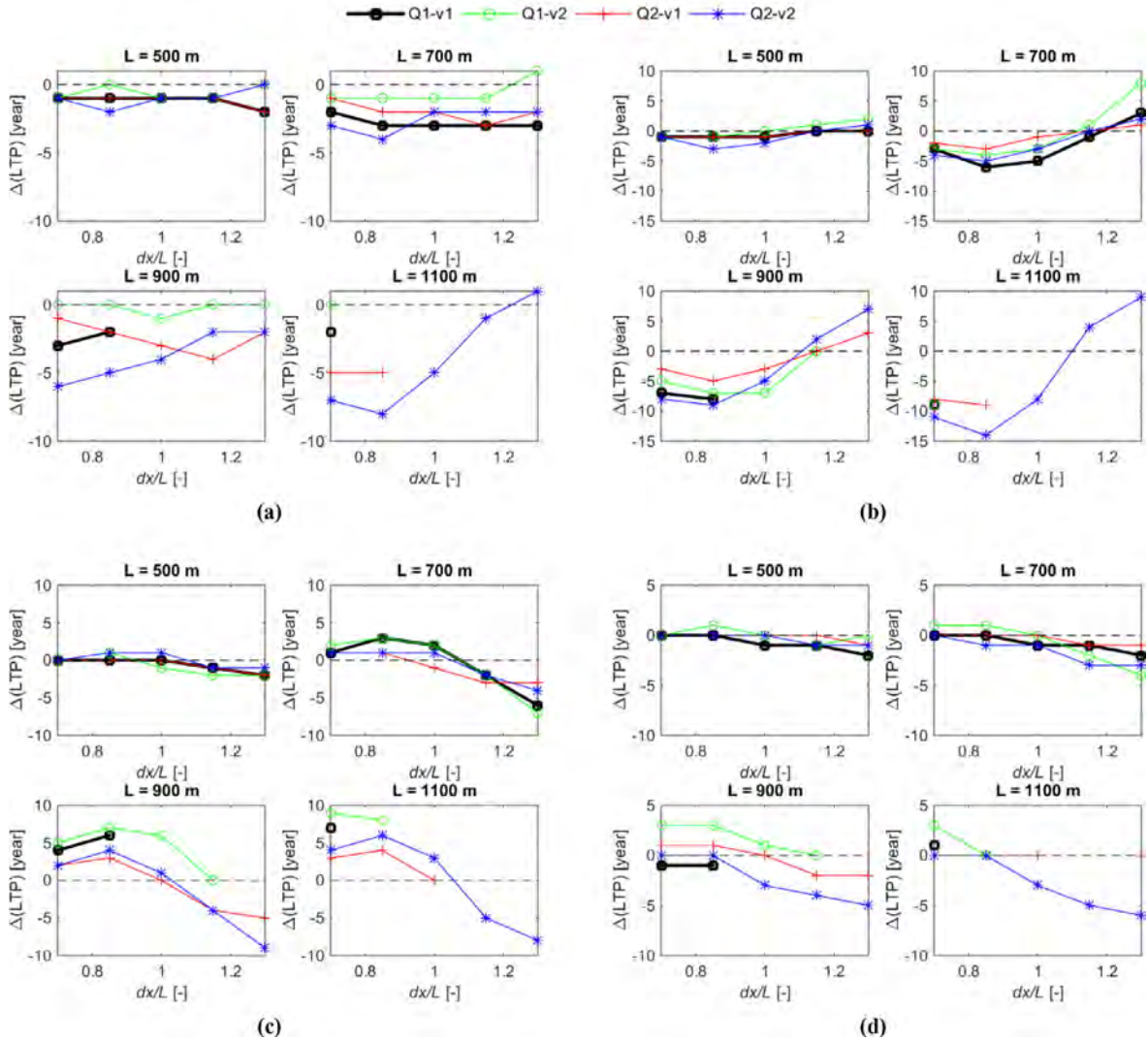


**Fig. 10.** Life time differences ( $\Delta LTP$ ) as an impact of varying correlation lengths and well spacing: (a)  $LTP_{C4} - LTP_{C1}$ , (b)  $LTP_{C2} - LTP_{C1}$ , (c)  $LTP_{C4} - LTP_{C2}$  and (d)  $LTP_{C4} - LTP_{C3}$ . In each plot,  $L$  is fixed while  $\Delta(LTP)$  is plotted with respect to varying  $dx/L$ .

temperature of production wells has dropped  $1^\circ\text{C}$  with respect to initial condition.

5. *Life time based on (average) production:* LTP of geothermal heat recovery operation defined as the time (in years) when  $\langle T_p^t \rangle = \frac{\langle TW_{p1}^t \rangle + \langle TW_{p2}^t \rangle}{2}$  has dropped  $1^\circ\text{C}$  with respect to initial condition.
6. *Life time based on (average) production:* LTP<sub>n</sub> of geothermal heat recovery operation defined as the time (in years) when  $\langle T_p^t \rangle = \frac{\langle TW_{p1}^t \rangle + \langle TW_{p2}^t \rangle}{2}$  has dropped  $n^\circ\text{C}$  with respect to initial condition.
7. *Life time based on boundary of license area:* LTB of geothermal heat recovery operation defined as the time (in years) when average temperature over the license area boundary has dropped  $1^\circ\text{C}$  with respect to the initial average temperature. This property is calculated based on the converged solution of the average temperature in license region's boundary ( $T_B^t$ ).
8. *Coefficient of Performance* defined as:

$$CoP = \frac{E_{prod}}{E_{pump}}, \quad (9a)$$

$$E_{prod} = (\rho C)_w Q \int_{t=0}^{LTB} (\langle T_w^t \rangle - T_{inj}) dt, \quad (9b)$$

$$E_{pump} = \frac{Q}{\epsilon} \int_{t=0}^{LTB} (\langle p_{inj} - p_{prd} \rangle) dt \quad (9c)$$

where  $E_{prod}$  is the energy produced from production wells and  $E_{pump}$  is an estimation of pump energy losses [10], in which  $\epsilon$  is the pump efficiency of %60, and  $\langle p_{inj} - p_{prd} \rangle$  is calculated by using the converged solution for well bottom-hole pressures of two doublets.

9. *Energy Sweep* is an indicator of how efficiently heat in the control volume is extracted. This is defined as:

$$S = \frac{E_{prod}}{E_R}, \quad (10a)$$

$$E_R = \int_{i=1}^{N_b} (\rho_w C_w \phi_i + \rho_r C_r (1 - \phi_i)) (T_{init,i} - T_{inj}) dV_{bi}. \quad (10b)$$

where  $E_R$  is the available reservoir energy of the license area,  $V_{bi}$  is the bulk volume of gridblock  $i$  in the license area ( $2L \times 2dx \times 10$  layers around the doublets),  $N_b$  is the number of gridblocks in the license area, and  $E_{prod}$  is the geothermal energy recovered by the doublets until the converged solution based-life-time of the operation.

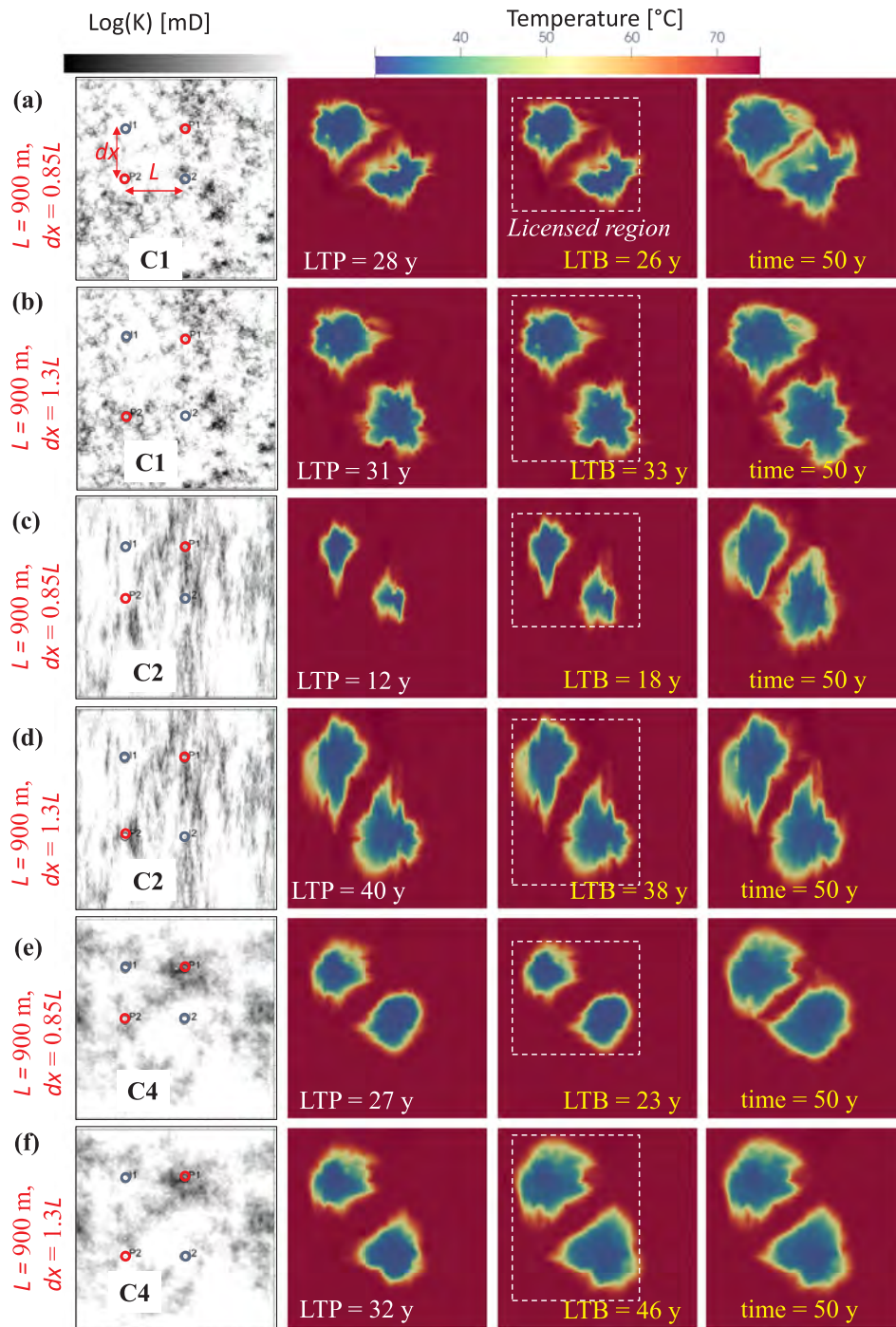


**Fig. 11.** Permeability and temperature distributions (at different time: LTP, LTB and 50 years) for six selected simulation samples/realizations: row (a) C1 low  $dx$ , row (b) C1 high  $dx$ , row (c) C2 low  $dx$ , row (d) C2 high  $dx$ , row (e) C4 low  $dx$ , and row (f) C4 high  $dx$ . The first column: the permeability distribution and the locations of wells, the second column: temperature distribution at LTP (of the realization), the third column: temperature distribution at LTB (of the realization), and the fourth column: temperature distribution at the end of simulation.

### 3. Results and discussion

#### 3.1. Lifetime analysis: boundary vs. production wells-based comparison

Fig. 4(a) shows LTP for various correlation lengths (C1, C2, C3 and C4), injection rates (Q1 and Q2) and variances in porosity field ( $v1$  and  $v2$ ). The profiles are plotted versus  $L$  and for  $dx = L$  only. As a result there are 16 profiles in this figure. In this figure and the rest of figures in this manuscript, black represents Q1- $v1$  simulation results, green Q1- $v2$ , red Q2- $v1$  and blue Q2- $v2$ . Yellow lines represent homogeneous

simulations. Some of the profiles are incomplete with respect to  $L$ . This is because the average temperature has not dropped 1 °C during 50 years of operation. From Fig. 4(a) it is clear that:

- Increase in injection ( $Q$ ) and variance of porosity fields ( $v$ ) lead to decrease in lifetime. This is trivial as cold water front reaches to production wells earlier for higher  $Q$  and  $v$ .
- Between each fixed pairs of  $Q$ - $v$ , there are 4 profiles for each correlation lengths ( $C$ ). Between them, C1 ( $c_x = 100$  m and  $c_y = 100$  m) leads to largest lifetimes and C2 ( $c_x = 500$  m and  $c_y = 100$  m) leads to

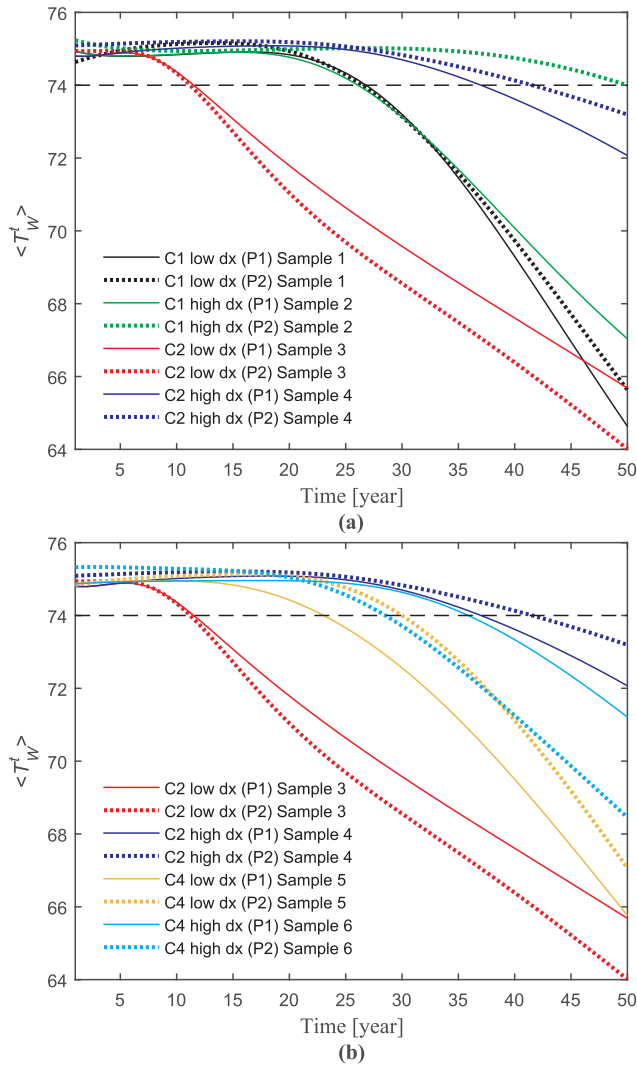


Fig. 12. The profiles of  $\langle T_w^t \rangle$  over time for six selected simulation samples: (a) C1 and C2 samples, and (b) C2 and C4 samples.

lowest lifetimes. This point will be further analyzed and discussed in Section 3.3.

- Considering a minimum lifetime of 20 years and an average temperature drop of 1°C at the license boundary as the main indicators of the lifetime, the minimum well distances for Q1 and Q2 (regardless of the heterogeneity variance) are 700 m and 900 m, respectively.
- Considering a minimum lifetime of 30 years and an average temperature drop of 1°C at the license boundary as the main indicators of the lifetime, the minimum well distances for Q1-H, Q1-v1, Q1-v2, Q2-H, Q1-v1, and Q1-v2 (regardless of the correlation lengths) are about 650 m, 750 m, 800 m, 900 m, 950 m, and 1000 m, respectively.

Fig. 4(b) shows LTB for various correlation lengths (C1, C2, C3 and C4), injection rates (Q1 and Q2) and variances in porosity field (v1 and v2), when  $dx = L$ . Evidently, LTB is less sensitive towards the correlation lengths and the profiles in each particular group of Q-v are less spread. Similar conclusions can be made for  $dx = 0.7L$ ,  $dx = 0.85L$ ,  $dx = 1.15L$  and  $dx = 1.3L$  as shown in Fig. 4(c) and (d).

In order to demonstrate the impact of well or doublet spacing on lifetimes (boundary vs. production wells-based calculations), in Fig. 5 all realizations as well as converged solutions are grouped into fixed

$dx/L$  (varying  $L$ ) or fixed  $L$  (varying  $dx$ ). Starting from Fig. 5(a), for all realizations, LTB are plotted vs.  $LW_{P1}$ . In each plot, injection rate ( $Q$ ), variance ( $v$ ) and  $L$  vary. The scattered markers above the 45° line, show that  $LTB > LW_{P1}$ . However, there is no dominant pattern in results in order to make a conclusion that LTB is higher than  $LW_{P1}$ . Moreover between different  $dx/L$ 's in Fig. 5(a), the extent of lifetimes in x- and y-axes are the same. Therefore, the variation in doublet spacing does not have a clear impact on lifetimes. Conversely, Fig. 5(c) shows that by increasing well spacing ( $L$ ) the lifetimes increase and scatter markers shift towards right of the plot.

Comparing LTB with  $LW_{P1}$ , the scatter markers are mostly above the 45° line, but not all of the realizations produced this trend. For the converged solutions (Fig. 5b and Fig. 5d), there is a general but not a universal trend of  $LTB > LTP$  for  $dx/L = 0.7$  and  $0.85$ ,  $L = 900$  m and  $L = 1100$  m. Nevertheless, for v2 (green and blue markers), we can deduct that  $LTB > LTP$ . This is because for v2 the breakthrough of cold water is happening too early (because of heterogeneity of the system) while the licensed region still has some energy left. We discuss this in details in the next subsection.

### 3.2. Determining the license area's extent from temperature distribution

If  $LTB > LTP$ , the geothermal system has still energy to produce by the time that the production wells signal the temperature drop. This means that the license boundary chosen has not experienced the same level of temperature drop by the time that the production wells have. Here we show that the license boundary can be in fact calculated in a way that the boundaries experience the threshold temperature drop of 1°C. We show that these boundaries are not necessarily the same as  $2dx \times 2L$  which were conventionally assumed.

We calculate the distribution of the actual boundaries of license area around operating wells based on a simple search algorithm. To this end, for the case of  $L = dx$  (which was shown to consistently result in optimal well/doublet spacing solutions), and  $L = 500$  m, 700 m and 900 m, Q1 and Q2, fixed v2 (with a general trend of  $LTB > LTP$ ), and C1, C2 and C4, first we calculate  $LTP1$ ,  $LTP5$  and  $LTP10$ , where  $LTPn$  represents production lifetimes when the converged solution for production wells ( $\langle T_w^t \rangle$ ) experiences  $n$  °C temperature drop. Then, for each realization and at  $LTPn$ , we search for a square license area around the wells so that for its boundary blocks, the average temperature drop is 1°C. The length of this square is denoted by  $L'$  ( $= dx'$ ). Also similarly we find a boundary where the cold plume has farthest spread. That is we search for a farthest boundary away from the wells where the difference between the minimum temperature of that boundary and the initial temperature of that boundary is 1°C. This boundary represents the extent of cold front. We denote this boundary with  $L''$  ( $= dx''$ ).

Fig. 6 shows the results of this analysis. For each  $LTPn$  ( $LTP1$ ,  $LTP5$  and  $LTP10$ ), we show  $L'/L$  and  $L''/L$  for C1 (averaged over all realizations of C1), for C2 (averaged over all realizations of C2), and for C4 (averaged over all realizations of C4). In each subfigure there are four lines for Q1-v2 (for  $L'/L$ ), Q1-v2 (for  $L''/L$ ), Q2-v2 (for  $L'/L$ ) and Q2-v2 (for  $L''/L$ ). The following observations can be made from this figure:

1. For  $L < 1000$  m and the well temperature drop of  $< 10$  °C, both  $L'/L$  and  $L''/L$  can be as large as 1.25 and 1.5, respectively.
2. Impact of discharge ( $Q$ ) on the size of the license area is not as important as how the constraint is considered for the temperature drop at the license boundary, i.e., an average 1°C or a local 1°C temperature. Note that obviously for a given case  $L''$  is always larger than  $L'$ .
3. For C4 cases  $L'$  and  $L''$  decrease by increasing the well distance ( $L$ ) implying that for  $L >$  than 1000 m the license boundary can be chosen as  $2L \times 2L$  ( $= 2dx \times 2dx$ ) or slightly larger. For both C1 and C2 cases  $L'$  and  $L''$  remain more or less similar for different  $L$  values between 500 m and 900 m.
4. In most cases for the systems with a lifetime defined as 10 °C (or

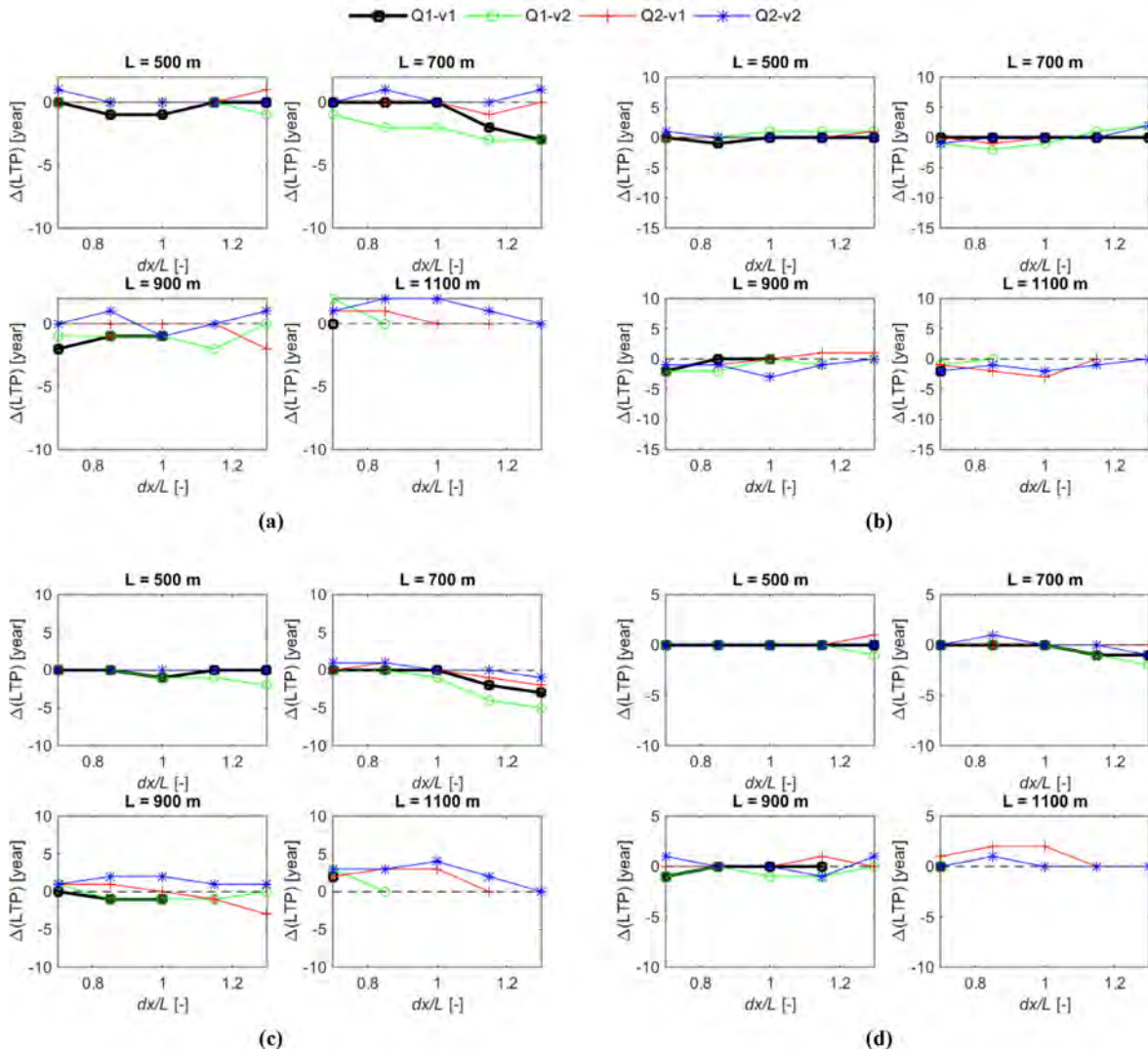


**Fig. 13.** Life time differences ( $\Delta(LTB)$ ) as an impact of varying correlation lengths: (a)  $LTB_{C4} - LTB_{C1}$ , (b)  $LTB_{C2} - LTB_{C1}$ , (c)  $LTB_{C4} - LTB_{C2}$  and (d)  $LTB_{C4} - LTB_{C3}$ . In each plot,  $L$  is fixed while  $\Delta(LTB)$  is plotted with respect to varying  $dx/L$ .

lower) temperature drop at the production wells,  $L'/L$  is between 1 and 1.2 suggesting that the license boundary can be designed as  $2.4L \times 2.4L$  if the constraint for the lifetime is defined as the average temperature drop of  $1^\circ\text{C}$  at the license boundary.

Since the lifetime resulted for LTP5 and LTP10 considered for the calculation of  $L'$  and  $L''$  are more than what is usually considered as the geothermal lifetime (e.g., 30 years) the  $L'$  and  $L''$  for constant lifetimes of 20, 30 and 40 years, and a constraint of  $TP < 10^\circ\text{C}$  are shown in Fig. 7. For all the cases  $L'$  and  $L''$  decrease by increasing the well distance ( $L$ ). If an average temperature drop of  $1^\circ\text{C}$  is considered for a lifetime of 30 years,  $L'$  is almost equal or smaller than  $L$  for a well distance of 700 m and 900 m for Q1 and Q2, respectively. These increase by 20% for the lifetime of 40 years.

Fig. 8 depicts the temperature field and the license boundaries defined based on different constraints for realization 1 of C1 and C2, and for different  $Q$  and  $L$  values. Fig. 9 shows similar results for the converged solutions.

The animations for the development of cold front for the examples shown in Fig. 8 and Fig. 9 are provided in Videos 1 to 8. The videos are zoomed in around the license areas for better visualization purposes and the stills are taken at the production time equal to 10 years. The videos represent how the swept area advances in time for different well

distances and heterogeneous fields. Comparing the results of geothermal systems with  $L = 500\text{ m}$  for different  $Q$  suggests that while a minimum well distance of  $L = 500\text{ m}$  might be enough to provide a lifetime of greater than 20 years for a discharge of  $150\text{ m}^3/\text{hr}$ , this well distance is not proper for higher discharge values. For a discharge of  $250\text{ m}^3/\text{hr}$  the results suggest that a well distance of 700 m provides a lifetime of more than 25 and 35 years for LTP5 and LTP10, respectively.

### 3.3. Effects of correlated heterogeneity

To investigate the impact of correlation lengths on operation lifetimes, Fig. 10 shows the difference in LTP between C4 and C1 in Fig. 10(a), C2 and C1 in Fig. 10(b), C4 and C2 in Fig. 10(c), and C4 and C3 in Fig. 10(d). All profiles are plotted with respect to  $dx/L$  for fixed  $L$ 's. The following observations can be made:

1. By increasing correlation lengths in both directions from 100 m to 500 m, Fig. 10(a) shows that almost universally lifetimes decrease (negative values in y-axis). The difference between lifetimes of C4 and C1 increases as  $L$  increases.
2. By increasing correlation lengths in only y-direction from 100 m to 500 m, Fig. 10(b) shows that lifetime decreases further (larger negative values in y-axis) for small doublet spacings ( $dx = 0.7L$  and

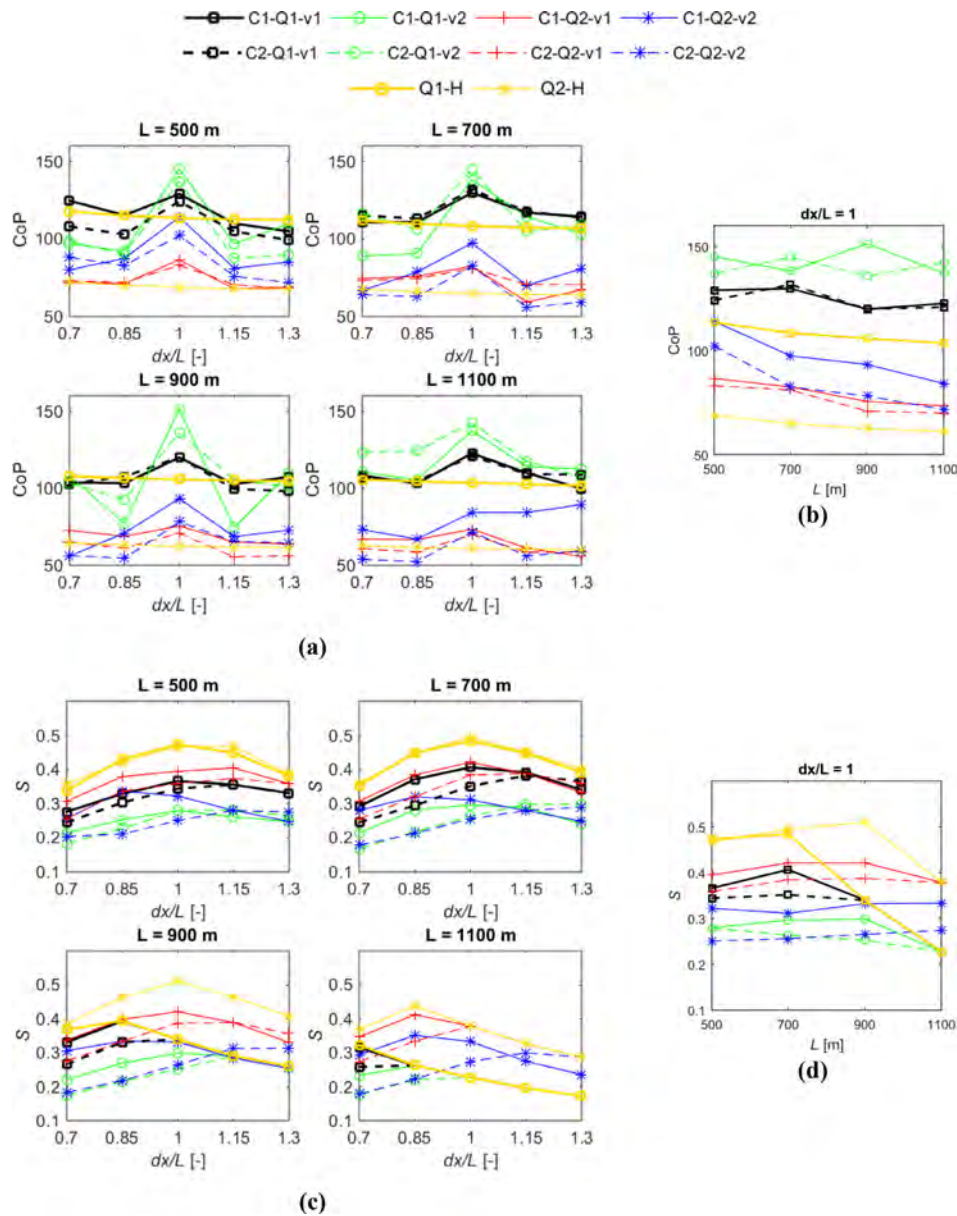


Fig. 14. (a) CoP vs.  $dx/L$  for fixed  $L$ 's, (b) CoP vs.  $L$  for fixed  $dx/L = 1$ , (c)  $S$  vs.  $dx/L$  for fixed  $L$ 's, and (d)  $S$  vs.  $L$  for fixed  $dx/L = 1$ . These are all calculated at LTP.

$dx = 0.85L$ ). However the trend reverses around  $dx = 0.85L$  so that for high  $dx$  values, lifetimes of C2 is actually higher than C1. This positive difference increases for larger  $L$ 's, and specially for Q2-v2 (blue lines).

3. Figs. 10(c) and (d) show that the trend for above points are reversed when we compare C4 with C2 and C4 with C3. That is, for low  $dx/L$  values, the higher correlation length in both directions, the larger lifetimes are observed, while for large  $dx/L$  values, the higher correlation length in both directions, the lower lifetimes are observed. Again the differences between lifetimes increases with higher  $L$ ,  $Q$  and  $v$ .
4. An anisotropic large correlation lengths in a geothermal reservoir reduces production wells-based lifetimes for small doublet spacings, while increases production wells-based lifetimes for large doublet spacings compared to isotropically correlated heterogeneous reservoir systems.

In order to investigate the impact of directional (anisotropic) correlated heterogeneity on lifetime of operation, here, we review the results of six simulation samples between different correlation lengths,

namely, C1, C2 and C4, and different doublet spacings, namely,  $dx/L = 0.85$  and  $dx/L = 1.3$ :

- Sample 1:  $\ell = 1$ , Q2, v2, C1,  $L = 900$  m,  $dx/L = 0.85$  (low  $dx$ ),
- Sample 2:  $\ell = 1$ , Q2, v2, C1,  $L = 900$  m,  $dx/L = 1.3$  (high  $dx$ ),
- Sample 3:  $\ell = 1$ , Q2, v2, C2,  $L = 900$  m,  $dx/L = 0.85$  (low  $dx$ ),
- Sample 4:  $\ell = 1$ , Q2, v2, C2,  $L = 900$  m,  $dx/L = 1.3$  (high  $dx$ ),
- Sample 5:  $\ell = 1$ , Q2, v2, C4,  $L = 900$  m,  $dx/L = 0.85$  (low  $dx$ ),
- Sample 6:  $\ell = 1$ , Q2, v2, C4,  $L = 900$  m,  $dx/L = 1.3$  (high  $dx$ ).

Fig. 11 shows the permeability distribution (first column) and temperature distributions (second, third and fourth columns) of the reservoir top layer. The temperature distributions are plotted at LTP (second column), LTB (third column) and at the end of simulation (fourth column) for the six samples defined above. The locations of wells are also superimposed on the permeability distribution profiles. Corresponding to these distribution profiles, Fig. 12, shows the flow-rate-weighted average temperature of the two production wells ( $\langle T_W^t \rangle$ ) of P1 and P2) for these samples.

We first concentrate on  $\langle T_W^t \rangle$  of Sample 1 and Sample 3 (low  $dx$  but

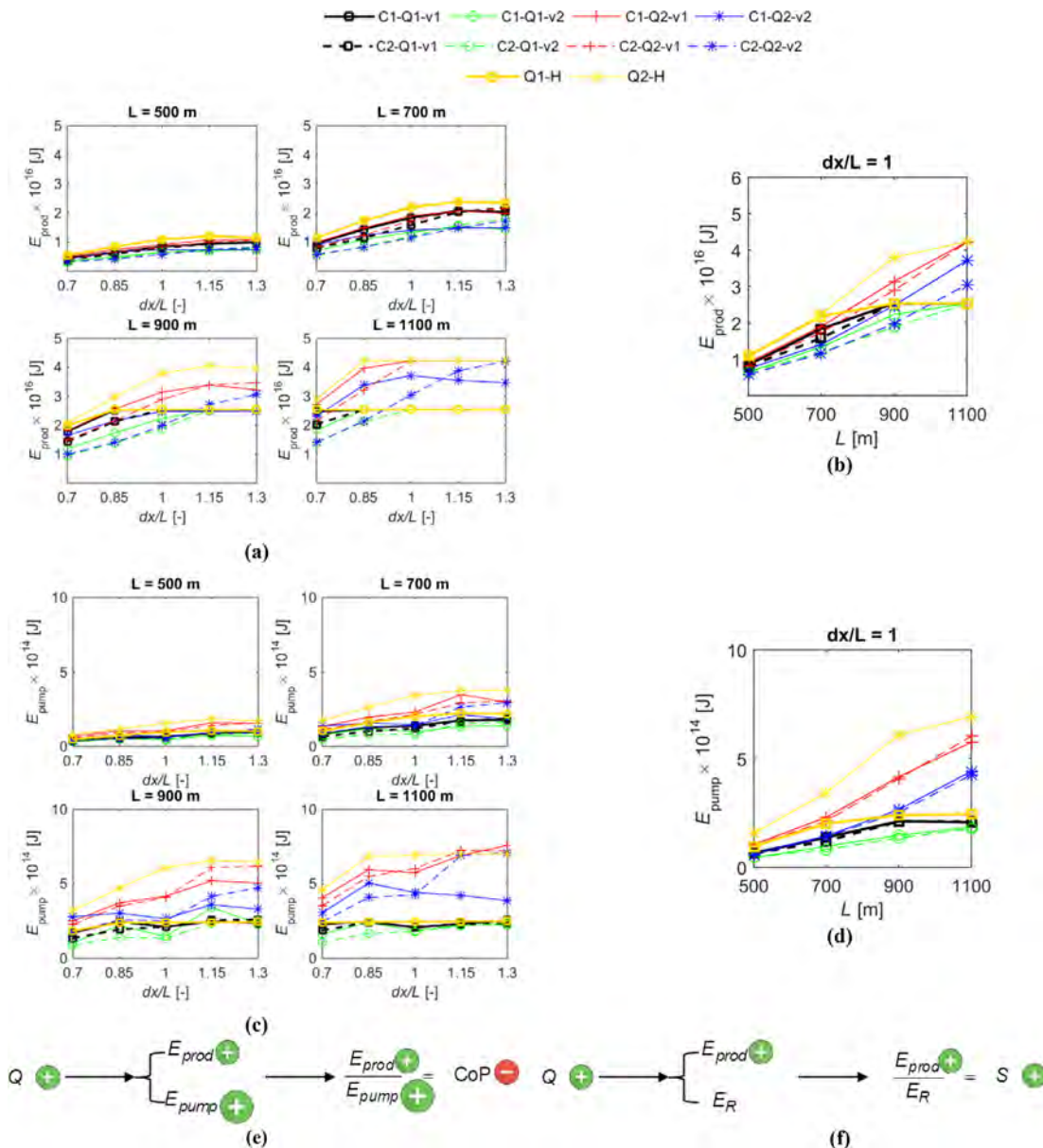


**Fig. 15.** (a)  $E_{prod}$  vs.  $dx/L$  for fixed  $L$ 's, (b)  $E_{prod}$  vs.  $L$  for fixed  $dx/L = 1$ , (c)  $E_{pump}$  vs.  $dx/L$  for fixed  $L$ 's calculated at LTP, (d)  $E_{pump}$  vs.  $L$  for fixed  $dx/L = 1$ , (e) an illustration of how flow rate increase impacts CoP based on  $E_{prod}$  and  $E_{pump}$  dependency on  $Q$ , and (f) an illustration of how flow rate increase impacts  $S$  based on  $E_{prod}$  and  $E_{pump}$  dependency on  $Q$ . These are all calculated at LTP.

varying correlation lengths of C1 and C2, respectively corresponding to Fig. 11row a) and Fig. 11row c), and black and red lines in Fig. 12(a)). The early temperature drop of Sample 3 wells (both P1 and P2) compared to Sample 1 can be directly attributed to the correlated heterogeneity in  $y$ -direction (along doublet spacing:  $dx$ ) that has transported cold water quickly to P2. As a result of these complications, LTP of Sample 1 is higher than Sample 3, and this corroborates results shown in Fig. 10(b) for  $L = 900$  m, Q2-v2 (blue line) at  $dx/L = 0.85$  where  $LTP_{C2} - LTP_{C1} \approx -10$  years. Such effects of correlated heterogeneity (or channelised heterogeneity) has also been studied in details in a recent publication by Lie et al. [16].

Next, we focus on  $\langle T_w^t \rangle$  of Sample 2 and Sample 4 (high  $dx$  but varying correlation lengths of C1 and C2, respectively corresponding to Fig. 11row b) and Fig. 11row d), and green and blue lines in Fig. 12(a)). In this instance, P2 is experiencing similar temperature drops between two cases. This is because P2 is sufficiently away from I1, so that correlated heterogeneity along I1-P2 corridor cannot lead to quick advection of cold water to P2. Nonetheless, the difference in lifetime

between Sample 2 and Sample 4 is made by P1. For Sample 4, the directional correlated heterogeneity is distorting the cold water fronts of both I1 and I2 to the benefit of P1. That is, large parts of cold water fronts of I1 and I2 move alongside  $y$ -direction but in the opposite direction towards P1, so that breakthrough at P1 takes place later for Sample 4 compared to Sample 2. As a result of these complications, LTP of Sample 4 is higher than Sample 2, and this corroborates results shown in Fig. 10(b) for  $L = 900$  m, Q2-v2 (blue line) at  $dx/L = 1.3$  where  $LTP_{C2} - LTP_{C1} \approx 5$  years.

Next, we focus on  $\langle T_w^t \rangle$  of Sample 3 and Sample 5 (low  $dx$  but varying correlation lengths of C2 and C4, respectively corresponding to Fig. 11row c) and Fig. 11row e), and red and orange lines in Fig. 12(b)). The comparison is the same as comparison made between Sample 1 and Sample 3, with Sample 5 behaving similar to Sample 1 when compared to Sample 3. Due to isotropic correlated heterogeneity and proximity of doublets, the rather circular cold front did not lead to an early breakthrough of cold water front as of Sample 3. Consequently, LTP of Sample 5 is higher than Sample 3, and this corroborates results shown

in Fig. 10(c) for  $L = 900$  m, Q2-v2 (blue line) at  $dx/L = 0.85$  where  $LTP_{C4} - LTP_{C2} \approx 5$  years.

Finally, we focus on  $\langle T_w^t \rangle$  of Sample 4 and Sample 6 (high  $dx$  but varying correlation lengths of C2 and C4, respectively corresponding to Fig. 11 row d) and Fig. 11 row f), and blue and cyan lines in Fig. 12b). In contrast to comparison between Sample 4 and Sample 2, P2 (and not P1) makes the difference in determining lifetime. Anisotropic correlated heterogeneity of Sample 4 accounts for preventing the cold water front of I2 to reach P2. Consequently, LTP of Sample 4 is higher than Sample 6, and this corroborates results shown in Fig. 10(c) for  $L = 900$  m, Q2-v2 (blue line) at  $dx/L = 1.3$  where  $LTP_{C4} - LTP_{C2} \approx -10$  years.

The fact that either P1 Sample 2 or P2 in Sample 6 experience earlier breakthroughs than P1 or P2 in Sample 4 is random, however, it is due to isotropicity of correlated heterogeneity of Sample 2 and Sample 6 compared to Sample 4. Further to above-mentioned comparisons between different correlation length samples, the comparison of C4 with C1, and C4 with C3 is evident from discussions above and supported by Fig. 10(a) and Fig. 10(d). That is,  $LTP_{C4} - LTP_{C1} < 0$  due to impact of isotropic heterogeneity, and  $LTP_{C4} - LTP_{C3} > 0$  for small  $dx$  values and  $LTP_{C4} - LTP_{C3} < 0$  for large  $dx$  values. While the six samples above were taken from one realization only, it is evident that the converged solution has produced the same ranking between different correlation length cases with respect to production wells-based lifetimes (LTP).

In contrast to all variations in the production wells-based lifetimes observed as a result of change in correlation lengths, Fig. 13 shows that license boundary-based lifetimes (LTB) are significantly less sensitive towards this parameter and as such can be used to reduce uncertainty. This finding is corroborated by examining LTB of six samples investigated above and shown in Fig. 11 (third column). The magnitude of difference between LTB's are less than the magnitude of difference between LTP's, for most of the comparisons. For example,  $(LTP_{\text{Sample 3}} - LTP_{\text{Sample 1}}) = -16$  y vs.  $(LTB_{\text{Sample 3}} - LTB_{\text{Sample 1}}) = -8$  y,  $(LTP_{\text{Sample 4}} - LTP_{\text{Sample 2}}) = 9$  y vs.  $(LTB_{\text{Sample 4}} - LTB_{\text{Sample 2}}) = 5$  y, and  $(LTP_{\text{Sample 5}} - LTP_{\text{Sample 3}}) = 15$  y vs.  $(LTB_{\text{Sample 5}} - LTB_{\text{Sample 3}}) = 5$  y. Only for comparison between Sample 6 and Sample 4, the magnitude of differences are equal:  $(LTP_{\text{Sample 6}} - LTP_{\text{Sample 4}}) = -8$  y vs.  $(LTB_{\text{Sample 6}} - LTB_{\text{Sample 4}}) = 8$  y. Therefore the selected examples, clearly demonstrate that LTB is significantly less sensitive towards correlation lengths and heterogeneity of geothermal system. It is evident in Fig. 13 that the impact of the correlation length on the LTB is less than 5 years.

### 3.4. Coefficient of performance and energy sweep

Figs. 14(a) and 14(b) show the profiles of *Coefficient of Performance* (CoP) and *Energy Sweep* ( $S$ ) calculated from Eq. (9) and (10) as functions of well and doublet spacing for the converged solution at LTP. To avoid crowded figures, only C1 and C2 correlation-length cases are shown.

Fig. 14(a and b) shows that

1. For each fixed well spacing, while for heterogeneous cases the optimal doublet spacing is at  $dx/L = 1$  (in the middle), for homogeneous cases the doublet spacing has negligible impact on CoP.
2. The highest CoP's are obtained for Q1-v2 at  $dx/L = 1$ , however, considering the profiles for other  $dx/L$  values, Q1-v1 has consistently led to the best CoP's.
3. One clear observation is the dramatic reduction of CoP due to increase in injection rate ( $Q$ ). This has also happened for homogeneous cases (compare Q1-H with Q2-H).
4. Similar to the homogeneous reservoirs, for most heterogeneous cases CoP decreases as  $L$  increases for  $dx/L = 1$ .
5. The increase in correlation length mostly decreases CoP.

From Fig. 14(c and d) for  $S$ , the following observations can be made:

1. Heterogeneity in general reduces  $S$  especially for lower  $L$  values.

2. Except for the highest  $L = 1100$  m, increasing the variance of porosity fields ( $v$ ) reduces  $S$  (green and blue lines compared to black and red lines).
3. Increasing the injection rate ( $Q$ ) increases  $S$ .
4. It is evident that  $dx/L = 1$  is consistently producing the maximum values for  $S$ .
5. The increase in correlation length mostly decreases  $S$ .
6. Similar to the homogeneous reservoirs, for most heterogeneous cases  $S$  decreases as  $L$  increases for  $dx/L = 1$ .

In summary, the increase in correlation length in y-direction (C2 compared to C1) will largely lead to decrease in both CoP and  $S$ , with few exceptions when  $dx/L > 1$ . The increase in variance of the porosity fields (green lines compared to black lines, and blue lines compared to red lines), largely decreases  $S$ , but the impact on CoP varies for each  $dx/L$ . These results suggest that the shorter well distance may provide higher  $S$  and CoP. While higher injection rate increases  $S$ , it has a negative impact on the CoP.

Fig. 15(a-d) show the profiles of  $E_{\text{prod}}$  and  $E_{\text{pump}}$  as functions of well and doublet spacing for the converged solution and the homogeneous simulations. The results show that both of these properties increase with increase in well and doublet spacings due to increasing the lifetime. However, just at  $dx/L = 1$ , the ratio of  $E_{\text{prod}}$  over  $E_{\text{pump}}$  produces a maximum for heterogeneous models. Also with increase in injection rate,  $E_{\text{prod}}$  and  $E_{\text{pump}}$  increase. However, increase in  $E_{\text{pump}}$  is larger than increase in  $E_{\text{prod}}$ , so that CoP decreases by increase in  $Q$ , while since  $E_R$  is independent of  $Q$ ,  $S$  increases with  $Q$ . The changes in CoP and  $S$  as a function of  $Q$  is illustrated in Figs. 15(e) and 15(f).

## 4. Conclusions and future works

A comprehensive set of numerical simulations were carried out on synthetic homogeneous and heterogeneous low-enthalpy aquifer system, with a range of operational and physical parameters of the subsurface system. Using multiple performance metrics, the following conclusions were made:

1. Heterogeneity undermines performance of geothermal systems in terms of *Life Time* of the operation,
2. Spatially highly correlated heterogeneity undermines performance of geothermal systems compared to low correlated systems or randomly distributed heterogeneity,
3. An anisotropically correlated heterogeneous system performs worse than isotropically correlated heterogeneous systems for large well and doublet spacings,
4. Increase in operational flow rate can increase *Energy Sweep* while decrease *Coefficient of Performance*,
5. A doublet spacing equal to well spacing robustly leads to best performance of the operation,
6. Use of license area's boundary showed less uncertainty with respect to various operational and physical parameters, suggesting a better control criterion for the operation design.
7. The difference between lifetimes based on production wells and license area's boundary is minimum for when well and doublet spacings are equal.
8. Sufficient lifetime (>20 years) could be achieved for the well spacing of less than 900 m for a discharge of 250 m<sup>3</sup>/hr. The lifetime can be increased significantly or the well spacing can be further reduced if larger temperature drop (>1 °C) at the producers are permitted. This would however require a larger license area than the  $2dx \times 2L$  in order to minimise the negative interference with the neighbouring geothermal projects.

Future directions include use of robust optimisation algorithms to obtain optimal well or doublet spacing for heterogeneous geothermal systems. While previously, Kong et al. [25] conducted optimization of

geothermal systems using homogeneous models, the heterogeneity will have non-trivial effects on positions of wells and doublets, and consequently it will also impact optimal solutions. The well spacings can be optimised further with including the economics of the project.

### Acknowledgment

The study was supported by University of Manchester EPS Fund 2015 with which the computational facilities of this research were procured. MB would like to thank this institution. MB also thanks EPSRC for grant EP/R009678/1 that allowed studies of heterogeneous porous systems at various length scales to be carried out by MB. HN would like to thank Harmen Mijnlief (TNO), Raymond Godderij (EBN) and Frank Schoof (Platform Geothermie) for their helpful discussions. The authors also thank anonymous reviewers for their constructive comments.

### Appendix A. Supplementary material

Supplementary data associated with this article can be found, in the online version, at <https://doi.org/10.1016/j.apenergy.2019.113569>.

### References

- [1] Bonté D, Van Wees J-D, Verweij J. Subsurface temperature of the onshore Netherlands: new temperature dataset and modelling. *Neth J Geosci* 2012;91(04):491–515.
- [2] Poulsen S, Balling N, Nielsen S. A parametric study of the thermal recharge of low enthalpy geothermal reservoirs. *Geothermics* 2015;53:464–78.
- [3] Ma R, Zheng C. Effects of density and viscosity in modeling heat as a groundwater tracer. *Groundwater* 2010;48(3):380–9.
- [4] Saeid S, Al-Khoury R, Nick HM, Barends F. Experimental–numerical study of heat flow in deep low-enthalpy geothermal conditions. *Renew Energy* 2014;62:716–30.
- [5] Mottaghy D, Pechnig R, Vogt C. The geothermal project den haag: 3d numerical models for temperature prediction and reservoir simulation. *Geothermics* 2011;40(3):199–210.
- [6] Vogt C, Iwanowski-Strahser K, Marquart G, Arnold J, Mottaghy D, Pechnig R, et al. Modeling contribution to risk assessment of thermal production power for geothermal reservoirs. *Renew Energy* 2013;53:230–41.
- [7] Saeid S, Al-Khoury R, Nick HM, Hicks MA. A prototype design model for deep low-enthalpy hydrothermal systems. *Renew Energy* 2015;77:408–22.
- [8] Willems CJ, Nick HM, Weltje GJ, Bruhn DF. An evaluation of interferences in heat production from low enthalpy geothermal doublets systems. *Energy* 2017;135:500–12.
- [9] Pandey S, Vishal V. Sensitivity analysis of coupled processes and parameters on the performance of enhanced geothermal systems. *Scient Rep* 2017;7(1):17057.
- [10] Willems C, Nick H, Goense T, Bruhn D. The impact of reduction of doublet well spacing on the net present value and the life time of fluvial hot sedimentary aquifer doublets. *Geothermics* 2017;68:54–66.
- [11] Pandey S, Vishal V, Chaudhuri A. Geothermal reservoir modeling in coupled thermo-hydro-mechanical-chemical approach: a review. *Earth-Sci Rev*.
- [12] Watanabe N, Wang W, McDermott CI, Taniguchi T, Kolditz O. Uncertainty analysis of thermo-hydro-mechanical coupled processes in heterogeneous porous media. *Comput Mech* 2010;45(4):263.
- [13] Crooijmans R, Willems C, Nick H, Bruhn D. The influence of facies heterogeneity on the doublet performance in low-enthalpy geothermal sedimentary reservoirs. *Geothermics* 2016;64:209–19.
- [14] Willems CJ, Nick HM, Donselaar ME, Weltje GJ, Bruhn DF. On the connectivity anisotropy in fluvial hot sedimentary aquifers and its influence on geothermal doublet performance. *Geothermics* 2017;65:222–33.
- [15] Niederau J, Ebigbo A, Marquart G, Arnold J, Clauser C. On the impact of spatially heterogeneous permeability on free convection in the perth basin, australia. *Geothermics* 2017;66:119–33.
- [16] Liu G, Pu H, Zhao Z, Liu Y. Coupled thermo-hydro-mechanical modeling on well pairs in heterogeneous porous geothermal reservoirs. *Energy* 2019;171:631–53.
- [17] Salimzadeh S, Nick HM, Zimmerman R. Thermoporoelastic effects during heat extraction from low-permeability reservoirs. *Energy* 2018;142:546–58.
- [18] Vik HS, Salimzadeh S, Nick HM. Heat recovery from multiple-fracture enhanced geothermal systems: the effect of thermoelastic fracture interactions. *Renew Energy* 2018;121:606–22.
- [19] Vasilyeva M, Babaei M, Chung ET, Spiridonov D. Multiscale modelling of heat and mass transfer in fractured media for enhanced geothermal systems applications. *Appl Math Model* 2018;67:159–78.
- [20] Salimzadeh S, Grandahl M, Medetbekova M, Nick H. A novel radial jet drilling stimulation technique for enhancing heat recovery from fractured geothermal reservoirs. *Renew Energy* 2019;139:395–409.
- [21] Wang F, Deng S, Zhao J, Zhao J, Yang G, Yan J. Integrating geothermal into coal-fired power plant with carbon capture: a comparative study with solar energy. *Energy Convers Manage* 2017;148:569–82.
- [22] Pandey S, Chaudhuri A. The effect of heterogeneity on heat extraction and transmissivity evolution in a carbonate reservoir: a thermo-hydro-chemical study. *Geothermics* 2017;69:45–54.
- [23] Salimzadeh S, Nick H. A coupled model for reactive flow through deformable fractures in enhanced geothermal systems. *Geothermics* 2019;81:88–100.
- [24] Chen M, Tompson AF, Mellors RJ, Abdalla O. An efficient optimization of well placement and control for a geothermal prospect under geological uncertainty. *Appl Energy* 2015;137:352–63.
- [25] Kong Y, Pang Z, Shao H, Kolditz O. Optimization of well-doublet placement in geothermal reservoirs using numerical simulation and economic analysis. *Environ Earth Sci* 2017;76(3):118.
- [26] Schlumberger. ECLIPSE technical description 2014.1; 2014.
- [27] Brouwer GK, Lokhorst A, Orlic B. Geothermal heat and abandoned gas reservoirs in the Netherlands. *Proceedings world geothermal congress*. 2005. p. 24–9.
- [28] Moridis GJ, Pruess K. *Tough simulations of the updegraff's set of fluid and heat flow problems*. Tech rep, Lawrence Berkeley Laboratory; 1992.
- [29] Babaei M, Govindan R, Korre A, Shi J-Q, Durucan S, Quinn M. Calculation of pressure- and migration-constrained dynamic CO<sub>2</sub> storage capacity of the North Sea Forties and Nelson Dome structures. *Int J Greenhouse Gas Control* 2016;53:127–40.
- [30] Babaei M. Integrated carbon sequestration–geothermal heat recovery: performance comparison between open and close systems. *Transp Porous Media* 2018;126(1):1–25.
- [31] Cirpka OA. Generation of random, autocorrelated, periodic fields [online]; 2003.
- [32] TNO. TNO NI olie- en gasportaal [online]; 1977.
- [33] IAPWS. Release on the iapws industrial formulation 1997 for the thermodynamic properties of water and steam. IAPWS Secretariat. Palo Alto, CA: Electric Power Research Institute; 1997.
- [34] Willems C, Nick H. Towards optimisation of geothermal heat recovery: an example from the west Netherlands basin. *Appl Energy* 2019;247:582–93.